Engineering Journal

Fourth Quarter 2023 | Volume 60, No. 4

Smarter. Stronger. Steel.

Engineering Journal

American Institute of Steel Construction

Dedicated to the development and improvement of steel construction, through the interchange of ideas, experiences, and data.

Engineering Journal (ISSN 0013-8029) is published quarterly. Published by the American Institute of Steel Construction at 130 E Randolph Street, Suite 2000, Chicago, IL 60601.

Archives: Search at **aisc.org/ej**. Article downloads are free for current members and are available for a nominal fee for non-members.

Technical Note

Strength of I-Girders with Narrow Panels Subjected to Concentrated Loads

Rolando Chacón and Luis B. Fargier-Gabaldon

ABSTRACT

This technical note deals with the strength of web panels under concentrated loads, with emphasis on girders with closely spaced transverse stiffeners (commonly referred to as narrow panels). A review of experimental data and data from simulations suggest that girders with closely spaced panels exhibit substantially higher strength to concentrated loads than that calculated in accordance with the AISC *Specification for Structural Steel Buildings* (AISC, 2016). A simple equation to account for a fraction of the excess in strength is proposed.

Keywords: patch loading, closely spaced stiffeners, web crippling, flange resistance.

INTRODUCTION

Concentrated loads often govern the design of built-up steel I-girders, for example when launching plate girders or lifting heavy structures. To optimize web thickness and to prevent failure, transverse stiffeners at a constant spacing along the axis of the member are often provided. The behavior of steel built-up I-girders subjected to concentrated loads has been studied experimentally and analytically over the past six decades by Bergfelt (1979), Roberts and Rockey (1979), Roberts (1981), Roberts and Markovic (1983), Elgaaly (1983), Shimizu et al. (1989), Lagerqvist and Johansson (1995), Roberts and Newmark (1997), Tryland et al. (2001), Graciano (2005, 2015), Carden et al. (2007), Chacón et al. (2010a, 2010b, 2012), Salkar et al. (2015), Kövesdi (2018), and Rodilla and Kowalkowski (2021a, 2021b). Results from these investigations indicate that stocky webs exhibit local yielding, while slender or deep webs tend to buckle and fold (referred to as web crippling in the AISC *Specification*). In either case, the length on which the load is applied spreads out through the flange to a wider portion of the web that contributed to the load-carrying capacity. The *load length* is the length of the web affected by the concentrated load in the absence of vertical stiffeners.

Rolando Chacón, Department of Civil and Environmental Engineering, Universitat Politècnica de Catalunya, Barcelona, Spain. Email: rolando.chacon@upc.edu (corresponding)

Luis B. Fargier-Gabaldon, Massman-Beavers Associate Professor of the Practice of Heavy Civil Engineering, Department of Civil and Environmental Engineering and Earth Sciences, University of Notre Dame, Notre Dame, Ind. Email: luis.fargier@nd.edu

Paper No. 2022-03R

In this technical note, the behavior of beams with narrow panels failing in crippling and web yielding is investigated. Other failures modes, including sidesway buckling of the web, are beyond the scope of this investigation. In beams with narrow panels, the nominal *load length* calculated with the design equations exceeds the spacing between transverse stiffeners, a (Figure 1). In this technical note, experimental results and numerical simulations of girders with narrow panels subjected to concentrated loads are compared with the calculated strength in accordance with the AISC *Specification for Structural Steel Buildings* (AISC, 2016), hereafter referred to as the AISC *Specification*. It should be noted that the AISC *Specification* does not differentiate between girders with narrow panels and girders with wide panels (in which the nominal *load length* is less than a).

AISC *SPECIFICATION*

The strength of the built-up I-girders under concentrated loads, $R_{n\ AISC}$, is the smallest calculated for web yielding (Equations 1 or 2) and web crippling (Equations 3, 4, or 5). (Note that the AISC *Specification* equation number is also given for reference.) For web yielding, when the concentrated load is applied at a distance from the member end that is greater than the depth of the member, d,

$$R_{nAISC} = f_{yw} t_w (5k + l_b) \quad \text{(AISC } Spec. \text{ Eq. J10-2)} \quad (1)$$

When the concentrated load to be resisted is applied at a distance from the member end that is less than or equal to d,

$$R_{n\,AISC} = f_{yw} t_w (2.5k + l_b) \quad \text{(AISC } Spec. \text{ Eq. J10-3)} \quad (2)$$

For web crippling, when the concentrated load to be resisted is applied at a distance from the member end that is greater than or equal to $d/2$,

$$R_{n\,AISC} = 0.80t_w^2\left[1+3\left(\frac{l_b}{d}\right)\left(\frac{t_w}{t_f}\right)^{1.5}\right]\sqrt{\frac{Ef_{yw}t_f}{t_w}}Q_f$$

(AISC *Spec.* Eq. J10-4) (3)

When the concentrated compressive load to be resisted is applied at a distance from the member end that is less than $d/2$, two additional equations 4 and 5 are given for web crippling,

For $l_b/d \le 0.2$

$$R_{n\,AISC} = 0.40t_w^2\left[1+3\left(\frac{l_b}{d}\right)\left(\frac{t_w}{t_f}\right)^{1.5}\right]\sqrt{\frac{Ef_{yw}t_f}{t_w}}Q_f$$

(AISC *Spec.* J10-5a) (4)

For $l_b/d \ge 0.2$

$$R_{n\,AISC} = 0.40t_w^2\left[1+\left(\frac{4l_b}{d}-0.2\right)\left(\frac{t_w}{t_f}\right)^{1.5}\right]\sqrt{\frac{Ef_{yw}t_f}{t_w}}Q_f$$

(AISC *Spec.* J10-5b) (5)

When the concentrated compressive force is a live load (e.g., during launching of a steel plate girder, or a steel shape that serves as the rail of an industrial crane), the location of the force changes over time, and it is not possible to have a stiffener at every potential force location. In this case, the design strength calculated with the force acting between transverse stiffeners will exceed the demand. Equations 1 and 2 were proposed by Roberts (1981). In these equations, the term in parentheses may be interpreted as the nominal *load length*. For a concentrated load applied at a distance less than d from the end of the girder, a nominal *load length* equal to $2.5k + l_b$ is inferred from Equation 2. In Equations 3 to 5, however, the *load length* is not explicit. Roberts (1981) already found that Equations 4 and 5 tend to underestimate the strength of girders with narrow panels. He suggested that the calculated strength from these equations can be taken as the maximum concentrated load recommended under service conditions. Other design equations to estimate the strength at ultimate load for these cases have been proposed, including the Eurocode, EN1993-1-5 (CEN, 2006), and the work of Chacón et al. (2013a, 2013b, 2017). It should be noted that the design equations proposed by Roberts (1981) were derived from a set of experimental tests on simply supported single panels.

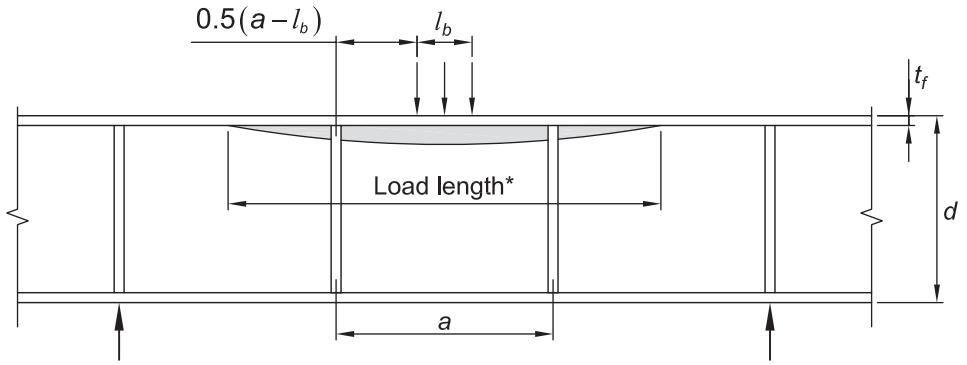

(a) Load away from the end of the girder

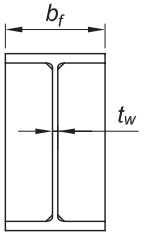

(b) Girder cross section

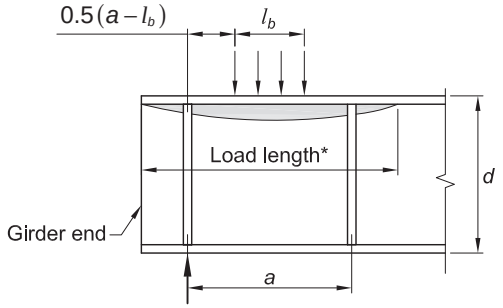

(c) Load close to the end of the girder

*Fig. 1. Built-up I-girder under concentrated loads (*nominal load length shown in absence of vertical stiffeners).*

TEST RESULTS AND NUMERICAL SIMULATIONS

Figure 2 shows the applied vertical load vs. displacement response of a typical built-up steel I-girder with closely spaced stiffeners tested by Chacón et al. (2013a, 2013b). The *load length* calculated for this girder, as defined, is not affected by the presence of vertical stiffeners. For girders with relatively closely spaced vertical stiffeners, the calculated *load length* may exceed the spacing between transverse stiffeners (see Figure 1 and Table A.1 in Appendix A). When transverse stiffeners are provided, however, the portion of the web resisting the concentrated load is bounded by the vertical stiffeners, and thus, the actual *load length* cannot exceed or extend beyond *a*. Multipanel built-up steel I-girders are more common in practice than single-panel built-up I-girders. The majority of tests from which design equations were derived have single panels and, thus, do not provide relevant information for the case of continuous deep girders with closely spaced transverse stiffeners. The last column of Table A.1 shows the ratio of the measured-to-calculated strength for two girders with three panels and closely spaced stiffeners (the strength obtained with the AISC *Specification*). The measured strength of both girders exceeds the calculated strength by a factor of 1.6. In this technical note, it is postulated that a fraction of the safety margin, or excess strength that is not captured by the current design equations, can be attributed to the reserve of strength in the loaded flange (that is engaged due to the presence of transverse stiffeners). Figure 2 shows a response curve of a tested specimen with three panels. A linear response up to approximately 250 kN (56 kips) is observed. This load is referred to as F_1 in Chacón et al. (2013a). At this load, the web starts to cripple, while the top flange remains elastic. A web folding mechanism was gradually observed from this point onward. For further load increases, the flanges and the stiffeners provided an additional load path allowing for some post-crippling capacity. A fraction of this post-crippling capacity, $\alpha\Delta F$ is provided by the reserve strength available in the loaded flange when the external load reaches F_1. Results from this investigation suggest that strength calculated based on the AISC *Specification*, $R_{n\,AISC}$, is a good approximation of the magnitude of F_1, as shown in Figure 2. The additional strength beyond $R_{n\,AISC}$ can be quantified and added, with certain assumptions. A database with test results from 62 steel built-up I-girders, some of which were collected by Lagerqvist (1994) and other specimens reported recently, was used to investigate the strength of beams with narrow panels. The measured strength, R_u, was normalized with respect to the strength calculated with Equations 2, 4, or 5, as shown in Figure 3. In addition, results from numerical simulations reported by Chacón et. al (2013a, 2013b, 2017) are included, and as it was done with the experimental data, normalized with respect to Equations 2, 4, or 5.

Data shown in Figure 3 suggest that Equations 2, 4, and 5 tend to underestimate the capacity of steel built-up I-girders girders with narrow panels (mean strength ratio is equal to 2.3).

There are at least two plausible and noncontradictory explanations for a fraction of the strength underestimation.

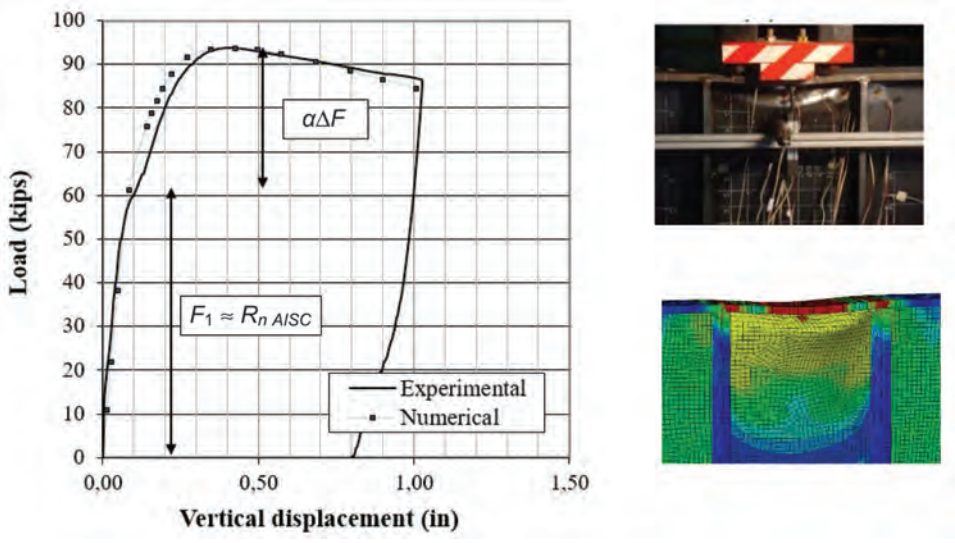

Fig. 2. Experimental and numerical results (beam VPL450, Chacón et al., 2013a).

First, the contribution of the flange to the web crippling strength as reported by Chacón et al. (2013a, 2013b, 2017) is not accounted for (in the derivation of Equation 4, only the mechanism associated with web crippling was adopted). Second, for the case of failures associated with web yielding, the AISC *Specification* requires a load length equal to $2.5k + l_b$ when the load is applied at a distance less than d from the end of the girder, regardless of the existence of stiffeners. In most cases, however, a bearing stiffener is present near the girder end [Figure 1(c)], leading to a significant strength increase.

CONTRIBUTION OF THE FLANGES TO THE STRENGTH, ΔF

The term ΔF can be obtained from a collapse mechanism involving four plastic hinges on the loaded flange (Chacón et al., 2013b). At an external concentrated load equal to F_1 (Figure 2) the web is assumed to cripple and its capacity exhausts. It is postulated that the strength increase, $\alpha\Delta F$, is resisted solely by the loaded flange (Figure 2). It should be noted that during the testing of the girder with narrow panels, a four-hinge collapse mechanism of the flange, as shown in Figure 4, is observed. The transverse stiffeners provide a load path to develop such hinges. Two plastic hinges develop in the vicinity of the flange-to-stiffener junction (outer hinges) while the other two plastic hinges develop under the applied load (inner hinges). The collapsed mechanism is idealized in Figure 4.

The strength contribution provided by the flanges, ΔF, can be estimated from a mechanism of the flanges as shown in Figure 4. The cross-sectional area of the flange is equal to $b_f t_f$ with length α between stiffeners, as shown in Figure 4. The reserve in flexural strength of the loaded flange at an applied external load corresponding to $R_{n\ AISC}$ is equal to Equation 6.

$$M_p = \frac{1}{4} b_f t_f^2 (f_{yf} - \sigma) \tag{6}$$

where σ can be taken as the peak flexural stress in the flange at the section under consideration, due to all loads acting on the plate girder (e.g., self-weight) when the magnitude of the external concentrated load is at the onset of

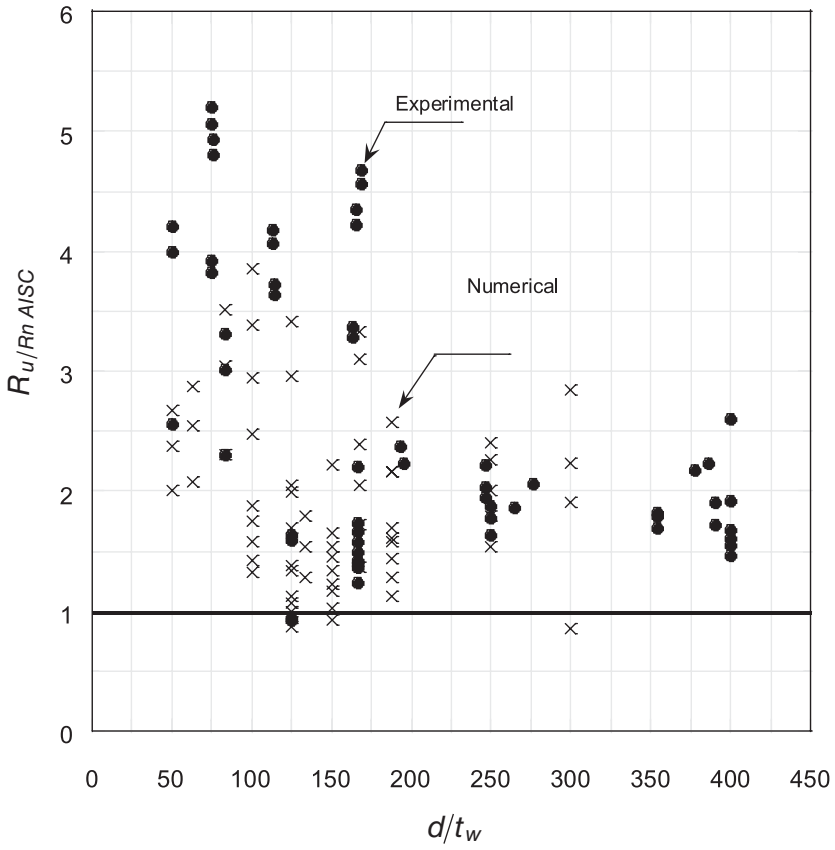

Fig. 3. Strength ratio vs. web slenderness ratio (using the AISC Specification*).*

web crippling, F_1, which can be approximated to $R_{n\,AISC}$, as shown in Figure 2. The peak stress can be obtained from a linear elastic beam model (Chacón et al., 2017). Based on the principle of virtual work and the idealized collapse mechanism shown in Figure 4, the additional strength can be calculated as shown in Equation 7.

$$\Delta F = \frac{4(M_{pi} + M_{po})}{a - l_b} \tag{7}$$

where M_{pi} and M_{po} are the reserve in flexural strength of the inner and outer hinges. Incorporating Equation 6 into Equation 7, one obtains Equation 8.

$$\Delta F = \frac{b_f t_f^2}{a - l_b}(2f_{yf} - \sigma_i - \sigma_o) \tag{8}$$

where σ_o and σ_i are the peak flexural stresses in the flanges (both positive) due to external loads for outer and inner hinges, respectively. This accounts for the contribution of flexural stresses as well. The proposed expression to estimate the strength of the girder with narrow panels failing in crippling is given by Equation 9.

$$R_{n\,proposed} = R_{n\,AISC} + \alpha\Delta F \tag{9}$$

The term $R_{n\,AISC}$ is obtained from Equations 4 or 5, ΔF is the contribution of the flanges calculated from Equation 8, and α is a correction factor determined empirically as shown in Equation 10.

$$\alpha = 1 - \frac{d/t_w}{1000} \tag{10}$$

Strength ratios calculated with $R_{n\,proposed}$ are shown in Figure 5. Given that all girders had bearing stiffeners, a load length equal to $5k + l_b$ was used for failures controlled by web panel yielding—that is, based on Equation 1 instead of Equation 2 (even when the load was applied at a distance less than d from the end of the girder). An average strength ratio equal to 1.8 is obtained, compared with 2.3 as obtained with Equations 2, 4, and 5. Once more experimental data become available of multipanel beams with narrow panels, a refined reliability analysis is recommended prior to introducing code changes (note that strength ratios range between 0.83 and 5.17, with only a few below 1.0). The proposed methodology, however, provides additional tools to tackle design or rehabilitation projects with a better understanding of the mechanics.

CONCLUSIONS

The equations given in the AISC *Specification for Structural Steel Buildings* (AISC, 2016) to calculate the strength of girders under concentrated loads are safe, but they tend to be quite conservative when applied to beams with narrow panels. A fraction of the excess in crippling strength not captured by the current AISC *Specification* equations can be estimated by adding the term shown in Equation 11.

$$\alpha\Delta F = \alpha\frac{b_f t_f^2}{a - l_b}(2f_{yf} - \sigma_i - \sigma_o) \tag{11}$$

When a bearing stiffener is present, a load length equal to $5k + l_b$ seems reasonable to estimate the web yielding strength under concentrated loads.

Data Availability Statement

Some data, models, or code that support the findings of this study are available from the corresponding author upon reasonable request.

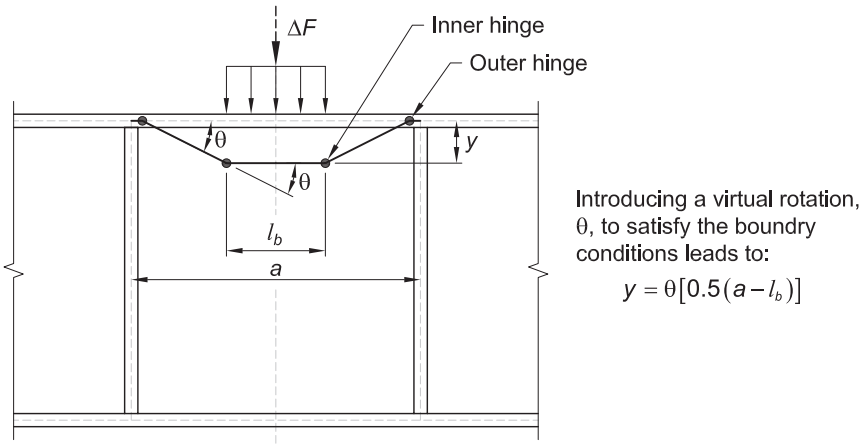

Fig. 4. Postulation of a four-hinge mechanism.

APPENDIX A EXPERIMENTAL RESULTS

Table A.1. Tests on Girders with Closely Spaced Stiffeners (Chacón, 2013a)

Girder	t_w in.	f_{yw} psi	f_{yf} psi	d_w in.	b in.	l_b in.	b_f in.	t_f in.	k in.	R_u kips	R_n Eq. 2 kips	R_n Eq. 4 kips	R_u/R_n
1VPL450	0.157	51.49	65.85	19.69	17.72	7.87	7.87	0.79	0.79	95.77	63.85	30.35	1.6
2VPL450	0.157	30.46	65.12	19.68	17.72	7.87	7.87	0.79	0.79	75.76	37.77	23.38	1.6

NOTATION

E Young's modulus of steel

F_1 patch load at which the response curve changes slope

F_2 ultimate load capacity

R_{test} measured strength

Q_f Chord stress interaction parameter factor 1.0 for wide-flange sections and for HSS in tension

$R_{n\ AISC}$ strength calculated in accordance with the AISC *Specification*

b panel width

b_f flange width

d member depth

f_{yf} flange yield stress

f_{yw} web yield stress

k distance from outer face of flange to the web toe of fillet

l_b bearing length of the patch load according to the AISC *Specification*

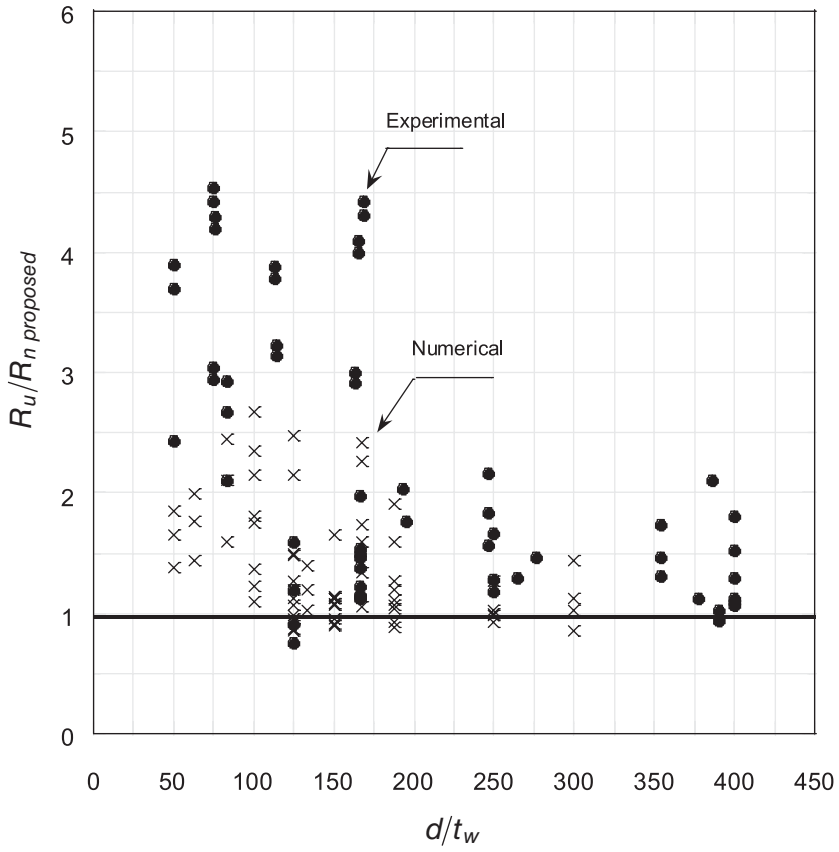

Fig. 5. Strength ratio from tests vs. web slenderness ratio using proposed equations.

t_f flange thickness

t_w web thickness

ΔF post-crippling capacity

REFERENCES

AISC (2016), *Specification for Structural Steel Buildings*, ANSI/AISC 360-16, American Institute of Steel Construction, Chicago, Ill.

Bergfelt, A. (1979), "Patch Loading on a Slender Web-Influence of Horizontal and Vertical Web Stiffeners on the Load Carrying Capacity," Report S79:1, Chalmers University of Technology, Gothenburg, Sweden.

Carden, L., Pekcan, G., and Itani, A. (2007), "Web Yielding, Crippling and Lateral Buckling under Post Loading," *Journal of Structural Engineering,* ASCE, Vol. 133, No. 5, pp. 665–673. https://doi.org/10.1061/(ASCE)0733-9445(2007)133:5(665)

CEN (2006), *Eurocode 3: Design of Steel Structures*, Part 1-5: Plated Structural Elements, EN 1993-1-5, Comite Européen de Normalisation, Brussels, Belgium.

Chacón, R., Braun, B., Kuhlmann, U., and Mirambell, E. (2012), "Statistical Evaluation of the New Resistance Model for Steel Girders Subjected to Patch Loading," *Steel Construction,* Vol. 5, No. 2, pp. 10–15. https://doi.org/10.1002/stco.201200002

Chacón, R., Herrera, J., and Fargier-Gabaldón, L. (2017), "Improved Design of Transversally Stiffened Steel Plate Girders Subjected to Patch Loading," *Engineering Structures,* Vol. 150, pp. 774–785. https://doi.org/10.1016/j.engstruct.2017.07.086

Chacón, R., Mirambell, E., and Real, E. (2010a), "Hybrid Steel Plate Girders Subjected to Patch Loading. Part 1: Numerical Study," *Journal of Constructional Steel Research*, Vol. 66, No. 5, pp. 695–798. https://doi.org/10.1016/j.jcsr.2009.12.005

Chacón, R., Mirambell, E., and Real, E. (2010b), "Hybrid Steel Plate Girders Subjected to Patch Loading, Part 2: Design Proposal," *Journal of Constructional Steel Research,* Vol. 66, No. 5, pp. 709–715. https://doi.org/10.1016/j.jcsr.2009.12.004

Chacón, R., Mirambell, E., and Real, E. (2013a), "Transversally Stiffened Plate Girders Subjected to Patch Loading, Part 1: Preliminary Study," *Journal of Constructional Steel Research,* Vol. 80, pp. 483–491. https://doi.org/10.1016/j.jcsr.2012.06.008

Chacón, R., Mirambell, E., and Real, E. (2013b), "Transversally Stiffened Plate Girders Subjected to Patch Loading, Part 2: Additional Numerical Study and Design Proposal," *Journal of Constructional Steel Research*, Vol. 80, pp. 492–504. https://doi.org/10.1016/j.jcsr.2012.06.001

Elgaaly, M. (1983), "Web Design under Compressive Edge Loads," *Engineering Journal*, AISC, Vol. 20, No. 4, pp. 153–171.

Graciano C. (2005), "Strength of Longitudinally Stiffened Webs Subjected to Concentrated Loading," *Journal of Structural Engineering*, ASCE, Vol. 131, No. 2, pp. 268–278. https://doi.org/10.1061/(ASCE)0733-9445(2005)131:2(268)

Graciano, C. (2015), "Patch Loading Resistance of Longitudinally Stiffened Girders—A Systematic Review," *Thin Walled Structures*, Vol. 95, No. 1–6. https://doi.org/10.1016/j.tws.2015.06.007

Kövesdi, B. (2018), "Patch Loading Resistance of Slender Plate Girders with Longitudinal Stiffeners," *Journal of Constructional Steel Research*, Vol. 140, pp. 237–246. https://doi.org/10.1016/j.jcsr.2017.10.031

Lagerqvist, O. (1994), "Patch Loading: Resistance of Steel Girders Subjected to Concentrated Forces," PhD Dissertation, Lulea University of Technology, Sweden. ISSN 0348-8373

Lagerqvist, O. and Johansson, B. (1995), "Resistance of Plate Edges to Concentrated Forces," *Journal of Constructional Steel Research*, Vol. 32, No. 1, pp. 69–105. https://doi.org/10.1016/0143-974X(94)00010-F

Roberts, T. (1981), "Slender Plate Girders Subjected to Edge Loading," *Proceedings of the Institution of Civil Engineers*, Vol. 71, No. 3, pp. 805–819.

Roberts, T. and Markovic, N. (1983), "Stocky Plate Girders Subjected to Edge Loading," *Proceedings of the Institution of Civil Engineers, Part 2*, Vol. 75, No. 3, pp. 539–550.

Roberts, T. and Newark, A. (1997), "Strength of Webs Subjected to Compressive Edge Loading," *Journal of Structural Engineering*, ASCE, Vol. 123, No. 2, pp. 176–186. https://doi.org/10.1061/(ASCE)0733-9445(1997)123:2(176)

Roberts, T. and Rockey, K. (1979), "A Mechanism Solution for Predicting the Collapse Loads of Slender Plate Girders when Subjected to In-Plane Patch Loading," *Proceedings of the Institution of Civil Engineers, Part 2*, Vol. 67, No. 1, pp. 155–175.

Rodilla, J.A. and Kowalkowski, K. (2021a), "Determination of Capacities of Eccentric Stiffeners Part 1: Experimental Studies," *Engineering Journal*, AISC, Vol. 58, No. 2.

Rodilla, J.A., and Kowalkowski, K, (2021b), "Determination of Capacities of Eccentric Stiffeners Part 2: Analytical Studies," *Engineering Journal*, AISC, Vol. 58, No. 2.

Salkar, R., Salkar, A., and Davids, W. (2015), "Crippling of Webs with Partial Depth Stiffeners under Patch Loading," *Engineering Journal*, AISC, Vol. 52, No. 4.

Shimizu, S., Yabana, H., and Yoshida, S. (1989), "A New Collapse Model for Patch Loaded Web Plates," *Journal of Constructional Steel Research*, Vol. 13, pp. 61–73. https://doi.org/10.1016/0143-974X(89)90005-9

Tryland, T., Hopperstad, O., and Langseth, M. (2001), "Finite-Element Modeling of Beams under Concentrated Loading," *Journal of Structural Engineering*, ASCE, Vol. 127, No. 2, pp. 176–185. https://doi.org/10.1061/(ASCE)0733-9445(2001)127:2(176)

Internal Redundancy of Mechanically Fastened Built-Up Steel Axially Loaded Two-Channel Members

Jason B. Lloyd, Francisco J. Bonachera Martin, Cem Korkmaz, and Robert J. Connor

ABSTRACT

Previous research on large-scale fracture tests on mechanically fastened built-up steel members subjected to flexural or axial loads demonstrated resistance to complete member fracture due to cross-boundary fracture resistance (CBFR). This paper builds on and expands that work through additional experimental and analytical research into behavior of two-channel mechanically-fastened built-up axial steel members following fracture of a single component. Finite element based parametric studies were conducted to characterize the static load redistribution behavior of axial members comprised of two channels, following a fracture event. FEMs were calibrated using experimental data obtained from full-scale testing. Simplified solutions were developed to estimate the after-fracture load capacity and the fatigue stress range in a remaining channel. The solutions are used to evaluate the internal redundancy of mechanically fastened built-up two-channel members. If this member type is found to be internally redundant during an evaluation, the developed solutions can then be used to reliably predict fatigue life of the member in the faulted state and establish the special inspection interval according to the relevant provisions of AASHTO.

Keywords: steel bridge, built-up steel members, nonredundant steel tension member, fracture critical member, internal redundancy, steel axial member.

INTRODUCTION

Since the Surface Transportation and Uniform Relocation Assistance Act of 1987 (Pub. L. 100-17, 101 Stat. 132), the AASHTO *Manual for Bridge Evaluation* (AASHTO, 2018) requires that bridges containing fracture critical members (FCMs) receive a "hands-on" inspection, meaning the inspector must be within an arm's length of any fracture critical component at least every 24 months (FHA, 1988). Fracture critical members have since been renamed nonredundant steel tension members (NSTMs) with an overhaul to the "National Bridge Inspection Standards" released in 2022 (FHA, 2022). NSTMs require the same level of inspection rigor as the FCMs, but the inspection interval may be shorter or longer, depending on a risk-based evaluation. The cost of hands-on inspections can be strenuous on state transportation budgets due to the time required on the bridges, traffic control during inspections, and specialized equipment required (Connor et al., 2005). Furthermore, while hands-on inspections of NSTMs are intended to improve public safety, a study carried out for Indiana interstates revealed that overall congested crash rates increased by 24.1 times over uncongested crash rates and that 90% of the congested crashes in 2014 occurred with a traffic queue duration of ≥ 5 minutes (Mekker et. al., 2015). Traffic queues of this magnitude can result from several things, including closed lanes on bridges during inspections. Protecting the safety of the traveling public is multifaceted—it isn't necessarily as simple as requiring more bridge inspection, particularly when one considers the probability of detection for very small defects intended to be found (Campbell et al., 2019). The approach to the nation's bridge inspection program should be rational—considering all the economic *and* safety factors and correlating damage tolerance with inspector capabilities.

Previous research that carried out large-scale fracture tests on mechanically fastened built-up steel members subjected to flexural or axial loads demonstrated resistance to complete member fracture due to cross-boundary fracture resistance (CBFR) (Hebdon et al., 2017; Lloyd et al., 2021). Additionally, Diggelmann et al. (2013) used shape charges to simulate fracture on the tension chord at midspan of the Milton-Madison deck truss approach span while the bridge was loaded with approximately 75 kips of sand placed on the middle third of the span. The chord was severed in two stages, the first of which cut one of the two built-up channels that made up the tension chord. Under the simulated live load, the researchers measured a global deflection of less than ⅛ in. After severing the remaining portion of the

Jason B. Lloyd, PhD, PE, Manager of Bridge & Infrastructure Solutions, Nucor, Charlotte, N.C. Email: jason.lloyd@nucor.com (corresponding author)

Francisco J. Bonachera Martin, PhD, PE, Technical Manager, Michael Baker International, Indianapolis, Ind. Email: FJ.BonacheraMartin@mbakerintl.com

Cem Korkmaz, PhD, Research Engineer, Lyles School of Civil Engineering, Purdue University, West Lafayette, Ind. Email: ckorkmaz@purdue.edu

Robert J. Connor, PhD, PE, Jack and Kay Hockema Professor, Lyles School of Civil Engineering, Purdue University, West Lafayette, Ind. Email: rconnor@purdue.edu

Paper No. 2023-01

tension chord, the bridge remained stable, and researchers measured a total deflection of less than ½ in. This is remarkable for a bridge that was in service for 91 years and a member identified as fracture critical and then required to be treated as such for the last 34 of those years.

This paper summarizes the experimental and analytical research into the behavior of two-channel mechanically fastened built-up axial steel members following fracture of a single channel. Finite element–based parametric studies were conducted to characterize the static load redistribution behavior of two-channel axial members following the fracture event. Finite element models (FEMs) were calibrated using experimental data obtained from full-scale testing. Simplified solutions were developed to estimate the after-fracture load capacity and the fatigue stress range in the remaining channel. The solutions can be applied to analyze for internal redundancy of these member types. If a member is found to be internally redundant, the simple solutions can then be used to reliably predict fatigue life of the member in the faulted state and establish the special inspection interval according to the provisions of AASHTO (2018).

Research Objectives

The primary objectives of the experimental testing were to understand the static load redistribution behavior in the faulted condition and calibrate finite element models for parametric study. The parametric studies were used to develop simplified engineering solutions for the evaluation of internal redundancy. In this case, the faulted condition is defined as having one-half of the total cross section severed. Brittle fracture testing was not necessary to achieve the test objectives. Furthermore, previous work on the internal redundancy of built-up members unequivocally demonstrated the inherent characteristic of mechanically fastened built-up members referred to as cross-boundary fracture resistance (CBFR) (Hebdon et al., 2017; Lloyd et al., 2021). CBFR provides brittle fracture arrest at component boundaries resisting total cross-sectional fracture. Therefore, in the present study, the fracture event was not necessary, and testing was performed by severing one-half of the unloaded chord using a cutting torch. Next, the specimens were statically loaded in the faulted condition. The first specimen, referred to as Specimen 1, was cut at location "B" (adjacent to the center gusset plate) as shown in Figure 1. The second was Specimen 2, which was cut at location "A" (mid-length between gusset plates), as indicated in the same figure. These locations were identified through analytical modeling to be the most severe cases in terms of secondary effects in the faulted member. Photographs of torch cuts can be seen in the insets for Figures 8 and 9.

Prior to cutting each specimen to simulate the after-fracture faulted condition, they were loaded in the as-delivered condition over several load cycles to ensure test setup and sensors were operating correctly. Data for the first several load cycles were discarded as part of the "shakedown" of the setup. Shakedown load cycles were performed within the elastic range of the specimen ensuring proper seating of the bolted connections to the load frame. Note that multiple load cycles (or tests) were performed on each specimen to ensure repeatability of results, particularly in the elastic range of loading, each being numbered chronologically as a different test number.

EXPERIMENTAL METHODS

The following sections discuss methods used for experimental research of after-fracture load redistribution behavior of axial steel tension members comprised of two channels. Full-scale laboratory experiments were performed on members removed from a retired bridge taken out of service.

Condition of Test Specimens Removed from Service

The two specimens used for the experimental portion of the research on two-channel members were removed from an approach span of the Winona Bridge that was built in 1940 carrying traffic over the Mississippi River near Winona, Minnesota. Figure 2 shows the general condition of the specimens as they were delivered, after nearly 80 years in service. The condition of the rolled channels was generally sound with minor section loss resulting from corrosion. Figure 2 also shows a sketch of the cross section at one of the stay plates, which has the appearance of a box section; however, the stay plates were intermittent along the lengths spaced at a distance of 43 in. center-to-center (28 in. clear distance). The channels were C15×40 rolled channels, made continuous through the gussets. The cover plates were 14¾ in. tall by ⅜ in. thick and were spliced at the gussets. Moderate to severe pack rust was evident

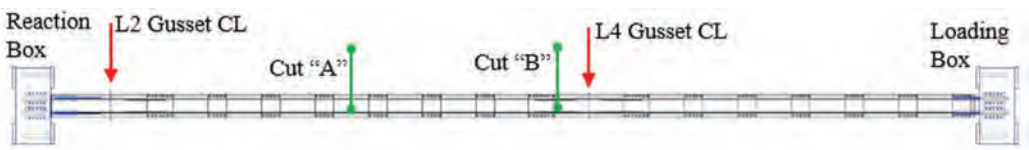

Fig. 1. Plan view sketch of specimen showing locations of the torch cuts.

between the channels and the cover plates along the top of the chords. The gusset connections for the mid-span tension chord sections were also in good condition with some minor corrosion damage. Figure 3 shows a portion of Specimen 2 where cracks were identified in the cover plates resulting from pack rust that were present during all testing. It also shows typical section loss at the stay plates.

Load Frame and Specimen Preparations

A horizontally oriented, self-reacting load frame was designed and fabricated in-house with capacity for 1.5 million pounds. In order to react against the large tension forces, two 60-foot-long W24×146 rolled wide flange beams were used as compression elements in the load frame. Load and reaction boxes (one at each end of the specimen) transferred load between the test specimen and the compression reaction columns of the load frame. Figure 4 shows a specimen placed between the reaction columns with the loading box attached. Figure 5 shows a top-down perspective of this area. The four hydraulic jacks pushed against the loading box, supported by the reaction columns putting the specimen into axial tension. Steel rollers were placed below the specimens and the reaction columns, allowing the entire load frame and specimen to undergo unrestricted strain without impeding their opposing relative displacements.

The two test specimens were removed from a deck truss span of the Winona Bridge, as shown by Figure 6. One came from the east truss line and the other from the west truss line. The specimens were approximately 65 feet long upon arrival and were cut to the final testing length of 740.5 in. (61.7 feet). Rivets were removed at each end and bolt holes were drilled for connection to the loading boxes. All connections were bearing-type connection using 1-in.-diameter ASTM F3125/F3125M Grade A325 high-strength bolts (ASTM, 2019), thereby reducing the number of required bolts. To account for any movement or "shake down" in the connection, load was applied to ensure all connections

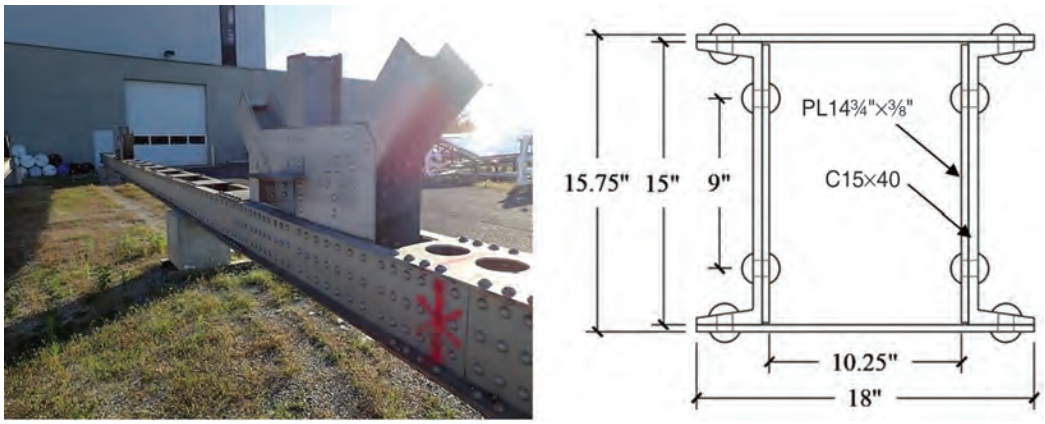

Fig. 2. Winona Bridge specimens.

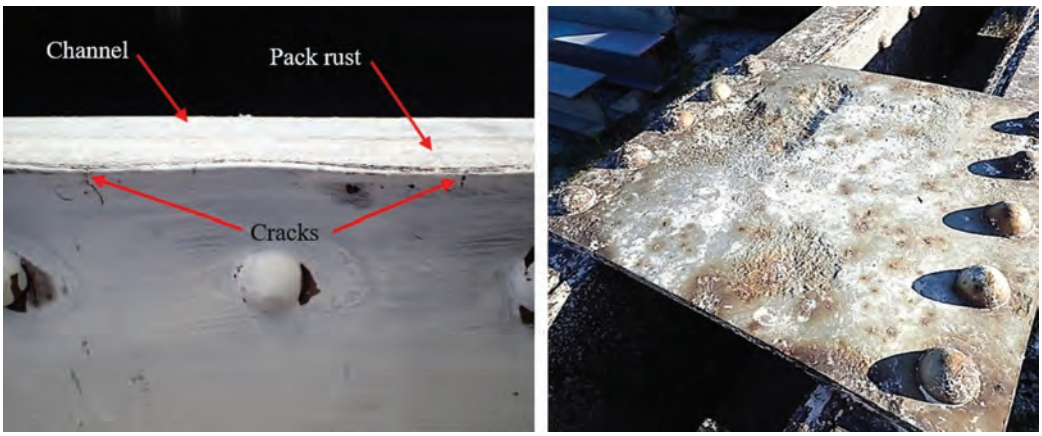

Fig. 3. (Left) Specimen 2 (whitewashed for testing) showing defects and section loss; (right) typical section loss of a stay plate.

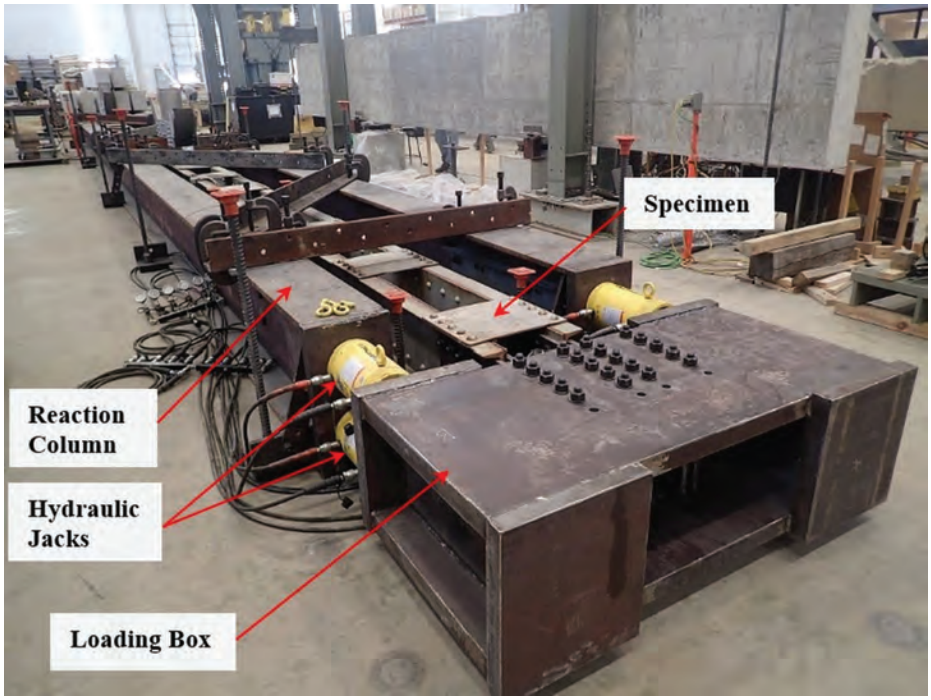

Fig. 4. Load frame with specimen placed and ready for testing.

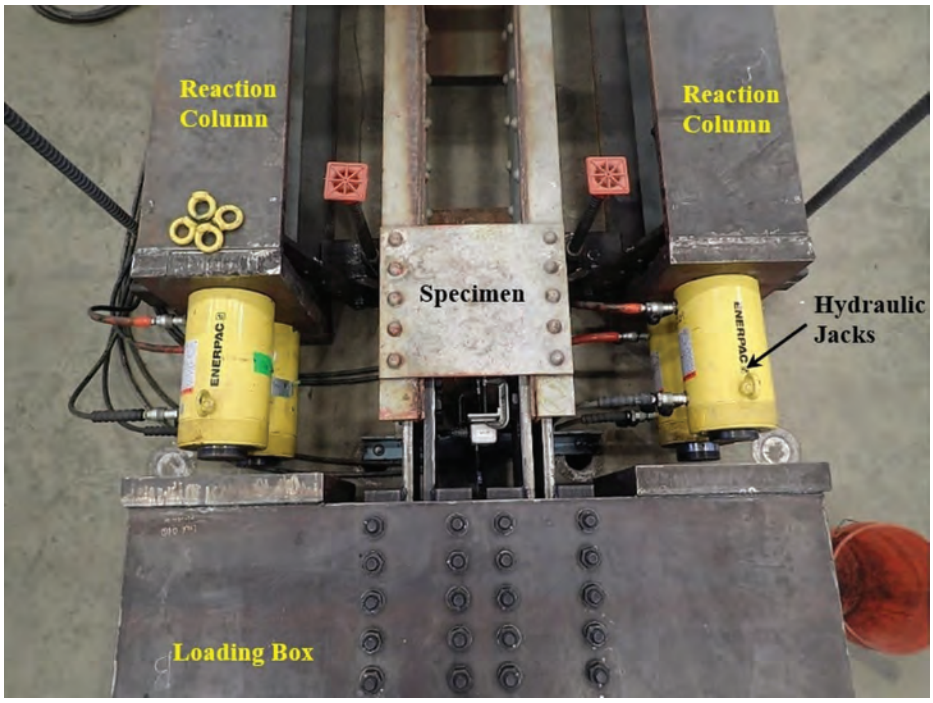

Fig. 5. Top view of loading frame and specimen connection.

Table 1. Comparison of CVN Impact Energy				
Service Temperature (°F)	AASHTO Fracture-Critical (ft-lb)	AASHTO Nonfracture-Critical (ft-lb)	Average for Winona Channel (ft-lb)	Average for Winona Cover Plate (ft-lb)
70 (Zone 1)	25	15	16.0	18.2
40 (Zone 2)	25	15	10.0	10.7
10 (Zone 3)	25	15	6.8	6.0

were fully seated. This process helped remove excess displacements that could be wrongfully attributed to specimen elongation, particularly when the connections are designed as bearing connections and when, inevitably, some of the fasteners go into bearing before others.

Experimental Test Results

The following sections describe the experimental test results, including material testing and static load tests of the specimens in the faulted condition.

Material Testing

Prior to load testing, material samples were removed from the cover plate, channel web, and two gusset plates to test for Charpy V-notch impact (CVN) energy (for estimation of toughness), yield strength, tensile strength, and chemical composition. The material testing was performed according to requirements of ASTM E23 (2016a), ASTM E8 (2016b), and ASTM E415 (2017), respectively. The steel was found to be consistent with the standards of ASTM A7 that likely would have been specified at the time of construction of the Winona Bridge in the late 1930s.

Although some limited chemical specifications and tensile capacity minimums were typically provided in early steel specifications, toughness was not. Toughness is the material property that quantifies the ability of a material to resist fracture in the presence of a notch or crack. Direct measurement of toughness requires costly testing and relatively large piece of material. As a result, an economical alternative often used is the CVN test. These tests are not a direct measure of toughness, but rather a measure of energy absorption. However, using accepted correlation methods, such as the master curve method, fracture toughness can be estimated from CVN data. Table 1 compares the modern CVN impact energy requirements from Section 6 of the *AASHTO LRFD Bridge Design Specification* (AASHTO, 2020) with the average of three CVN impact energy test results at the service temperature indicated. As a point of interest, the only category for which the historic steel would meet the modern specification is Zone 1 Nonfracture-critical. See the complete results of the material tests provided by Lloyd et al. (2019).

Load Test Results

Figure 7 shows a load-displacement plot for Specimen 1 prior to being purposefully cut to simulate a partial member failure. The line labeled "Nominal" is the calculated, or nominal, load-displacement curve based on a simple mechanics of materials equation for displacement of an axially loaded body (i.e., $\delta = PL/AE$) using the gross cross-sectional area. The measured load-displacement relationship correlated well with the nominal estimation and indicated a linear-elastic response to the applied load. The peak load of 1150 kips surpassed the original design load for the member by 222% and effectively reached the upper bound capacity of the hydraulic jacks. This portion of the testing helped confirm proper loading and unloading cycles were being performed and that sensors were operating as desired. Next, load was removed and Specimen 1 was cut between the end stay plate and the L4 (center) gusset plate

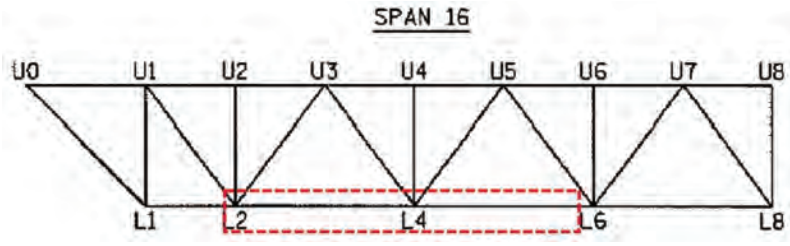

Fig. 6. Winona Bridge deck truss span—specimens removed from area shown by the dashed line.

(location "B" as indicated on Figure 1) leaving only half of the original cross section intact. Several load cycles were applied to the member in this condition, including a final load cycle up to 800 kips, as plotted in Figure 8. The calculated, or nominal, load-displacement curve has also been plotted and labeled for the linear-elastic portion of the loading, which does not take into account the loss of half the cross section. In other words, the full cross-sectional area was used in the nominal estimate. The nominal, or unfaulted, member stiffness is used in this case to make a comparison back to Figure 7, demonstrating the change in stiffness as a result of the simulated fracture. The curve is based on the simple calculation of elastic displacement of an axially loaded body, as explained earlier. However, in this case, it is not an equitable comparison because the measured curve now represents the member in the faulted condition with only half of its cross section at location "B" (i.e., near the gusset plate). The specimen experienced approximately an 18% reduction in axial stiffness in the faulted condition. This is without the benefit of system behavior one might expect for a member in a bridge where other members, bracing, etc., are connected to the faulted chord provided alternative load paths and additional stiffness. That is to say that in a real-world application, any loss of axial stiffness in the faulted member would result in the member shedding some load to adjacent members. System behavior was observed by Diggelmann et al. (2013) during field testing of a deck truss bridge where explosives were used to sever half of a built-up channel member on the Milton-Madison Bridge. The load measured in cross members, as well as in the truss line opposite the severed member, were observed to increase slightly. This is an important observation simply because all evaluation methods developed in this research conservatively assume that the entire load originally carried by the faulted member remains in the faulted member. However, minor load shed from the damaged member will help improve both strength and fatigue performance of a member in the faulted condition in real-world conditions.

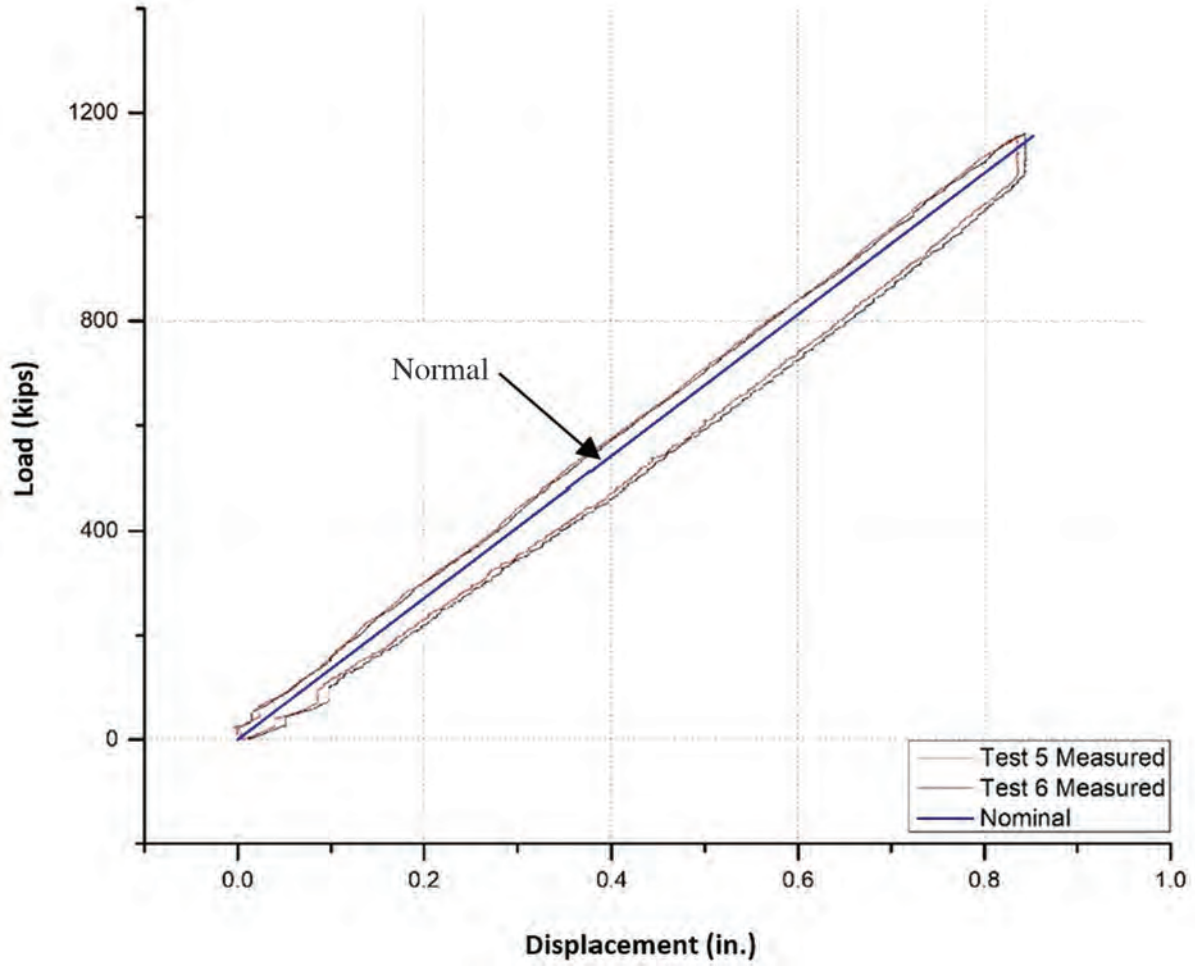

Fig. 7. Load vs. displacement curve for Specimen 1 prior to severing half of the cross section showing predictable elastic behavior.

Table 2. Test Specimen Cross-Sectional Area and Capacity in the Faulted Condition		
	Specimen 1 (at Location "B")	**Specimen 2 (at Location "A")**
Faulted gross area (in.^{2})	19.2	17.3
Faulted net area (in.^{2})	15.9	14.5
Nominal load at gross section yield (kips)	632	571
Predicted load at gross section yield (kips)	754	679
Nominal load at net section fracture (kips)	954	870
Predicted load at net section fracture (kips)	1070	972
Maximum test load (kips)	800	647

Table 2 provides the "nominal" (based on published ASTM A7 material properties) and "predicted" (based on measured material properties) section capacity calculations for the specimen in the faulted state. Figure 8 plots results for Tests 12 (elastic range) and 13 (failure). It can be seen in Figure 8 that the onset of yielding occurred during Test 13 at around 600 kips, which is notably less than the predicted gross section yield load on the faulted section of 754 kips. However, a yield load based on the faulted *net* section is approximately 625 kips. The initial onset of yielding probably began at the fastener holes, most likely the first set of rivets shared by the splice plate and cover plate or gusset plate. This is supported by the locations of observed rivet slip in the final load cycle for Specimen 1 (see Figure 10). At the peak load, it can be observed that the specimen began inelastic deformation holding peak load momentarily through minor strain hardening before permanent deformation increased and began to shed load.

Note that the faulted specimen exceeded the original design load of 517 kips (obtained from the original design drawings) by 15–20% before the onset of yielding and was able to reach about 1.5 times the design load before onset of gross section yielding on the faulted section. This is remarkable considering that the specimen reached this load while also resisting flexural stress resulting from an after-fracture second-order moment at the location of the failure.

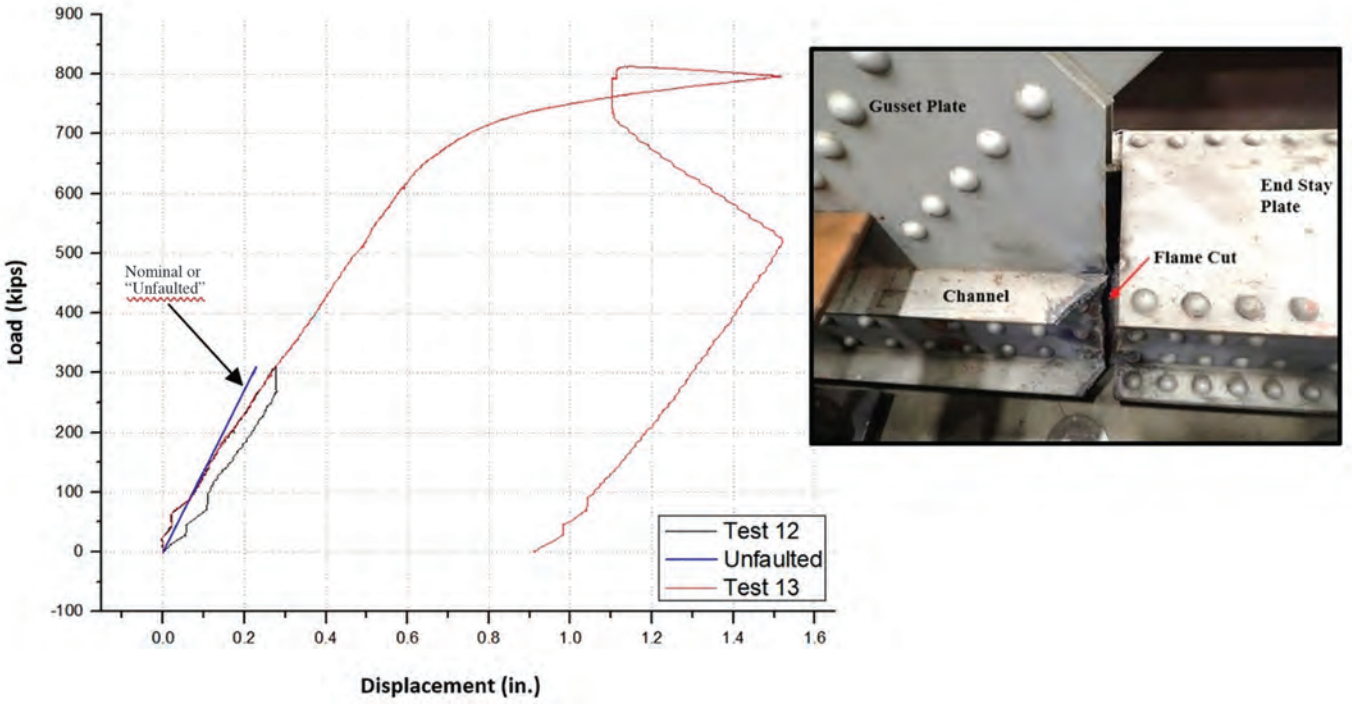

Fig. 8. Load vs. displacement curve for Specimen 1 (cut near gusset plate).

Specimen 2 was also loaded several times in the unfaulted condition in order to perform a shakedown on the connections and ensure the specimen was seated into the load frame properly. Several additional static load cycles were applied on the faulted section up to a peak load of 647 kips. A few of these have been plotted in Figure 9 where cycles up to 300 kips remained linear-elastic and later cycles reaching loads of 600 kips or more produced permanent plastic deformation on the faulted section. The calculated nominal load-displacement curve of the member in the unfaulted condition has also been plotted as reference. In this case, the axial stiffness of the specimen in the faulted condition was reduced by 45% (within the elastic range of loading). This would have resulted in load shed to adjoined members in an actual structure. This is notably more loss as compared to Specimen 1, likely due to the fact that Specimen 1 had the benefit of mutiple members and plates within the vicinity of the failure (cross-member stubs connecting gusset plates, bracing, etc.) helping to provide stiffness and load transfer. Table 2 provides the "nominal" (based on published A7 material properties) and "predicted" (based on measured material properties) section capacity calculations for the specimen in the faulted state. Similar to Specimen 1, Specimen 2 experienced what was likely a net section yielding at about 500 to 550 kips, which is less than the calculated gross section yielding load of 679 kips. The 550 kip load closely corresponded with a yield load calculated on the *faulted* net section of 565 kips. Once again, the faulted specimen was able to achieve loads in excess of the original design load (obtained from design drawings)—in this case, by just over 25%—in addition to resisting the after-fracture second order-moments induced by resdistribution of loads around the failure.

In both cases, the stay plates showed no sign of permanent deformation at the peak loads. Figure 10 shows Specimen 1 after testing has been completed where localized damage is labeled, such as channel flange buckling, slip at the rivets, and rotation of the end stay plate. Slip at the rivets indicates that either the rivet has yielded, the plate has yielded locally at the rivet hole, or both. The in-plane rotation of the stay plate shown in the figure was indicated at the corner of the end stay plate where a small unpainted section of the channel was exposed. The stay plates resisted opening of the severed channel through horizontal in-plane shear action. This put part of the stay plate in tension and part of the plate in compression, the capacity of which would theoretically be controlled by the buckling capacity of the plate. However, in both experimental cases, and as was later confirmed in the parametric study, the faulted member capacity was not limited by the stay plate thickness (and thus buckling capacity), which was found to have no effect on the internal redundancy analysis. The plates for

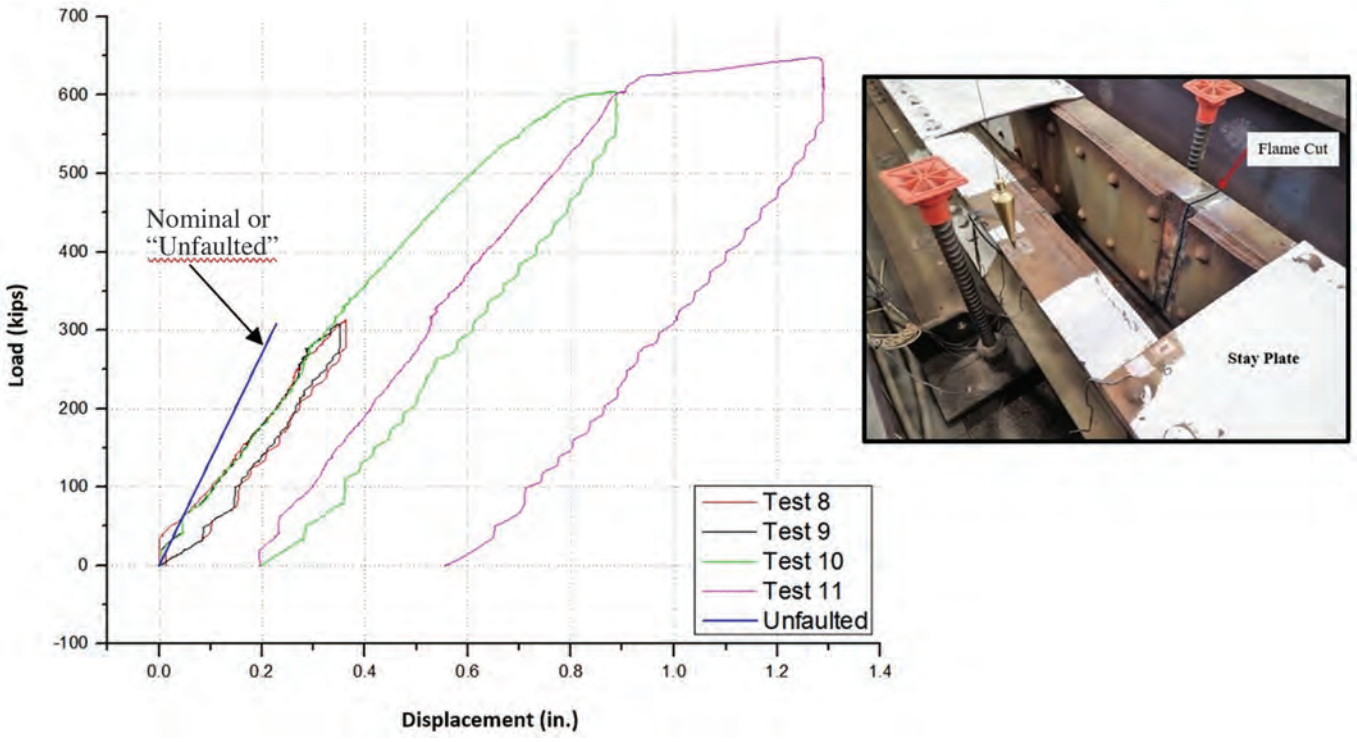

Fig. 9. Specimen 2 load-displacement curves (cut at mid-panel).

Specimen 1 and 2 were ⅜ in. thick—a common thickness for riveted built-up members and which can be considered a typical minimum thickness for stay plates.

PARAMETRIC STUDY OF TWO-CHANNEL MEMBERS

Global behavior of two-channel members resulting from a single failed channel was investigated in a parametric study using the Abaqus software suite. The parametric study resulted in several simplified solutions intended to be used to calculate second order moments, which can be superimposed to estimate the live load stress range in the unbroken channel.

Two-Channel Member FEM Calibration and Specifications

Finite element models for the two-channel member parametric study were calibrated using the experimental test data from Specimen 1 and 2. Following FEM calibration, numerous three-dimensional member geometries were created and evaluated using linear elastic, static implicit analysis. The geometries studied included stay-plated members and double-latticed members with the intersection of the lattice bars connected. Single lattice bar configurations were not studied after research showed that lacing bars contribute negligibly to load redistribution in the faulted condition. This is discussed in greater detail below. Concentrated loads were applied at reference points that were connected to the member cross section using kinematic coupling constraints, which uniformly distributed the load. Plates and channels were modeled using four-node doubly curved shell elements with reduced integration and hourglass control (Abaqus designation S4R) and a structured quadrilateral mesh. The global mesh size was ½ in. using the Simpson integration rule with five integration points through the thickness of the shells. Lattice bars were modeled using two-node linear beam elements (Abaqus designation B31) with a 1½ in. mesh size. A shell element mesh convergence study was performed halving the mesh density to 1 in. elements and then doubling the mesh density to ¼ in. elements at locations adjacent to the failure sites. It was found that the results were insensitive to the mesh size up to at least 1 in. However, the ½ in. element size facilitated the integration of nodal forces at locations of interest without significant increase in computational cost.

Figure 11 is zoomed in on a gusset plate connection on the +60-ft-long specimen showing a typical mesh for the models. Rivets were not explicitly modeled. Although nonlinear connector elements were initially used that were calibrated to experimental single fastener shear test data obtained from Ocel (2013), no significant improvement to the stress outcomes was observed. Hence, the use of connector elements to model rivets was not carried forward into the parametric study. Instead, plates and channels were connected using surface-to-surface tie constraints. Lattice bars were connected to channel flanges and at center points of lattice bar intersections using kinematic tie coupling constraints that allowed rotation about what would be the fastener longitudinal axis.

For the benchmark FEM, an elastic-plastic isotropic material was defined for the channels and plates having a yield strength equal to the measured cover plate yield strength of Specimen 1 and 2. The modulus of elasticity was defined as 29,000 ksi and a Poisson's ratio of 0.3. Following calibration of the shell element models, the material definition was simplified to linear-elastic for the parametric study.

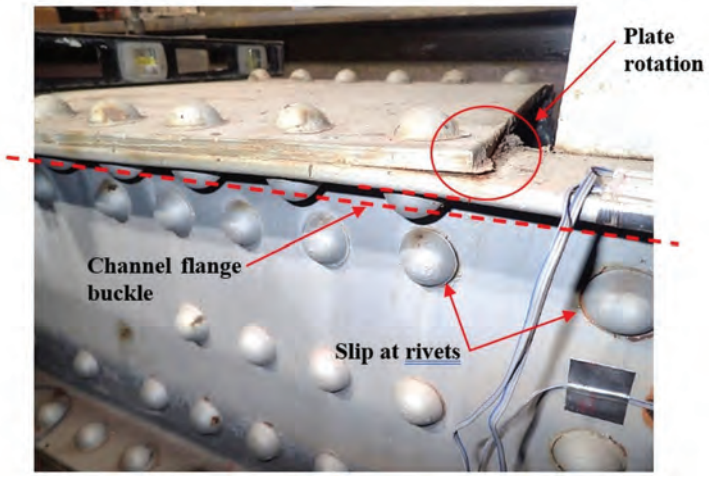

Fig. 10. Specimen 1 after testing showing signs of permanent deformation.

Data collected during the laboratory testing of Specimens 1 and 2 were compared to the benchmark finite element model to calibrate the model parameters and ensure accurate solutions. Strain, load, and displacement sensors used during the experimental testing provided data for comparison. Figures 12 and 13 show load-displacement curves for each of the specimens compared to load-displacement results obtained from the benchmark FEM. While the load-displacement relationship was not necessarily the output of interest for purposes of the parametric study, it was considered a useful indicator of overall behavior and response to load in comparison of the laboratory test results to the FEM results—particularly in the faulted condition.

Figure 12 plots data for Specimen 2, where the member was cut at location "A" (midpoint between gusset plates). Several elastic load cycles were applied, followed by two large load cycles resulting in permanent plastic deformation. It can be seen in Figure 12 that the FEM results compared relatively well with the laboratory results, particularly within the linear-elastic range up to about 400 kips. The FEM load-displacement curve showed reasonable nonlinear behavior, as well. The same can be said for Figure 13 comparing FEM results to Specimen 1, which was cut at location "B" (between the gusset plate and end stay plate). The goal of this benchmarking process was to simplify the FEM as much as possible while achieving reasonable and acceptable accuracy that could be carried forward into the parametric study. The lack of undue complexity of the model resulted in the divergence at peak loads seen in the plots. For example, at peak load, slip at rivets immediately adjacent to the failure site, slip at bolted connections used to attach the specimen to the load frame, in-plane rotational slip of the stay plate pairs closest to the failure site, as well as localized fastener hole deformation at extreme loads were observed. These sources of additional axial displacement would not be captured by the simplified FEM but were not considered necessary for the objectives of the parametric study either, which focused on linear-elastic behavior in the faulted condition that would be used for fatigue-based stress-range calculations and subsequent fatigue life estimates.

Strain gages were placed at several cross sections along the length of the test specimens. The benchmark FEM longitudinal stress results were within 10% or less of laboratory results at all critical areas, such as near the points of severed members, and within 15% or better at all other locations. Figure 14(a) shows a cross-sectional view of the benchmark FEM at the site of the "failure" of Specimen 2. Symbols are sketched at approximate locations where the strain gages were installed, corresponding to the stress plots in Figures 14(b)–(d). Figures 14(b)–(d) plot stress on the vertical axes and transverse position on the component on the horizontal axes. Dashed lines are also sketched on Figure 14(a), corresponding to the path across which the stress outputs were obtained from the FEM. Figure 14(b) shows longitudinal normal stress across the width of the cover plate. The triangle indicates the location of the strain gage, which was centered between the edges of the cover plate, as well as between the adjacent stay plates, directly across from the severed half of the member. Figure 14(c) shows longitudinal normal stress across the width of the channel flange. Two strain gages were installed on the flange: One (diamond) was located 1½ in. from the edge of the flange, and the other (circle) was ½ in. from the edge. Both of these gages were centered between the adjacent stay plates directly

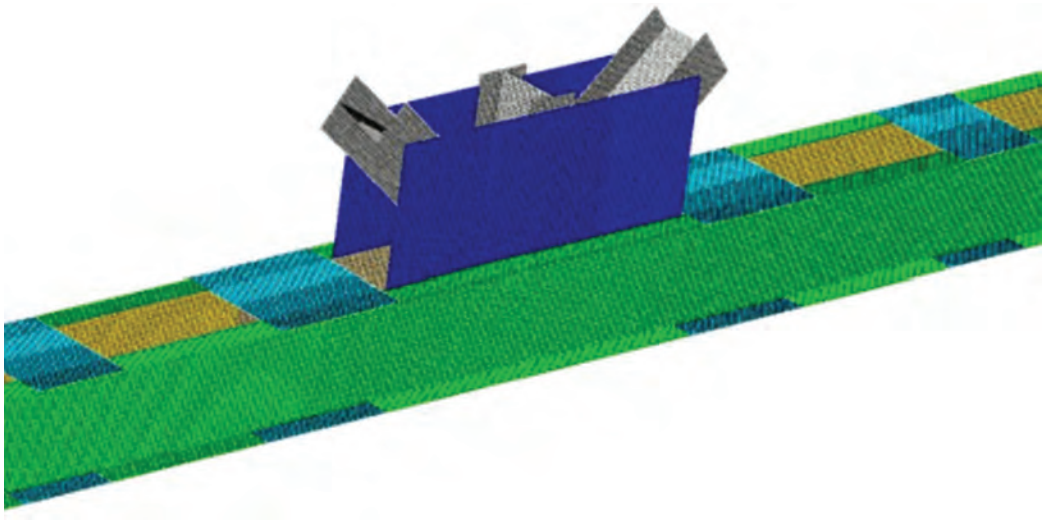

Fig. 11. Typical ½ in. shell element mesh used for FEM validation and two-channel member parametric study.

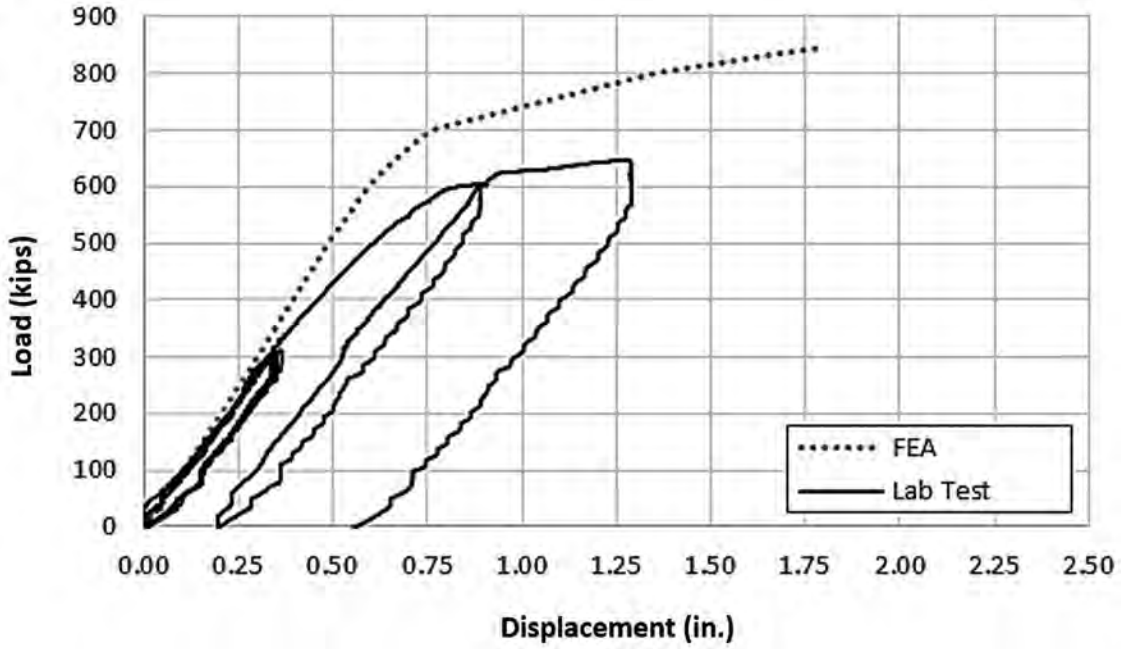

Fig. 12. Benchmark data comparing FEA results to lab test data for Specimen 2 in faulted condition with severed member at mid-panel (Cut "A", Fig. 1).

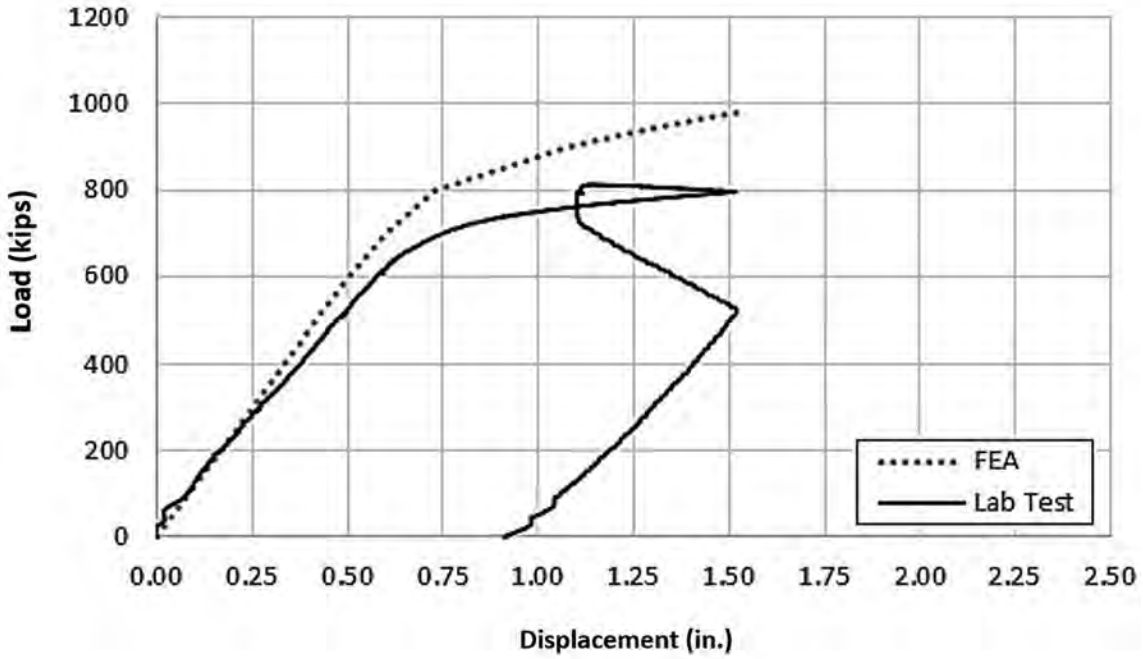

Fig. 13. Benchmark data comparing FEA results to lab test data for Specimen 1 in faulted condition with severed member at mid-panel (Cut "B", Fig. 1.)

across from the severed half of the member. Figure 14(d) plots longitudinal normal stress across the width of the channel web. The square indicates the location of the strain gage, which was directly opposite the strain gage installed at mid-depth on the cover plate. The applied load was 300 kips. All FEM results in this location were within 10% or less of laboratory measurements.

Figure 15 shows a rotated elevation view of the same FEM, where the severed half can be seen, along with the stress hotspots at the corners of the stay plates. The strain gage symbols have also been placed on Figure 15 to illustrate their approximate positions. Note that the cover plate gage (triangle) is out of view. Stresses in the intact half of the member resulted from the axial load applied to the member, as well as a secondary moment resulting from load redistribution around the discontinuity. Stay plates functioned as load paths for the redistribution, carrying load through in-plane shear and helping resist opening of the severed half of the member. This caused the intact member to displace inward (toward the severed member). Out-of-plane displacements of the FEM at the location of "failure" matched laboratory specimen measurements to within 5% at peak loads.

Pinned and fixed boundary conditions were also applied to the FEM to understand the effect it may have on the benchmark results. It was found that end boundary conditions had a negligible effect likely due to benefits attributed to the member being continuous at the center gusset, meaning more than a single panel length. The influence of boundary conditions within the context of the parametric study is discussed in more detail later.

The benchmark shell element model, as described herein, was found to be acceptably accurate, particularly within the linear-elastic range. Stresses and displacements outputs at locations of highest interest were found to be within 10% of that measured in the laboratory tests and therefore, set the standard for finite element models used in the parametric study.

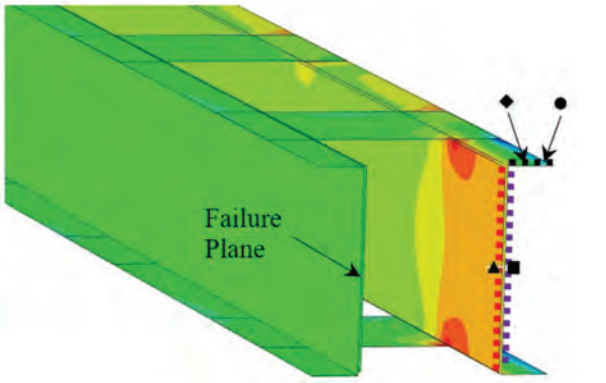

(a) Isometric view of the FEM identifying the approximate locations of the sensors

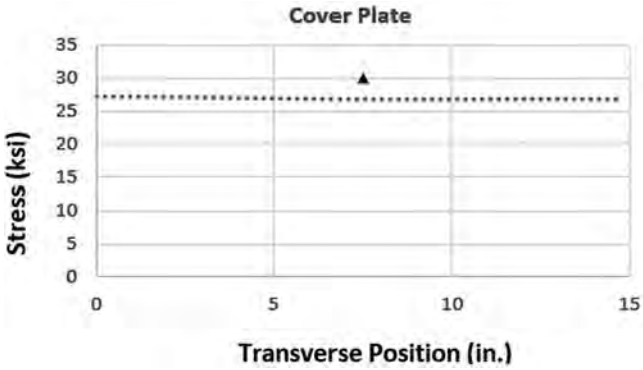

(b) FEA vs. measured stress at inside cover plate surface [see Fig. 14(a)]

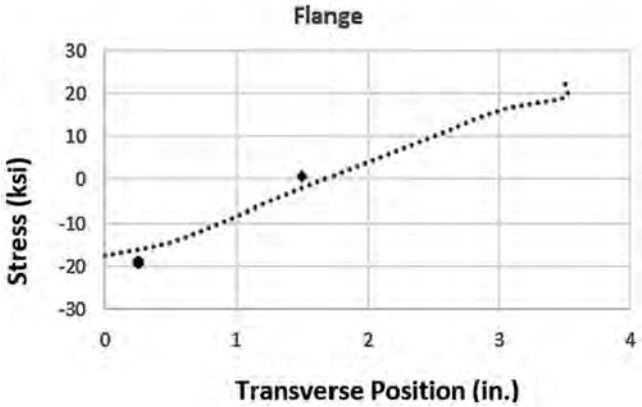

(c) FEA vs. measured stress at top of channel flange surface [see Fig. 14(a)]

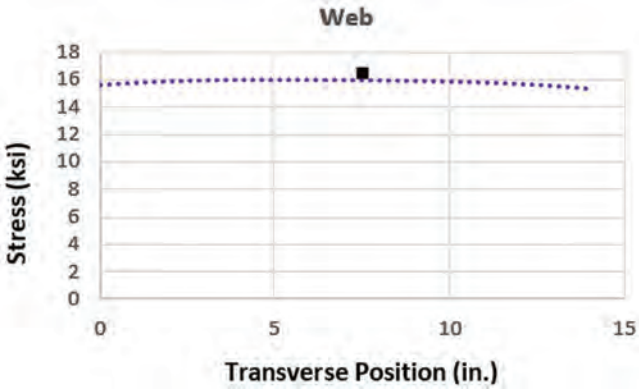

(d) FEA vs. measured stress at inside channel web surface [see Fig. 14(a)]

Fig. 14. Benchmark data comparing FEA results to measured data at the location of failure.

Geometric Parameters Varied for Two-Channel Members

The parametric study was divided into four subgroups: continuous stay-plated, continuous laced, noncontinuous stay-plated, and noncontinuous laced. Continuous stay-plated members are two-channel members where the channels are connected using intermittent stay plates (also known as batten plates) and made continuous through multiple panel points (or truss nodes). Continuous laced members are two-channel members with the channels connected using lattice bars and made continuous through multiple panel points. The noncontinuous stay-plated members are two-channel members connected using intermittent stay plates and extending between two panel points, such as would be the case for a truss shear diagonal member. The noncontinuous laced members are the same as noncontinuous stay-plated members, except that the channels are connected using lattice bars instead of stay plates. Each of these subgroups was studied for effects of equivalent applicable parameters but were divided into subgroups due to the differences in after-fracture load redistribution behavior.

The modern AASHTO *LRFD Bridge Design Specification* (AASHTO, 2020) is silent on the sizing and spacing of stay plates and lattice bars for built-up tension members. It does provide guidance on the design of built-up compression members, including single-angle members. Many existing built-up members, however, were constructed long before the modern LRFD design specifications. The earliest AASHTO design specification that could be referenced for this work was *The Standard Specifications for Highway Bridges* adopted by AASHO (now AASHTO) in 1935 (AASHO, 1935). It provided design guidance for built-up tension and compression members. It states that separate segments of tension members composed of shapes may be connected by stay plates or end stay plates and lacing. End stay plates for tension members were required to be sized the same as for compression member intermediate stay plates. Intermediate stay plates of tension members were required to be sized at a minimum of three-quarters of that specified for compression member intermediate stay plates. Additional information on the design provisions of stay plates from AASHO 1935 is summarized by Lloyd et al. (2019).

The *AREMA Manual for Railway Engineering*, Chapter 15, provides guidance on design of stay plates and lattice, as well (AREMA, 2017). It states that built-up members shall be connected by stay plates or lacing bars with end stay plates. It goes on to specify that tension members shall have stay plates sized to a minimum of two-thirds the lengths specified for stay plates on primary compression members. The angle of orientation of lacing bars, thickness of the lacing bars, and fastener requirements was found to be similar to the requirements of the 1935 AASHO Standard Specifications. Additional information on the design provisions of stay plates and lattice from AREMA is summarized by Lloyd et al. (2019). It was preferred to develop a simplified method of analysis that would be inclusive of all reasonable designs, including those that were designed per the 1935 AASHO provisions and those designed per the AREMA provisions. Therefore, the parametric study included a range of models with size and dimensional aspects that enveloped the requirements of the 1935 AASHO *Standard Specifications* (AASHO, 1935).

Parameters Evaluated for Two-Channel Members

Lloyd et al. (2019) provide details as to the geometries considered in that parametric study within an appendix. The reader is encouraged to reference that report for more information. Many of the parameters evaluated for the two main types of members, stay-plated and laced, were similar. However, there were several parameters unique to each type of two-channel member. The parameters evaluated for stay-plated members included:

- Boundary conditions: Fixed vs. pinned
- Channel section: C8×11.5, C15×40, and C15×50
- Channel spacing: From ½ channel depth to 2 times channel depth

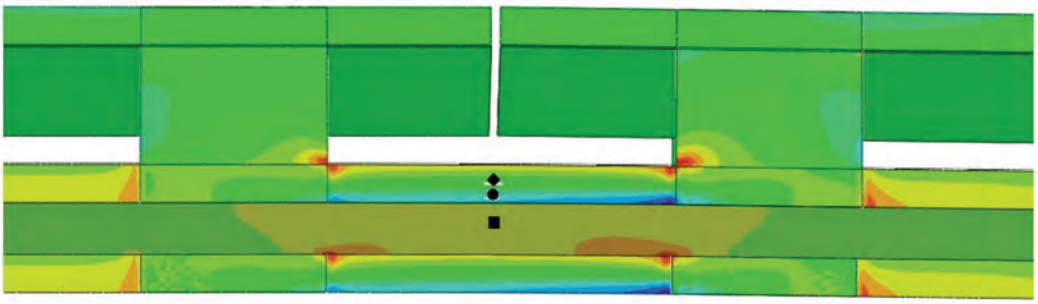

Fig. 15. Benchmark FEM showing location of the severed half and stress hotspots at load equal to 300 kips.

- Panel length—referring to the distance between two adjacent gusset joint centerlines: From 20 to 40 ft
- Stay plate thickness: From ⅜ to ⅞ in.
- Stay plate length: From ½ channel depth to 2 times channel depth
- Stay plate clear spacing: From 18 to 148 in.
- Gusset plate thickness (for noncontinuous only): From ⅜ to ⅞ in.
- Location of failures: Next to the gusset vs. centered between gussets at mid-panel

The laced members were always modeled with end stay plates. Based on results for the stay-plated members, the thickness and length parameters of the end stay plates were not varied. Additionally, results for the stay-plated members also showed that gusset plate thickness for the noncontinuous members had negligible effect and therefore was not varied for the laced members. The parameters considered for laced members included:

- Boundary conditions: Fixed vs. pinned
- Channel spacing: From ½ channel depth to 2 times channel depth
- Panel length—referring to the distance between two adjacent gusset joint centerlines: From 20 to 40 ft
- Lacing bar thickness: From ⅛ to ¾ in.
- Lacing bar length: Dependent on lacing bar spacing and channel spacing
- Lacing bar spacing—referring to the distance between connecting rivets to the channel flange, which determined the lacing angle relative to the channel: From ½ channel depth to 2 times channel depth
- Location of failures: Next to the gusset vs. centered between gussets at mid-panel

Boundary conditions were found to have a significant effect on results for noncontinuous members, which is discussed in greater detail later. Three sizes of rolled channels were considered; however, not all sections were considered for all combinations of parameters. They are sketched to scale in Figure 16 to give a sense of relative sizes. C15×50 is the largest rolled channel section currently available, so it was selected to learn if parametric effects varied between it and the next size smaller. C15×40 was chosen because in the authors' experience, it is the most commonly used rolled channel section for tension elements in legacy bridges. It is noted that a C15×40 was used to construct the Winona Bridge from which the two test specimens were obtained for the present research. The C8×11.5 was selected as a channel that is most likely representative of the smallest useable size channel for bridges. While this size channel probably would not be found on railroad bridges, it could be

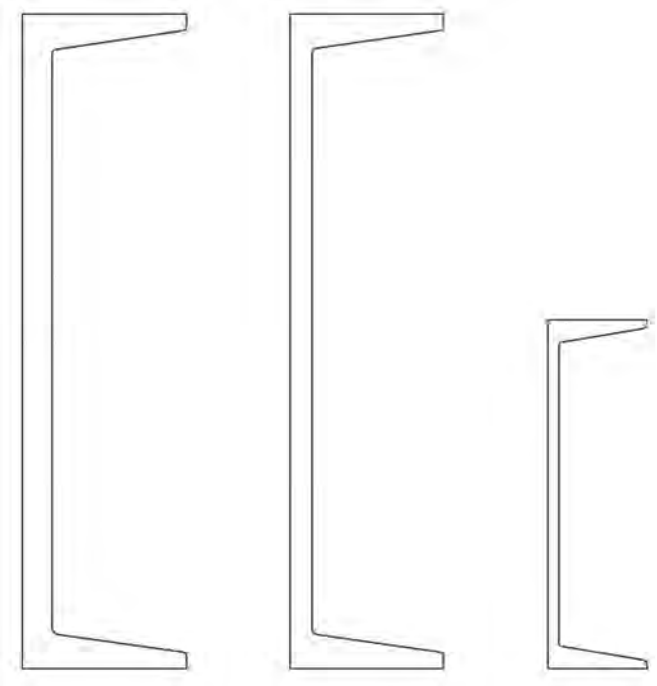

Fig. 16. Channel sections included in the parametric study.

possible for short span highway bridges as shear diagonals or hangers.

Gusset plates were modeled for the noncontinuous members, as discussed later. The thickness of the gusset plates was modeled as ⅜ and ⅞ in. to bound the limits of typical gusset plate thickness. The location of the failure within a member was also examined for the effect on results. Two locations were studied for all geometries, which included one at the mid-panel location centered between the gusset connections, and the other was adjacent to gusset plates located between the end stay plate and the gusset connection, thereby conservatively removing the benefit of the stay plate. This was considered for the continuous, as well as the noncontinuous types.

Definition of Eccentricity Parameter, **e**

Figure 17 illustrates the dimension "*e*" used in the post processing of data from the parametric study. 2*e* represents the distance between the centroids of individual channels that make up a two-channel member cross section. For the purposes of this paper, *2e* is referred to as the "channel spacing." Hence, *e* is the distance from the unfaulted *member centroid* to the centroid of an individual channel within that cross section. The figure further illustrates how 2*e* for two members that are comprised of the same size of channels with the same web-to-web spacing, but in reversed orientation, may differ from each other. The parametric study included some channels in both orientations. All results discussed in the following used the appropriate nominal moment, *Pe*, to normalize the second order moment resulting from failure of a single channel; where *P* is the total load in the member. In this way, a simplified method to calculate the resulting after-fracture, secondary moments in two-channel members as a percentage of *Pe* was developed.

Rotational Stiffness of Joints for Continuous and Noncontinuous Two-Channel Members

End boundary conditions were the most influential parameter affecting the resulting second-order moments in noncontinuous two-channel members in the faulted condition. The applied end boundary conditions were effectively inconsequential for continuous members due to rotational stiffness provided by the continuity of the channels. Varying boundary conditions were modeled for each geometry, including a noncontinuous member with pinned ends, a noncontinuous member with fixed ends, a three-span continuous member with pinned ends, and a three-span continuous member with fixed ends. It was observed that the percent *Pe* for the noncontinuous member with pinned boundary conditions differed as much as 10 times more than the same geometry with fixed boundaries. Continuous members had similar results to fixed noncontinuous members and were found to be insensitive to end boundary conditions. Continuity of the channels through the panel points provided rotational constraint that approached fixed boundary conditions. No additional rotational constraints were added at the interior panel points of the three-span members. However, they did have displacement constraints simulating bracing points of connection that would exist on an actual bridge to prevent out-of-plane displacement.

Primary and secondary members—including chords, floor beams, diagonals, lateral braces, sway braces, and bearings—tie into panel points on a truss that are typically connected using gusset plates. Chords or diagonal members will contribute some level of restraint for the joint against rotation (in all three axes and against torsion), particularly under tension. Other members such as lateral bracing and sway bracing may also help to restrain against rotation of the gusset connection. Floor beams, often with full-depth connections, increase rotational constraint of the connection. In some cases, fixed bearings, or even guided expansion bearings designed to only displace longitudinally, could offer further resistance to rotation for the gusset connections at supports. The combined restraint provided by all these members is difficult to estimate without finite element analysis of each individual bridge and member geometry, which would not be feasible for most bridge owners, nor was it the desired outcome of this research. However, the potential for there to be an effect of the rotational stiffness

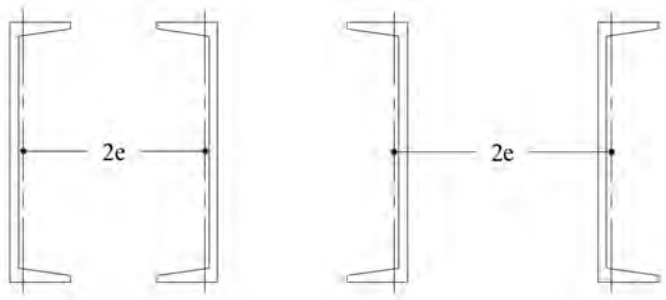

*Fig. 17. Illustrations showing eccentricity "*e*" used in development of the simplified evaluation method for two-channel members.*

on the after-fracture behavior of two-channel members was obvious. It was clear that pinned conditions would not exist in actual bridges. However, it would be problematic to justify perfectly fixed conditions, as well.

Consider further that diagonal and vertical two-channel members are usually "deeply" connected into gusset plates; often they would be trimmed such that they fit tightly into the connection to within a few inches of the other intersecting primary members. An example of this is shown in Figure 18, which shows a removed railroad deck truss joint with diagonal two-channel members connected into the gusset plates to within a couple inches of the continuous tension chord. Due to the rotational stiffness of the connection for reasons previously stated, it was suspected that most rotation experienced by a two-channel member would likely be due to local flexure of the gusset plates near or at the edges of the gusset plates. The plates themselves would behave as fixed toward the center of the connection. Thus, the concept was modeled by tying the channels to a set of gusset plates and then applying fixed boundary conditions to the free edges of the gusset plates. In this way, generous flexibility of the gusset plate was allowed while simultaneously providing a reasonable level of rigidity at the edge of the gusset plate modeling the interaction of intersecting members within the joint.

A pilot parametric study was carried out to determine how best to model the end boundary conditions of the noncontinuous members without overestimating joint rotational stiffness. The parameters considered in the pilot study included the effective portion of the gusset plate, the member embedment depth into the gusset plate, the gusset length beyond the member, and the gusset plate thickness. Figure 19 shows an illustration of these parameters. Two different effective areas of gusset were examined: a simple rectangular shape shown on the left and a Whitmore section-like shape shown on the right. The member embedment depth was evaluated looking at depths ranging from half the channel depth to two times the channel depth. The gusset plate length beyond the member, labeled *L* on the figure, also ranged from half the channel depth up to two times the channel depth.

Figure 20 plots the results of the rotational stiffness parametric study. Green dots represent values resulting from mid-panel failures. Black dots represent values resulting from failures near the gusset connections, such as those labeled in Figure 19. The rectangular and Whitmore-like effective gusset plate shapes are both represented in the data. The chart on the left plots the percent of *Pe* on the vertical axis and the member embedment depth into the gusset plate, normalized by the channel depth, on the horizontal axis. The chart on the right plots the same vertical axis and the gusset plate length, *L*, on the horizontal axis. By quadrupling the embedment depth, the percent *Pe* only increased by 2% for failures near the gusset plate and by less than 1% for mid-panel failures. By quadrupling the gusset plate length, *L*, the percent *Pe* increased by less than 1% for both failure locations. The final parameter considered was the thickness of the gusset plates. ⅜-in.-thick gusset plates are the thinnest plates used in bridges. The thickest plate is unknown. Several noncontinuous models were analyzed

Fig. 18. Example of deeply set diagonal members connected into a gusset plate.

varying only the gusset plate thickness from ⅜ in. to ⅞ in. It was found that results differed by 3% or less.

The rotational stiffness study concluded that outcomes were insensitive to the shape of the gusset assumed to be engaging in rotational constraint, the member embedment depth, the gusset plate length *L*, and the gusset plate thickness. As a result, noncontinuous FEMs were modeled in the primary parametric study using ⅜-in.-thick rectangular gusset plates with embedment depths and gusset plate lengths equal to the channel depth.

Finally, when percent *Pe* results shown in Figure 20 were compared back to previous model results with varying end boundary conditions, it was observed that by adding the gusset plates to the noncontinuous members, percent *Pe* fell between results for pinned and fixed boundary conditions, more closely resembling that of fixed boundary conditions and comparable to the continuous members. It is believed that this method of analysis reasonably and conservatively simulates typical boundary conditions on actual bridges for the noncontinuous two-channel members, which has a significant effect on the internal redundancy evaluation.

Results for Parametric Study of Two-Channel Members

The largest resulting second-order moments were always located in the intact member directly across from the location of failure. The largest of these moments nearly always resulted from a failure between the gusset plate and end stay plate, particularly for stay-plated members. Figure 21 shows the plan view of several FEMs with exaggerated deflections to illustrate general behavior. Two failed at the mid-panel, (a) and (b), and two failed between the gusset plate and end stay plate, (c) and (d). Overall global behavior was relatively

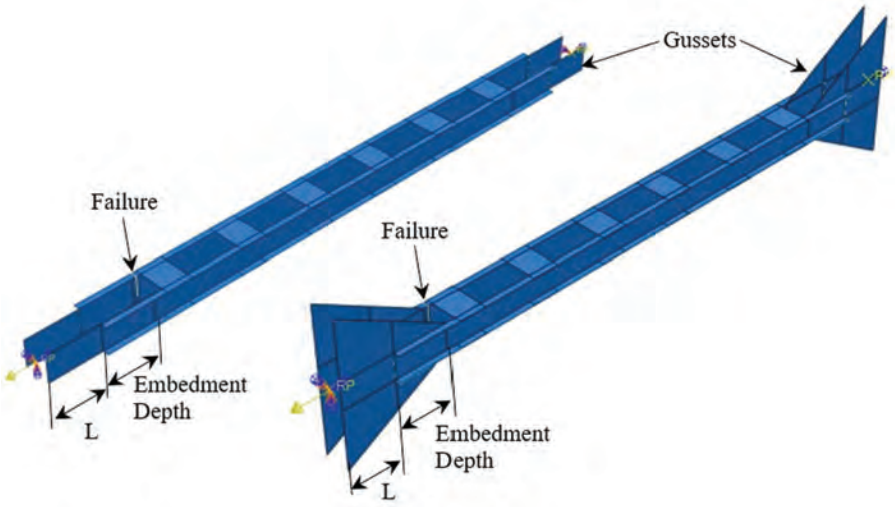

Fig. 19. Example of FEMs used to study gusset connection parameters: (left) rectangular gusset; (right) Whitmore gusset.

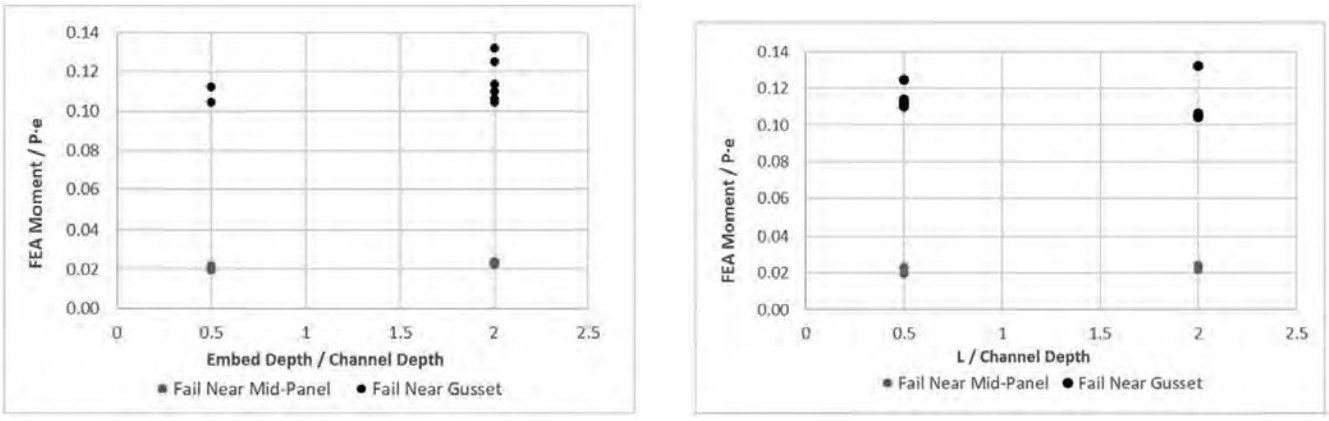

Fig. 20. Effects of the member embedment length (left) and gusset length, L (right).

similar between these two member types when they had failures at the same location. Mid-panel failures allowed moment distribution along the length of the intact channel via lattice bars or stay plates helping to distribute load more gradually around the failure. Gusset-end stay plate failures, however, forced much of the resulting moment to be resisted within a more localized area. Deflections across the remainder of the member were relatively gradual, as can be seen in Figure 21(c) and (d).

Moments integrated at the mid-panel of members with gusset-end stay plate failures were found to be very small compared to moments at the end stay plate near the failure. Stay-plated members were also observed to experience localized reverse curvature at the edges of the stay plates that produced hot spots of stress and amplified moments, as shown amplified in Figure 22. All moments reported in the following sections were taken near the edges of stay plates, when applicable, to capture the largest resultant moment. The opening of the fracture plane was resisted through in-plane shear in the stay plates. Laced members also benefited from in-plane shear resistance provided by end stay plates.

The size of the channel was found to have a negligible effect on outcomes. This makes sense when considering that loads were proportioned to the area of the member and that second-order effects resulting from load redistribution were a function of eccentricity created when half the member was severed. Thus, a smaller channel carried proportionally smaller loads and would be proportionally spaced, as well, causing similar behavior but on a smaller scale. This means that when the results were plotted as a ratio of the second-order moment (caused by the load redistribution) to the nominal moment, Pe, the results for the larger

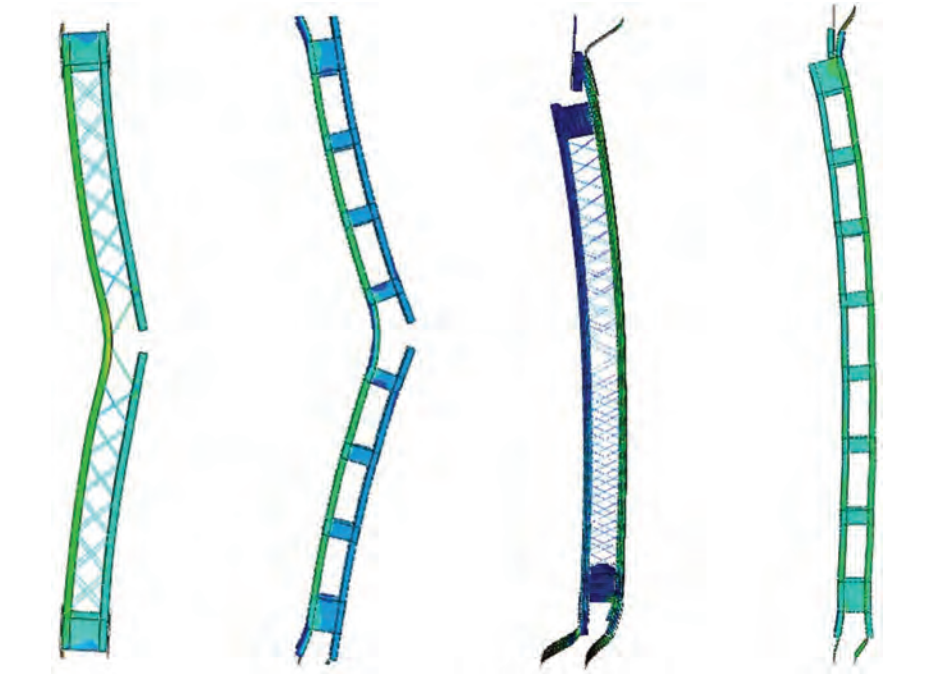

(a) Laced with mid-panel failure

(b) Stay-plated with mid-panel failure

(c) Laced with end failure near gusset

(d) Stay-plated with end failure near gusset

Fig. 21. Noncontinuous FEM results with deformations amplified 50 times for clarity.

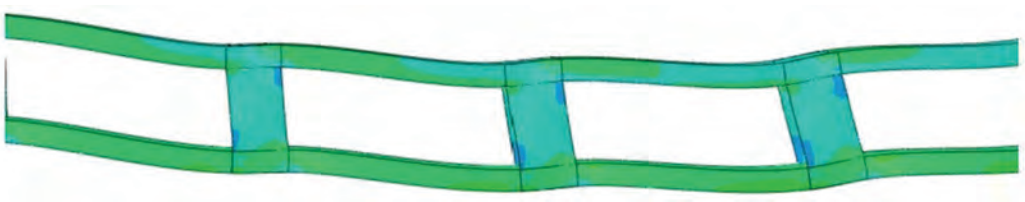

Fig. 22. Close-up of stay-plated member with deformations amplified 50 times, showing reverse curvature of the channels.

and smaller channel sections were nearly indistinguishable. This was the result for both continuous and noncontinuous members.

In addition to channel size, the spacing between channel pairs was studied. This parameter ranged from a spacing equal to half the depth of the channel up to two times the depth of the channel. When resulting second-order moments were normalized by the theoretical moment, *Pe*, then it appeared that as the spacing increased, the resulting moment decreased. However, when the second-order moments were not normalized, and instead absolute magnitudes were compared for geometries having different channel spacing, then it became clear that channel spacing had negligible effect on the results. The larger theoretical moment (i.e., *Pe*) was simply reducing the ratio of FEA moment to theoretical moment, due to the larger eccentricity, *e*.

This observation goes against the assumption that when one of the components fails the resulting second-order moment is equal to the original load times the faulted member eccentricity. The present parametric study found that such an assumption would be overly conservative for any two-channel geometry; as the spacing between components increased, that assumption would become increasingly overly conservative.

The panel length, which refers to the distance taken from centerline of a panel point to centerline of the next panel point for continuous members, or the length of the channels themselves for noncontinuous members, was found to have negligible effect on the after-fracture moment. Due to the localized curvature of the channels at the edges of stay plates that generated hotspots in the intact channel, longer spans having similar clear distances between stay plates were observed to have negligible effect. For laced members there were negligible increases in the resulting moments with longer member lengths. For example, doubling the panel length in some cases increased the after-fracture moment by 2%.

The thickness and length of the stay plates had negligible effect on the results. The thickness of the plates ranged from ⅜ to ⅞ in. The lengths of the plates ranged from half the depth of the channel to two times the depth of the channel. This range included a mixture of end and intermediate stay plates that would have exceeded known minimum design provisions. However, the results were insensitive to these changes in stay plate parameters. Existing design provisions also state that each plate must be fastened to the flanges of primary components with a minimum of three rivets per side. This type of connection would offer in-plane rotational constraint engaging the stay plates in resisting opening of the failed component as was observed during experimental testing.

In the FEMs, the connection was modeled using surface-to-surface tie constraints between shell elements, which constrained displacements and rotational degrees of freedom. Hence, modeled rotational constraint would be similar to that found on real structures, though most likely stiffer since slip at the highest loads on a riveted connection would not be allowed with the tie constraint such as was observed to occur on Specimen 1 in the laboratory test. The consequence of having stiffer stay plate connections is a larger localized transferal of moment into the intact channel. This means any difference in the FEM results caused by stiffer stay plate connections would have a conservative effect on the simplified solutions. However, it is important to keep in mind that laboratory testing showed that slip at the stay plates did not occur until near peak loads were reached, well beyond original design loads, and only for Specimen 1 when cut near the gusset connection. Specimen 2 showed no evidence of yielding and very minor evidence of slip at completion of testing in the stay plates adjacent to the failure location. The effectiveness of the stay plates in load redistribution is directly dependent upon the rotational constraint. This implies that stay plates have a minimum length to remain effective, but anything equal to or greater than half the depth of the channels to which they are attached with a minimum of three fasteners will effectively redistribute load. End stay plates were found to slightly reduce moments near the gusset connections for laced members but did not affect the secondary moment at the mid-panel location for mid-panel failures.

The number of stay plates within a given panel length was also studied and found to have a negligible effect. Smaller clear distances between stay plates resulting from increasing the number of stay plates, produced stiffer sections of channel between plates. Tripling the number of stay plate pairs was found to increase results by only 2–5%.

Lacing bar thickness, length, and spacing were investigated for their effect on laced two-channel members. Lattice bars sizes ranged from ⅛ to ¾ in. thick. Lattice fastener spacing ranged from half of the channel spacing to two times the channel spacing. Early design provisions limited the lattice spacing to about 45°, which would be equal to the channel spacing. The same provisions also called for a lattice thickness-to-length ratio of no more than 1/60. The parametric study varied this ratio from 1/169 to 1/28. It was found that these parameters all had negligible effects. One model was also analyzed in which the lattice bars were completely removed so that it only had the end stay plates. When the failure was at the mid-panel location of the member, the resulting moment at the location of the failure was reduced by about half compared to the same geometry with lattice bars, but the moment at the end stay plate was unaltered. When the failure was located between the end stay plate and the gusset connection of the member without lattice bars, the resulting moment at the mid-panel location was unchanged and the moment at the location of failure increased, going from 5% to about 9% of *Pe*. This behavior

suggests that while the lattice may support some limited load redistribution, it is not critical to performance of the member in the faulted condition. This also suggests that even though the parametric study focused on double lattice with fastened intersections, less robust systems of lattice, such as single lattice, would not be expected to affect results significantly. This comparison suggests that the simplified method of analysis resulting from the parametric study can be used for laced members of all kinds—that is, double or single lattice configurations.

The final parameter studied was the location of the failure. It included the mid-panel location and a location between the end stay plate and the gusset plate connections. Figure 23 shows four examples, one from each of the locations for each type of member. Figure 23(a) is failed between the end stay plate and gusset plate on a laced member. Figure 23(b) is failed between the end stay plate and gusset plate on a stay-plated member. Figure 23(c) shows the mid-panel failure for a laced member where the two lattice bars that would have connected into the location of the failure have been removed to facilitate convergence of the finite element solution. This was done for all laced member mid-panel failure models. Figure 23(d) shows a typical mid-panel failure for the stay-plated members. The resulting moment in laced members was not significantly affected by the location of the failure. This means that the resulting moment was always largest at the location of failure; however, the magnitude was not necessarily larger for mid-panel failures versus failures near the gusset plate. The same cannot be said for stay-plated types. It was found that failures near the gusset connection for both continuous and non-continuous stay-plated members resulted in moments that were two to three times larger than for the same geometry failed near mid-panel point. There were a few exceptions to this observation, so most models were analyzed two times, once with a failure at each location to ensure the worst-case scenario was captured for a given geometry. Plots of the percent of *Pe* in the following sections include results for both failure locations, which is the primary source of the data scatter.

Simplified Solution for Continuous Stay-Plated Two-Channel Members

Figure 24 compiles the results for all continuous, stay-plated models analyzed. The vertical axis is the finite element analysis moment divided by the theoretical moment, *Pe*. The horizontal axis is a combination of geometric properties used to correlate the results for the simplified solution. They offer simplistic inputs available to the engineer without refined analysis that can be readily taken from field

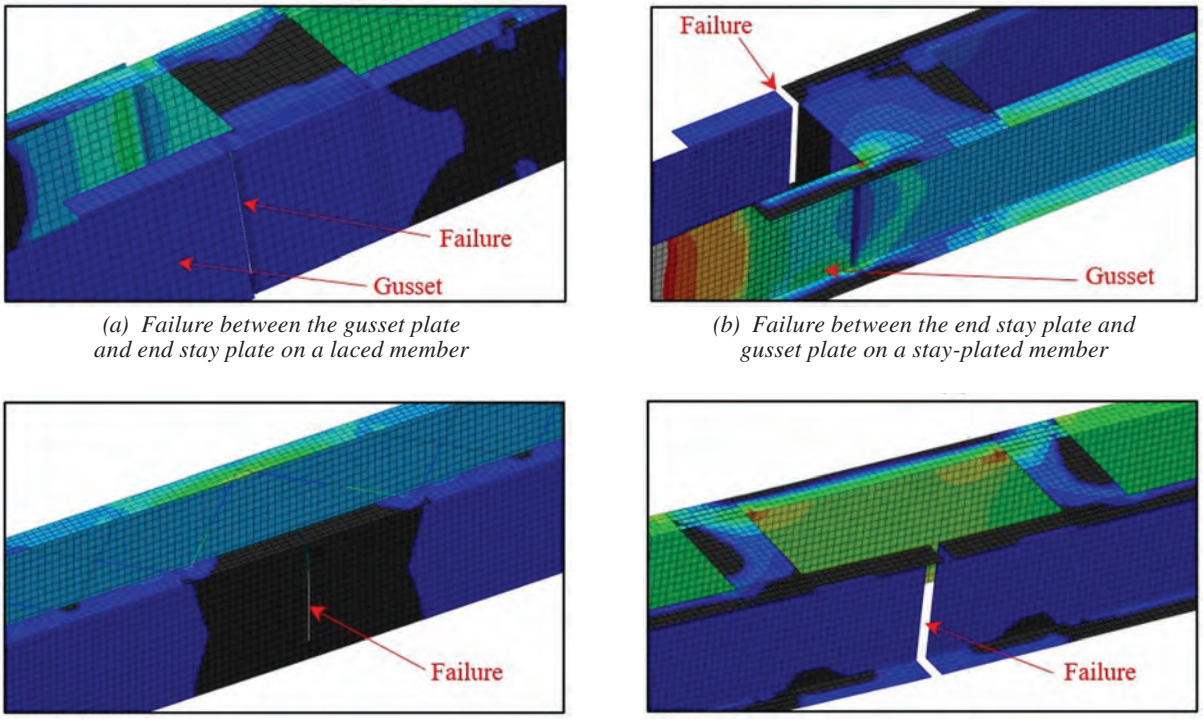

(a) Failure between the gusset plate and end stay plate on a laced member

(b) Failure between the end stay plate and gusset plate on a stay-plated member

(c) Mid-panel failure on a laced member

(d) Mid-panel failure on a stay-plated member

Fig. 23. Images depicting failure locations for stay-plated and laced two-channel members.

measurements or design drawings. The correlation includes the number of stay plate pairs (meaning a pair of plates located at the top and bottom of the member at the same cross section) within a single panel length, which includes the two end stay plate pairs and all intermediate stay plate pairs on the section of the member being evaluated, times the ratio of the channel depth to the channel spacing. The data plotted include all failure cases, both adjacent to the gusset plates and at the mid-section of the member. Failure cases closest to the gussets typically resulted in larger after-fracture moments, which is the primary cause for the scatter. The data show that an assumption of a secondary moment being generated equal to the axial load in the member times the eccentricity of the faulted member, or *Pe*, is overly conservative. As can be seen in Figure 24, most data were less than 10% of the *Pe* moment, with the most extreme case being less than 25%. Due to the regression analysis producing an equation fit to the maximum moments, the use of Equation 1 will provide a conservative estimate of the after-fracture moment.

Regression analysis was used to conservatively fit a line to the maximum values. The line is defined by Equation 1, which can be used to calculate the second-order moment resulting from a failed channel in a continuous, stay-plated, two-channel member.

$$M_{AF} = \frac{P_u e}{120}\left(\frac{N_{SP} d_{CH}}{2e} + 3\right) = \frac{P_u N_{SP} d_{CH} + 6P_u e}{240} \quad (1)$$

where

M_{AF} = after-fracture moment resulting from failure of a channel in a two-channel member (kip-in.)

P_u = total factored axial load (kips)

N_{SP} = number of stay plate pairs (1 pair equals the top and bottom stay plates at the same cross section) within the span of the member between the panel points

d_{CH} = depth of the channels (in.)

e = distance measured from the centroid of the unfaulted two-channel member to the centroid of the intact channel in the faulted state (in.); see Figure 17.

The resulting after-fracture moment is inserted into Equation 5 to calculate the after-fracture net section stress used to determine the remaining fatigue life. The individual results of each FEM can be viewed in the appendix reported by Lloyd et al. (2019).

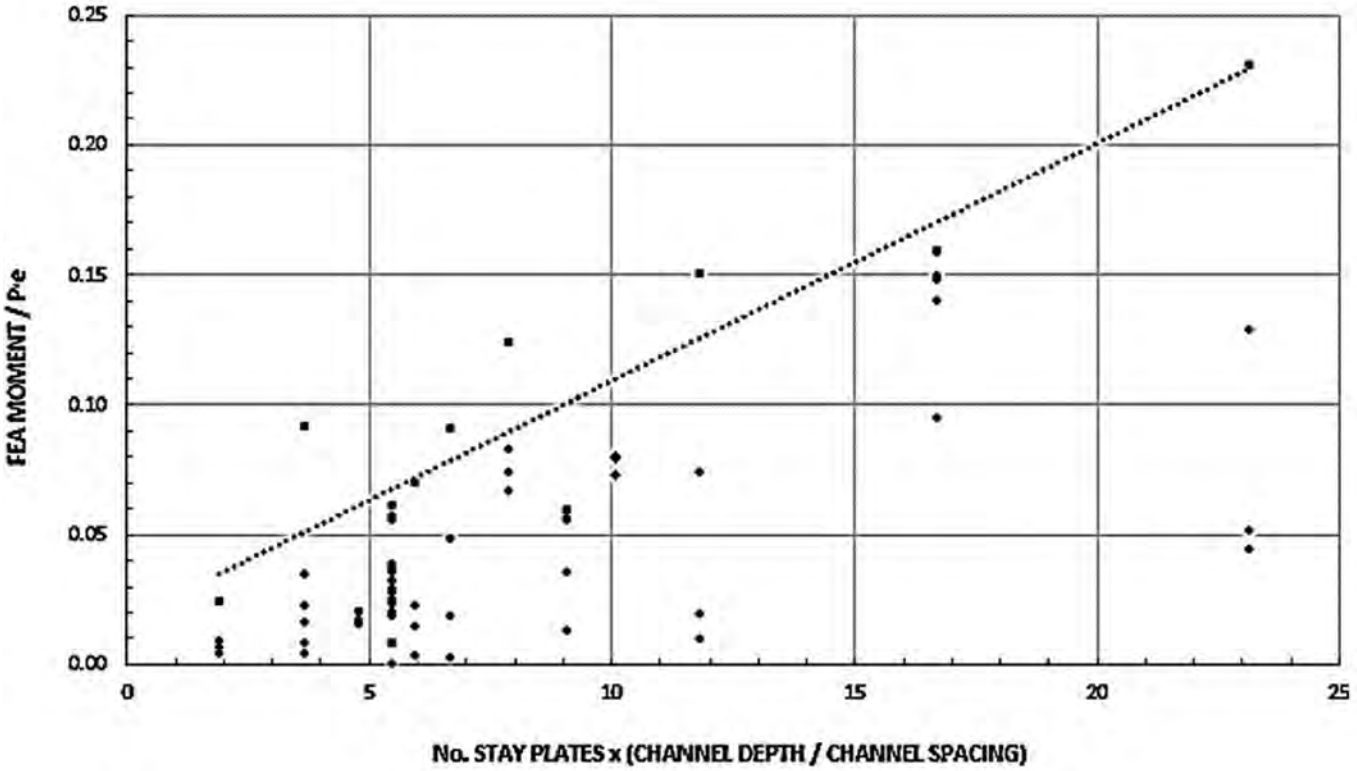

Fig. 24. Plot of results for continuous stay-plated two-channel members.

Simplified Solution for Continuous Laced Two-Channel Members

Figure 25 compiles the results for all continuous, laced models analyzed. The vertical axis is the finite element analysis moment divided by the theoretical moment, *Pe*. The horizontal axis is a combination of geometric properties used to correlate the results for the simplified solution. The parameters plotted offer simplistic inputs available to the engineer without refined analysis that can be readily obtained from field measurements or design drawings. These correlation parameters include the length in inches from the centerline of a panel point to the centerline of the next panel point divided by the lattice spacing, times the ratio of the channel depth to the channel spacing.

Regression analysis was used to conservatively fit a line to the maximum values. The line is defined by Equation 2, which can be used to calculate the second-order moment resulting from a failed channel in a continuous, laced, two-channel member. The lattice bar configuration factor, γ_{LB}, accounts for the difference between single lattice bar and double lattice bars spacing. Equation 2 was derived using double lattice bar spacing. Based on results for members where the lattice was removed, the simplified method can be extended to single lattice configurations, as well. Thus, the lattice bar configuration factor reduces the spacing of single lattice bar members to an equivalent double lattice bar spacing such that the moment is not incorrectly doubled for single lattice members. Finally, as can be seen in Figure 25, the maximum moment reaches a plateau of less than 14% of *Pe* for all modeled geometries, including the most extreme geometric cases studied (i.e., longest and narrowest member configurations). Therefore, Equation 2 puts a practical limit on the moment of 0.15*Pe*. The data plotted include all failure cases (i.e., adjacent to the gusset plates and at the mid-section of the member). Unlike for stay-plated members, laced member failure cases closest to the gussets were not necessarily observed to produce larger after-fracture moments. Hence, the data scatter is reduced for laced member types. The data further illustrate that an assumption of a secondary moment being generated equal to the axial load in the member times the eccentricity of the faulted member, or *Pe*, is overly conservative. As can be seen in Figure 25, most data were less than 10% of the *Pe* moment, with the most extreme cases staying below 14%.

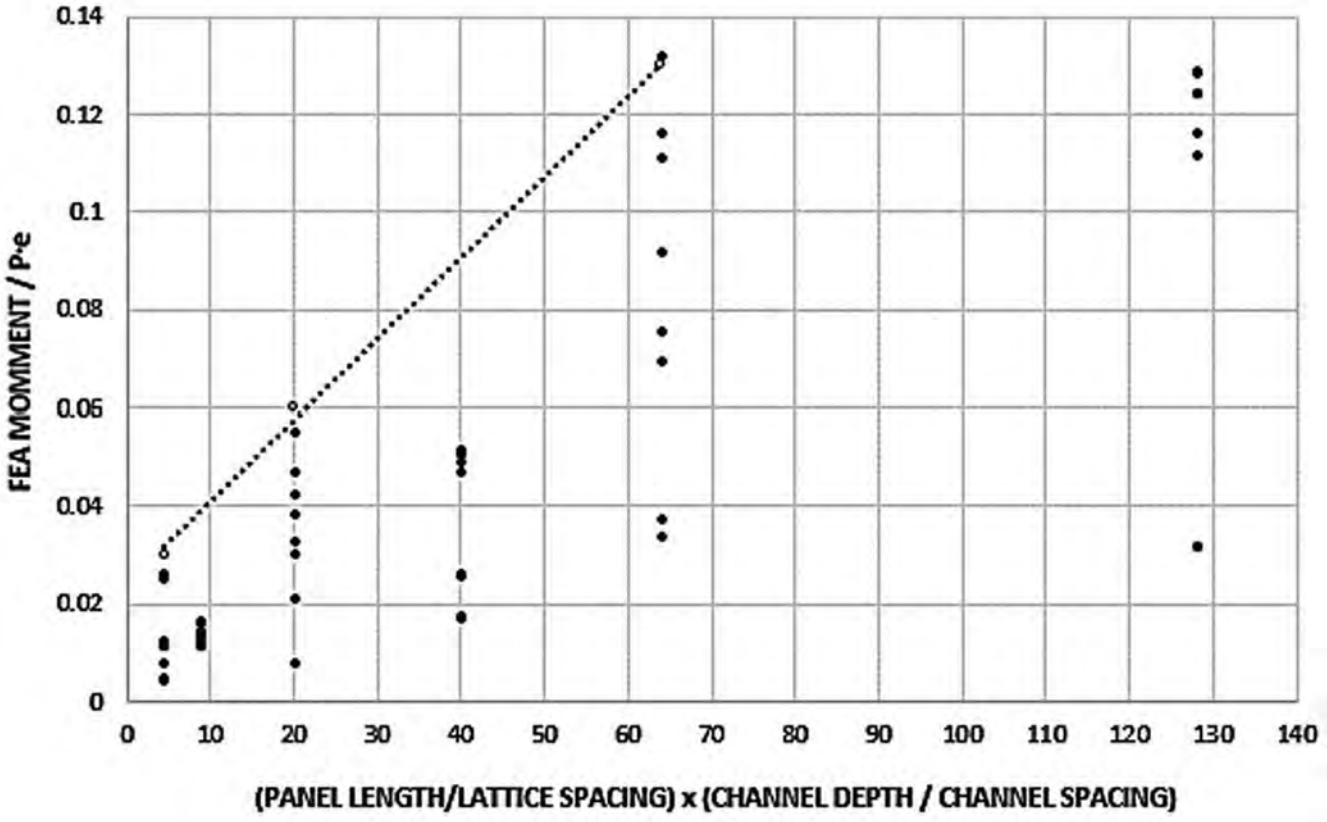

Fig. 25. Plot of results for continuous laced two-channel members.

Due to the regression analysis producing an equation fit to the maximum moments, the use of Equation 2 will provide a conservative estimate of the after-fracture moment.

$$M_{AF} = \frac{P_u e}{590}\left(\frac{L_{PL} d_{CH}}{\gamma_{LB} S_{LB} 2e} + 14\right) \tag{2}$$

$$= \frac{P_u L_{PL} d_{CH} + 28 P_u e \gamma_{LB} S_{LB}}{1{,}180 \gamma_{LB} S_{LB}} \leq 0.15 P_u e$$

where

L_{PL} = length of the panel measured between the centerlines of two panel points (in.)

M_{AF} = after-fracture moment resulting from failure of a channel in a two-channel member (kip-in.)

P_u = total factored axial load (kips)

S_{LB} = spacing of the lattice bars measured longitudinally between centerlines of fasteners connecting the lattice bars to a channel flange (in.)

d_{CH} = depth of the channels (in.)

e = distance measured from the centroid of the unfaulted two-channel member to the centroid of the intact channel in the faulted state (in.); see Figure 17.

γ_{LB} = lattice bar configuration factor; 1.0 for double lattice, 0.5 for single lattice

The resulting moment is inserted into Equation 5 to calculate the after-fracture net section stress used to determine the remaining fatigue life. The individual results of each FEM can be viewed in the appendix reported by Lloyd et al. (2019).

Simplified Solution for Noncontinuous Stay-Plated Two-Channel Members

Figure 26 compiles the results for all noncontinuous, stay-plated models analyzed. The vertical axis is the finite element analysis moment divided by the theoretical moment, *Pe*. Once again, the horizontal axis is a combination of geometric properties used to correlate the results for the simplified solution. Again, these parameters are based on input data that are readily available to the engineer without refined analysis that can be easily obtained from field measurements or design drawings. It is the number of stay plate pairs (meaning a pair of plates located at the top and bottom of the member at the same cross section) along the entire length of the member, which includes each of the two end stay plate pairs and all intermediate stay plate pairs on the section of the member being evaluated, times the ratio of the channel depth to the channel spacing.

Regression analysis was used to conservatively fit a line to the maximum values. The line is defined by Equation 3, which can be used to calculate the second-order moment resulting from a failed channel in a noncontinuous, stay-plated, two-channel member. The moment is limited to 0.35*Pe*, which is slightly above the maximum value observed for the continuous laced member geometries

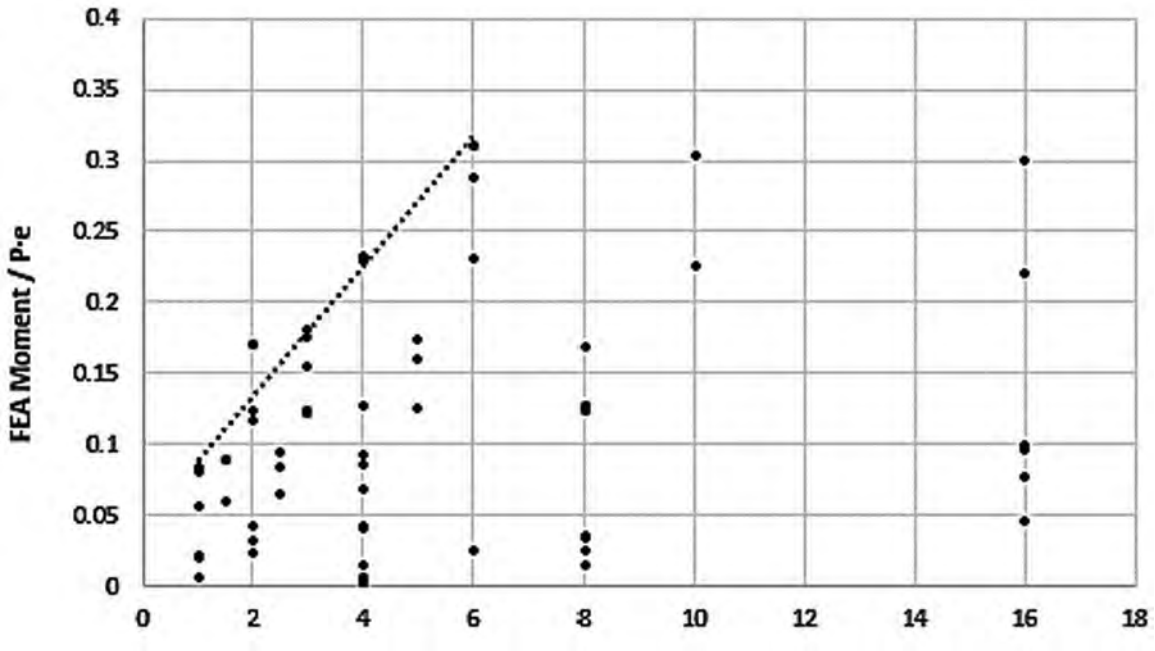

Fig. 26. Plot of results for noncontinuous stay-plated two-channel members.

studied, as can be seen in Figure 26. The maximum after-fracture moments for the noncontinuous stay-plated members were generally larger than those for the continuous stay-plated members by approximately 15–20%. The continuous stay-plated members benefited from the continuity across nodes through which they could distribute moment, whereas the noncontinuous types were forced to carry the entire after-fracture moment within the intact channel at the location of failure without benefit of continuity.

$$M_{AF} = \frac{P_u e}{22}\left(\frac{N_{SP} d_{CH}}{2e} + 1\right) \tag{3}$$
$$= \frac{P_u N_{SP} d_{CH} + 2P_u e}{44} \le 0.35 P_u e$$

where

M_{AF} = after-fracture moment resulting from failure of a channel in a two-channel member (kip-in.)

N_{SP} = number of stay plate pairs (1 pair equals the top and bottom stay plates at the same cross section) within the span of the member between the panel points

P_u = total factored axial load (kips)

d_{CH} = depth of the channels (in.)

e = distance measured from the centroid of the unfaulted two-channel member to the centroid of the intact channel in the faulted state (in.); see Figure 17.

The resulting moment is inserted into Equation 5 to calculate the after-fracture net section stress used to determine the remaining fatigue life. The individual results of each FEM can be viewed in the appendix reported by Lloyd et al. (2019).

Simplified Solution for Noncontinuous Laced Two-Channel Members

Figure 27 compiles the results for all noncontinuous laced models analyzed. The vertical axis is the finite element analysis moment divided by the theoretical moment, *Pe*. The horizontal axis is a combination of geometric properties used to correlate the results for the simplified solution. They offer simple inputs that don't require advanced analysis tools. It is the length (in.) of the channels, including the depth into the gusset plate at each end of the member, divided by the lattice bar spacing, times the ratio of the channel depth to the channel spacing.

Regression analysis was used to conservatively fit a line to the maximum values. The data plotted include all failure

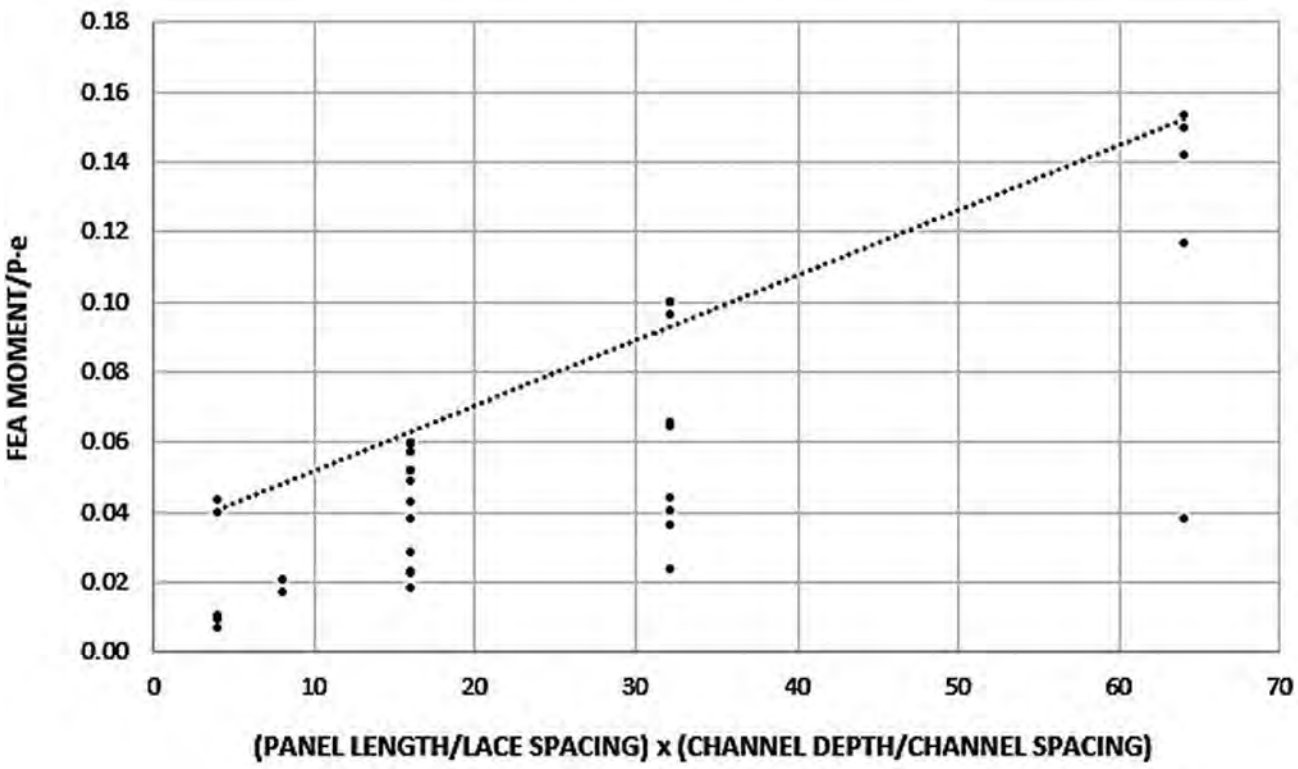

Fig. 27. Plot of results for noncontinuous laced two-channel members.

cases (i.e., adjacent to the gusset plates and at the mid-section of the member). Unlike for stay-plated members, laced member failure cases closest to the gussets were not necessarily observed to produce larger after-fracture moments. Hence, once again the data scatter is reduced for the noncontinuous laced member type. The data in Figure 27 further illustrate that an assumption of a secondary moment being generated equal to the axial load in the member times the eccentricity of the faulted member, or *Pe*, is overly conservative. As can be seen, most data were below 10% of a theoretical *Pe* moment, with the most extreme cases staying below 14%. Due to the regression analysis producing an equation fit to the maximum moments, the use of Equation 4 will provide a conservative estimate of the after-fracture moment. The line in Figure 27 is defined by Equation 4, which can be used to calculate the second-order moment resulting from a failed channel in a noncontinuous, laced, two-channel member. The lattice bar configuration factor, γ_{LB}, accounts for the difference between single lattice bar and double lattice bars spacing. Equation 4 was derived using double lattice bar spacing. Based on results for members where the lattice was removed, the simplified method can be extended to single lattice configurations, as well. Thus, the lattice bar configuration factor reduces the spacing of single lattice bar members to an equivalent double lattice bar spacing such that the moment is not incorrectly doubled for single lattice members.

$$M_{AF} = \frac{P_u e}{550}\left(\frac{L_{PL} d_{CH}}{\gamma_{LB} S_{LB} 2e} + 20\right) = \frac{P_u L_{PL} d_{CH} + 40 P_u e \gamma_{LB} S_{LB}}{1{,}100 \gamma_{LB} S_{LB}} \quad (4)$$

where

L_{PL} = length of the panel measured between the centerlines of two panel points (in.)

M_{AF} = after-fracture moment resulting from failure of a channel in a two-channel member (kip-in.)

P_u = total factored axial load (kips)

S_{LB} = spacing of the lattice bars measured longitudinally between centerlines of fasteners connecting the lattice bars to a channel flange (in.)

d_{CH} = depth of the channels (in.)

e = distance measured from the centroid of the unfaulted two-channel member to the centroid of the intact channel in the faulted state (in.); see Figure 17.

γ_{LB} = lattice bar configuration factor; 1.0 for double lattice, 0.5 for single lattice

The resulting moment is inserted into Equation 5 to calculate the after-fracture net section stress used to determine the remaining fatigue life. The individual results of each FEM can be viewed in the appendix reported by Lloyd et al. (2019).

Application of Parametric Study Findings for Two-Channel Members

The following describes implementation of the after-fracture moments, previously explained, to calculate the after-fracture net section stress resulting from failure of a channel in a two-channel member.

After-Fracture Net Section Stress Calculation

Following calculation of the after-fracture moment that results from failure of one of the two channels, Equation 5 is used to calculate the after-fracture net section stress. The equation combines the axial net section stress and second order flexural stress. The axial net section stress is the total factored load carried by the member in the unfaulted state, divided by the after-fracture net section. The flexural stress is the after-fracture moment calculated using one of Equations 1 to 4, as applicable for the member type, times the distance from the neutral axis to the point of interest, c, divided by the weak-axis moment of inertia, I_y, of the intact channel.

$$f_{AFN} = \frac{P_u}{A_{AFN}} + \frac{M_{AF} c}{I_y} \quad (5)$$

where

A_{AFN} = net section area of the member in the faulted state; this is equal to the net area of a single channel (in.^{2})

I_y = principal axis moment of inertia about the weak axis of a single channel (in.^{4})

M_{AF} = after-fracture moment resulting from failure of a channel in a two-channel member (kip-in.)

P_u = total factored applied tensile load (kips)

c = distance from the centroid of the channel to the surface of stress calculation (in.)

f_{AFN} = factored total net section stress in the faulted state (ksi)

Guidance for Use of Simplified Solutions for Two-Channel Members

The simplified method of analysis was developed considering failures at mid-panel and near the gusset connections capturing the largest resulting moments for the geometries analyzed. This means that a single after-fracture moment calculation and net section stress calculation need to be performed for each member. There is no need to repeat this calculation multiple times for different cross sections of the same member. Figures 28 and 29 illustrate two generic types of trusses where two-channel members could be used. Figure 28 shows a three-span continuous deck truss structure. Figure 29 depicts a single-span through-truss structure. Each figure has been highlighted with red and blue lines. The red lines indicate members that would be analyzed

using either Equation 1 (stay-plated) or 2 (laced) for continuous members. The blue lines designate members that would be evaluated using either Equation 3 (stay-plated) or 4 (laced) for noncontinuous members. Members that are *not* highlighted, or which appear black, are compression members that would not need to be evaluated for internal redundancy. Reversal zones that are subjected to both tensile and compressive live load stresses would also need to be evaluated. Notice that the terminating bottom chord of each truss is evaluated using equations for noncontinuous members. Due to the lack of continuity beyond the abutment at each end of a truss, the last panel should be analyzed using equations developed for noncontinuous members.

CONCLUSIONS

This paper summarizes the experimental and analytical research into behavior of mechanically fastened built-up axial steel members comprised of two rolled channels following fracture of a single channel. Previously performed and reported-on fracture tests verified cross-boundary fracture resistance (CBFR) of axially loaded built-up steel members as evidence that these member types can avoid full cross-section fracture in service (Lloyd et al., 2021). Finite element–based parametric studies were conducted to characterize the static load redistribution behavior of two-channel axial members following a fracture event. Finite element models (FEMs) were calibrated using experimental data obtained from full-scale testing. Simplified solutions were developed to estimate the after-fracture load capacity and the fatigue stress range in the remaining channel, accounting for second-order moments. The solutions can be applied to internal redundancy evaluations. If a member is found to be internally redundant, the solutions can then be used to reliably predict fatigue life of the member in the faulted state and establish the special inspection interval according to the provisions of AASHTO (2018).

The research concluded that mechanically fastened built-up axial members comprised of two rolled channels can possess sufficient strength and fatigue resistance after the failure of a single channel. After-fracture load redistribution behavior of two-channel members was found to result in a global out-of-plane flexural response in the surviving channel. Applied boundary conditions were significantly influential on some member types, driving separate simplified solutions for continuous and noncontinuous two-channel members. The derived solutions calculate the after-fracture, second-order moment carried by the surviving channel in combination with the original and redistributed axial loads. A verification exercise comparing results from the derived solutions back to full-scale experimental research predicted primary longitudinal stress to within a few percentage points of the measured values at locations of interest. As a result, it was concluded that the proposed method of analysis contained herein provides a simple, conservative, and efficient quantitative approach to perform the redundancy analysis and the prediction of the commensurate special inspection interval.

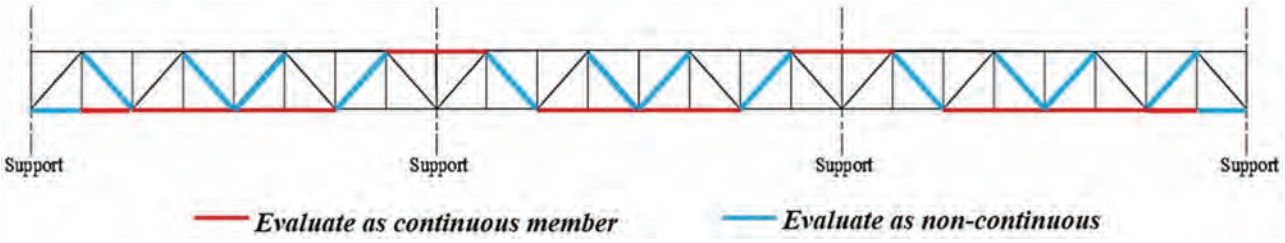

Fig. 28. Sketch illustrating correct application of Equations 1–4 on continuous trusses.

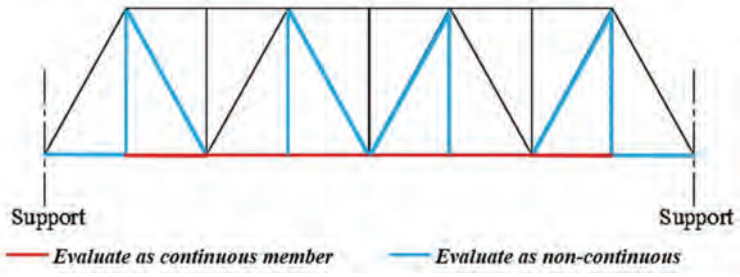

Fig. 29. Sketch illustrating correct application of Equations 1–4 on simple span trusses.

REFERENCES

AASHO (1935), *AASHO Standard Specifications for Highway Bridges*, 2nd ed., The American Association of State Highway Officials, Washington D.C.

AASHTO (2018), *AASHTO Guide Specifications for Internal Redundancy of Mechanically-Fastened Built-Up Steel Members*, 1st ed., American Association of State Highway and Transportation Officials, Washington D.C.

AASHTO (2020), *LRFD Bridge Design Specifications*, 9th ed., American Association of State Highway and Transportation Officials, Washington, D.C.

AREMA (2017), *AREMA Manual for Railway Engineering*, American Railway Engineering and Maintenance-of-Way Association, Lanham, Maryland

ASTM (2016a), *Standard Test Methods for Notched Bar Impact Testing of Metallic Materials*, ASTM E23, ASTM International, West Conshohocken, Pa.

ASTM (2016b), *Standard Test Methods for Tension Testing of Metallic Materials*, ASTM E8, ASTM International, West Conshohocken, Pa.

ASTM (2017), *Standard Test Method for Analysis of Carbon and Low-Alloy Steel by Spark Atomic Emission Spectrometry*, ASTM E415, ASTM International, West Conshohocken, Pa.

ASTM (2019), *Standard Specification for High Strength Structural Bolts and Assemblies, Steel and Alloy Steel, Heat Treated, Inch Dimensions 120 ksi and 150 ksi Minimum Tensile Strength, and Metric Dimensions 830 MPa and 1040 MPa Minimum Tensile Strength*, ASTM F3125/F3125M-19e2, ASTM International, West Conshohocken, Pa.

Campbell, L.E., Snyder, L.R., Whitehead, J.M., Connor, R.J., and Lloyd, J.B. (2019), "Probability of Detection Study for Visual Inspection of Steel Bridges: Volume 2—Full Project Report," Joint Transportation Research Program Publication No. FHWA/IN/JTRP-2019/22, Purdue University, West Lafayette, Ind. https://doi.org/10.5703/1288284317104

Connor, R.J., Dexter, R., and Mahmoud, H. (2005), *NCHRP Synthesis 354: Inspection and Management of Bridges with Fracture-Critical Details,* Washington D.C., p. 84.

Diggelmann, L.M., Connor, R.J., and Sherman, R.J. (2013), *Evaluation of Member and Load-Path Redundancy on the US-421 Bridge over the Ohio River*, Washington D.C.

FHA (1988), "National Bridge Inspection Standards," *Federal Register*, Vol. 53, No. 121, p. 23,611.

FHA (2022), "National Bridge Inspection Standards," *Federal Register*, Vol. 87, No. 88, p. 27,396.

Hebdon, M.H., Bonachera Martin, F.J., Korkmaz, C., and Connor, R.J. (2017), "Fracture Resilience of Steel Built-Up Members Subjected to Flexure," *Journal of Bridge Engineering*, ASCE. DOI: 10.1061/(ASCE)BE.1943-5592.0001059

Lloyd, J.B., Bonachera Martin, F.J., Korkmaz, C., and R.J. Connor (2021), "Internal Redundancy of Mechanically-Fastened Built-Up Steel Axially-Loaded Multi-Component Members," *Journal of Bridge Engineering*, ASCE. DOI: 10.1061/(ASCE)BE.1943-5592.0001743

Lloyd, J.B., Campbell, L.E., Bonachera Martin, F.J., and Connor, R.J. (2019), "Experimental and Analytical Evaluation of the Strength of Selected Truss Members from the Approach Spans of the Winona Bridge," Purdue University, West Lafayette, Ind. https://doi.org/10.5703/1288284316925

Mekker, M.M., Remias, S.M., McNamara, M.L., and Bullock, D.M. (2015), *Characterizing Interstate Crash Rates Based on Traffic Congestion Using Probe Vehicle Data*, Transportation Research Board, Washington, D.C. http://docs.trb.org/prp/16-1194.pdf

Ocel, J.M. (2013), NCHRP Web-Only Document 197: *Guidelines for the Load and Resistance Factor Design and Rating of Riveted and Bolted Gusset-Plate Connections for Steel Bridges*, Transportation Research Board, Washington D.C.

Seismic Performance of Embedded Column Base Connections with Attached Reinforcement: Tests and Strength Models

Ahmad S. Hassan and Amit M. Kanvinde

ABSTRACT

Embedded column base (ECB) connections used in mid- to high-rise steel moment frames derive moment resistance through bearing of the embedded column and base plate against the concrete footing. Five large-scale tests on ECB connections are presented; these feature cantilever columns subjected to axial compression and cyclic lateral loading. The tests feature reinforcement details including (1) horizontal reinforcement bars attached to the column (either directly welded to the flanges or in the form of U-hairpins wrapped around the column), and (2) vertical reinforcement in the form of stirrups in the footing. These tests complement previous experiments that are nominally identical but without the additional reinforcement. The tests indicate that while the horizontal reinforcement enhances moment strength due to resisting forces in the horizontal direction, it also produces a tension field that decreases the restraint to the rotation of the embedded base plate, ultimately reducing overall moment strength. The addition of vertical reinforcement in the form of stirrups mitigates this issue to an extent. A strength model considering these effects is proposed and shown to predict strength with good accuracy across a range of configurations, encompassing the different configurations of horizontal and vertical reinforcement. Limitations of the approach are discussed.

Keywords: base connection, moment frames, composite connection.

INTRODUCTION

Embedded column base (ECB) connections in seismically designed steel moment frames (SMFs) are commonly used to connect the steel columns to concrete foundations for mid- to high-rise buildings. Unlike low-rise buildings for which exposed-type base plate connections [where a base plate is welded to the column with anchor rods attached to the foundation, see Figure 1(a)] are suitable, in mid- to high-rise frames, the embedment is required to resist large base moments and provide fixity through bearing of column flanges against concrete, as shown in Figure 1(b). The column is usually welded to a base plate resting on a thin concrete layer for leveling purposes. Face-bearing plates are often used on the top of concrete surface to transfer axial compression and facilitate the formation of a shear panel similar to composite beam-column connections (ASCE, 1994).

Significant research has been conducted on exposed-type base connections, including large-scale experimental testing (Astaneh et al., 1992; Fahmy et al., 1999; Gomez et al., 2010; Kanvinde et al., 2015; Trautner et al., 2017; and Hassan et al., 2022), analytical (Wald, 2000), and computational simulations for both component (Inamasu et al., 2021; Hassan et al., 2022), and frame (Falborski et al., 2020), leading to the development of design considerations (Fisher and Kloiber, 2006; AISC, 2016; SEAOC, 2015). In contrast, research on ECB connections is sparse, with no experimentally validated strength characterization methods for design, and only limited finite element parametric studies (Pertold et al., 2000a, 2000b). Current design practice in the United States relies on adaptations of methods developed for other similar components such as composite beam-column connections (ASCE, 1994) and steel coupling beams embedded in concrete shear walls (Marcakis and Mitchell, 1980; Mattock and Gaafar, 1982; Harris et al., 1993; Shahrooz et al., 1993). The AISC *Seismic Design Manual* (AISC, 2018) applies the method developed by Mattock and Gaafar (1982) for coupling beams to the design of ECB connections. These adaptations disregard or inadequately incorporate behavioral aspects specific to ECB connections including (1) the effect of concrete confinement, which is limited in a shear wall or a composite beam-column connection; (2) the presence of a base plate welded to the column section; (3) the presence of axial load; and (4) differences in reinforcing bar patterns. Other studies on similar connections (Cui et al., 2009; Richards et al., 2018; Hanks and Richards, 2019) examined the effect of an overtopping slab-on-grade on top of an exposed-type column base connection. This type of connection (known as a blockout column base connection) is distinct from an

Ahmad S. Hassan, Designer, Degenkolb Engineers, Sacramento, Calif. Email: ahassan@degenkolb.com (Corresponding author)

Amit M. Kanvinde, Professor, Department of Civil and Environmental Engineering, University of California, Davis, Calif. Email: kanvinde@ucdavis.edu

Paper No. 2023-03

ECB connection in fundamental behavioral characteristics, wherein the concrete embedment due to the floor slab is incidental and the primary mode of moment resistance is similar to exposed-type base plate connections. As a consequence, behavioral characteristics of these connections are not readily applicable to ECB connections.

Previous experimental studies (Grilli et al., 2017) on ECB connections representative of U.S. construction practice—similar to that shown in Figure 1(b)—serve as the only test data available on the seismic performance of such connections. These five specimens featured wide-flange steel cantilever columns embedded within a concrete footing subjected to a cyclic lateral deformation history under a constant axial force (compression or tension). The specimens were designed with minimal longitudinal and transverse reinforcement such that observed failure modes and strengths were mainly associated with the concrete.

The results from this experimental program (Grilli et al., 2017; Grilli and Kanvinde, 2017), provided insights into the fundamental physics of the ECB connections, including failure modes that informed the development of strength models suitable for the design of ECB connections. Figure 1(b) shows the two primary mechanisms of moment resistance, as outlined by Grilli and Kanvinde (2017): (1) horizontal bearing stresses against the column flanges along with a complementary shear panel zone and (2) vertical bearing stresses resisting uplift of the base plate. Figures 2(a) and (b) show post-test photographs illustrating the failure modes observed from two specimens in the experimental program (Grilli et al., 2017) with different embedment depths. In

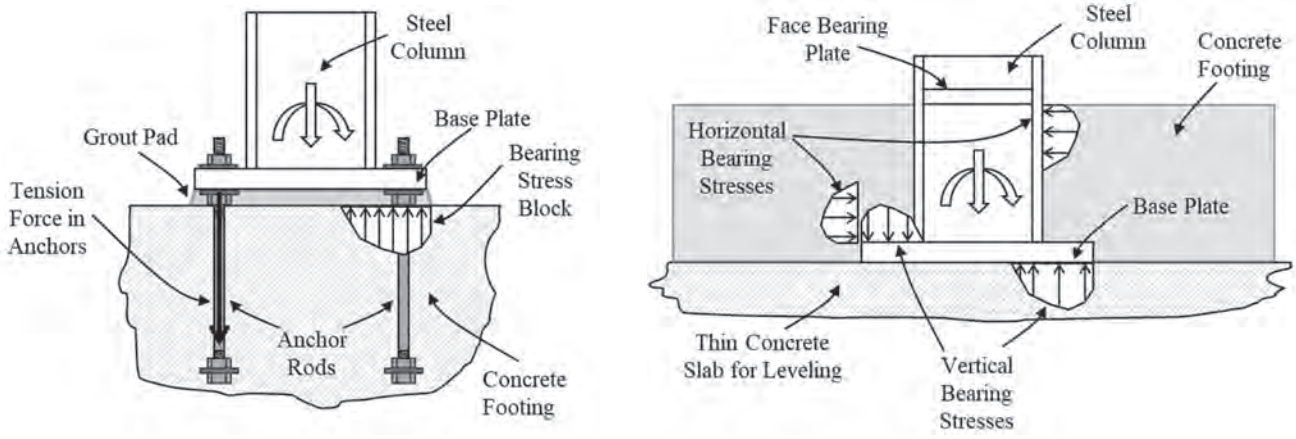

(a) Exposed-type connection *(b) Embedded-type (ECB) connection*

Fig. 1. Column base connections and force transfer mechanisms.

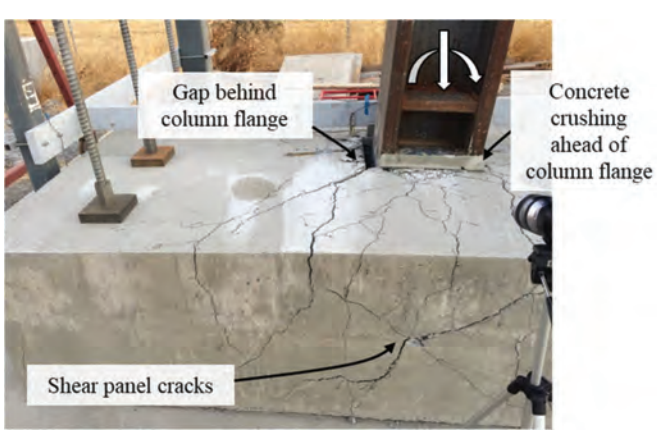

(a) Horizontal bearing

(b) Vertical bearing

Fig. 2. Experimental program (Grilli et al., 2017) damage patterns suggesting modes of failure/deformation governed by bearing mechanisms.

summary, the singular study on ECB connections is limited by a relatively small data set and the examination of a single detail. Specifically, the test series included only one generic detail [similar to Figure 1(b)] without any reinforcement attached to the column. As a result, the test data do not represent the effect of such reinforcement that is commonly used in practice.

Motivated by these issues, this paper presents a series of five large-scale experiments on ECB connections with attached reinforcement bars, representative of construction practice in the United States, along with a strength model. Figure 3 schematically illustrates the main features of the tested details developed in consultation with an oversight committee of practitioners and fabricators (see the Acknowledgments section). These details are similar to the one examined by Grilli et al. (2017), with the exception of reinforcement fixtures attached to the embedded column flanges. Two techniques for reinforcement attachment are examined—welded reinforcement bars to the column flange (deformed weldable bars commonly used in practice), as shown in Figure 3(a), and "U-bar hairpin" reinforcement bars (recommended by the AISC *Seismic Provisions* for steel coupling beams) anchored by the embedded portion of the column and alternating in direction to engage both column flanges, as shown in Figure 3(b).

CURRENT PRACTICE AND AVAILABLE STRENGTH MODELS

The AISC *Seismic Provisions* (AISC, 2016) and Design Guide 1 (Fisher and Kloiber, 2006) illustrate embedded base connections but do not provide or recommend strength models or design approaches. The only such guidance is available in the AISC *Seismic Design Manual* (AISC, 2018). Figure 4(a) illustrates the assumptions adopted by this approach, referred to hereafter as the AISC SDM Method. Referring to this figure, the applied moment and shear are resisted through the development of bearing stress blocks on both sides of the embedded column flanges. Equation 1 provides a closed-form solution for the moment capacity, obtained by solving for the force and moment equilibrium based on the assumed stress blocks. This equation is based on the work done by Mattock and Gafaar (1982) for steel coupling beams embedded in concrete shear walls:

$$M_{base}^{AISC\ SDM} = 1.54\sqrt{f_c'}\left(\frac{b_w}{b_f}\right)^{0.66}\beta_1 b_f L_e \frac{g}{2}\left(\frac{0.58-0.22\beta_1}{0.88+\frac{g}{2L_e}}\right) \quad (1)$$

where

L_e = embedment depth of the steel column measured from the face of the foundation [as shown in Figure 4(a)]

b_f = width of the embedded section (column) flange, in.

b_w = width of concrete foundation perpendicular to the loading direction (b_w is the thickness of the wall pier in the original equation), in.

f_c' = specified compressive strength of concrete, ksi

$\frac{g}{2}$ = distance from the top surface of the foundation to the inflection point of the column, in.

β_1 = factor relating the depth of the equivalent rectangular stress block to the neutral axis depth, c, as defined in ACI 318-19 (ACI, 2019)

The term $\left(\frac{b_w}{b_f}\right)^{0.66}$ accounts for the effect of concrete confinement and the spread of compressive stress ahead of the column flange, such that the value 0.66 is calibrated to match experimental results by Mattock and Gaafar.

Referring to Figure 4(a), the values c/L_e and k_2 are assumed to be 0.66 and 0.36, respectively, as reported by

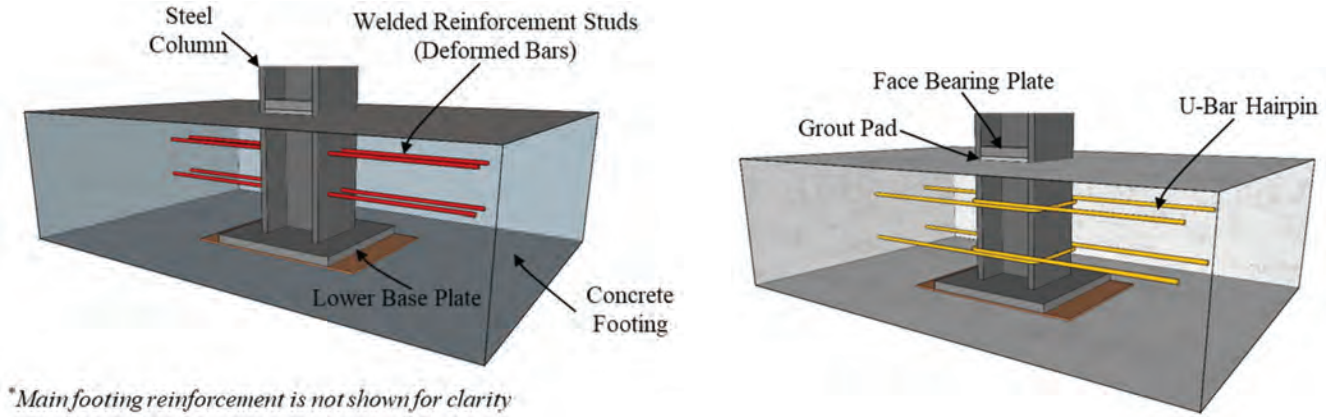

(a) Welded reinforcement stud *(b) U-bar hairpin*

Fig. 3. Details under investigation for the experimental program.

Mattock and Gaafar (1982). From the perspective of ECB connections, the following aspects of this method are problematic: (1) It assumes that the entire moment is carried solely by the bearing against the flanges (i.e., it does not consider the effect of the embedded base plate and its contribution to moment resistance); (2) the term reflecting the effect of concrete confinement is unbounded, which has the potential of overestimating the bearing stresses in concrete foundations, because footings are often significantly wider than the embedded steel section as compared to shear walls; and (3) several factors relating to the mechanics of the method (e.g., the ratio of the neutral axis location to the depth of embedment, c/L_e, and consequently the value k_2) have been particularized for simplification based on geometrical aspects and constraints that are not necessarily analogous for the case of ECB connections [see Figure 4(a)].

Grilli and Kanvinde (2017) developed a strength model that presumes that the total applied base moment is resisted by two mechanisms [see Figure 4(b)]: (1) horizontal bearing stresses against the column flange—assumed to be rectangular/constant in nature, accompanied by the formation of a shear panel action, and (2) vertical bearing stresses against the base plate that resist its rotation. The distribution of moments between these two mechanisms is determined through a semi-empirical equation that is inspired by the analytical solution to a beams-on-elastic foundations problems (Hetenyi, 1946), wherein the column is assumed to be a beam embedded in the elastic foundation. The details of these derivations are provided in Grilli and Kanvinde (2017); however, the equations are not as succinct as for the SDM approach.

Neither model accounts for the reinforcement attached to the column flanges (commonly used in practice), neither by ignoring its contribution (the AISC SDM model where the reinforcement is only prescribed for force transfer) nor by not accounting for its presence in the mechanical model through the equilibrium equations (as per Grilli and Kanvinde, 2017). This is problematic because the presence of additional reinforcement greatly influences the failure modes and the strength and stiffness of the connection. The next section presents an experimental program featuring ECB connections with reinforcement attachments. The results from the tested specimens are then compared with the available strength models presented previously to support the development of an approach that overcomes the limitations of these existing models.

EXPERIMENTAL PROGRAM

Figure 5 illustrates the test setup, and Figure 6 illustrates the specimen detailing. Table 1 summarizes the test matrix along with key experimental results.

Test Setup

Figure 5 shows the test setup, including the specimen. Specific aspects of the test setup and specimens are outlined in the following:

1. All specimens featured wide-flange cantilever columns. The height of load application (9.5 ft above the surface of concrete) was assumed to be the inflection point in a first-story column. The columns were all ASTM A992/A992M Grade 50 and were designed to remain elastic throughout the test.
2. Axial compression was introduced through a cross-beam assembly with two hydraulic jacks (shown in Figure 5) connected to tension rods and a freely rotating clevis. The axial forces did not introduce P-Δ moments.
3. The columns were placed on a plywood sheet with 1 in. thickness and the same plan dimensions of the lower base plate to reflect a supporting condition similar to a

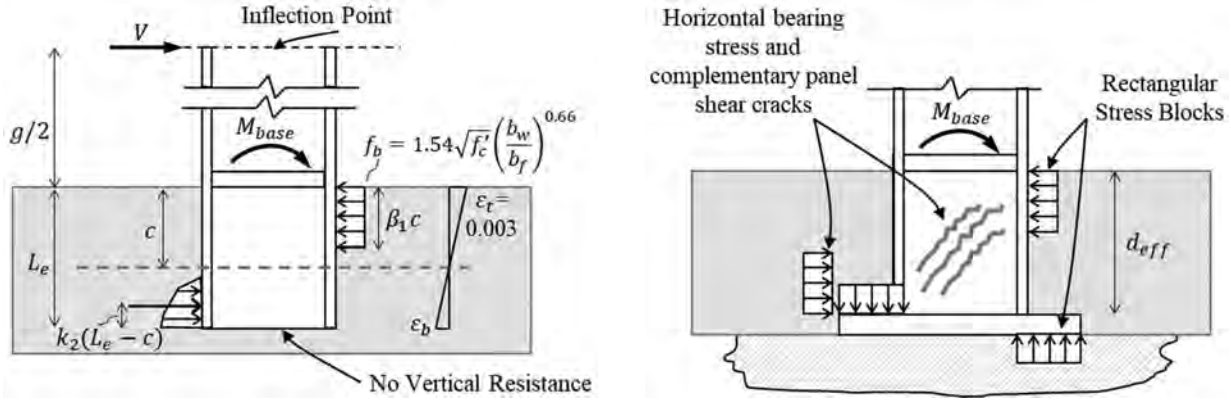

(a) AISC Seismic Design Manual *approach* *(b) Grilli and Kanvinde (2017) model*

Fig. 4. Strength model assumptions.

thin unreinforced slab for erection purposes, rather than directly bearing on bare soil.

4. Face-bearing plates similar to stiffeners were provided at the top of the embedment region (see Figure 6), consistent with the design practice. These provide a load path for compressive forces rather than transferring it through the bottom base plate, which often rests in an unreinforced slab.
5. The pedestals were fastened to the laboratory floor with pretensioned threaded anchors at a distance of 4.5 ft from the column to minimize boundary effects on the stress distribution and failure modes in the vicinity of the column.

Test Matrix

Referring to Table 1, the following test parameters were varied: (1) the configuration of the attached reinforcement—deformed bar anchor versus U-hairpin, (2) the cross-sectional area of the horizontal reinforcement, (3) the column size, and (4) the addition of supplemental vertical reinforcement (stirrups) through the length of the concrete pedestal. Parametric values of the test matrix were selected to reflect similarity with construction practice within the limitations of the test setup; specifically:

1. The column sections were selected to ensure failure in the connection rather than in the column. Thus, the columns are larger relative to the embedment depths in comparison to actual design cases in which the base would typically be stronger than the column.
2. Compressive axial loads were selected to be 10–20% of the axial yield capacity of a hypothetical column that would have an embedment depth similar to the ones used in the study; for more in-depth discussion of this, see Grilli et al. (2017).
3. The footing was similar to the specimens tested by Grilli et al. (2017) in terms of concrete dimensions and nominal reinforcement. All footings were provided with minimal longitudinal and transverse reinforcement. The column embedment depth, d_{embed}, footing dimensions, and footing reinforcement are illustrated in Figure 6.

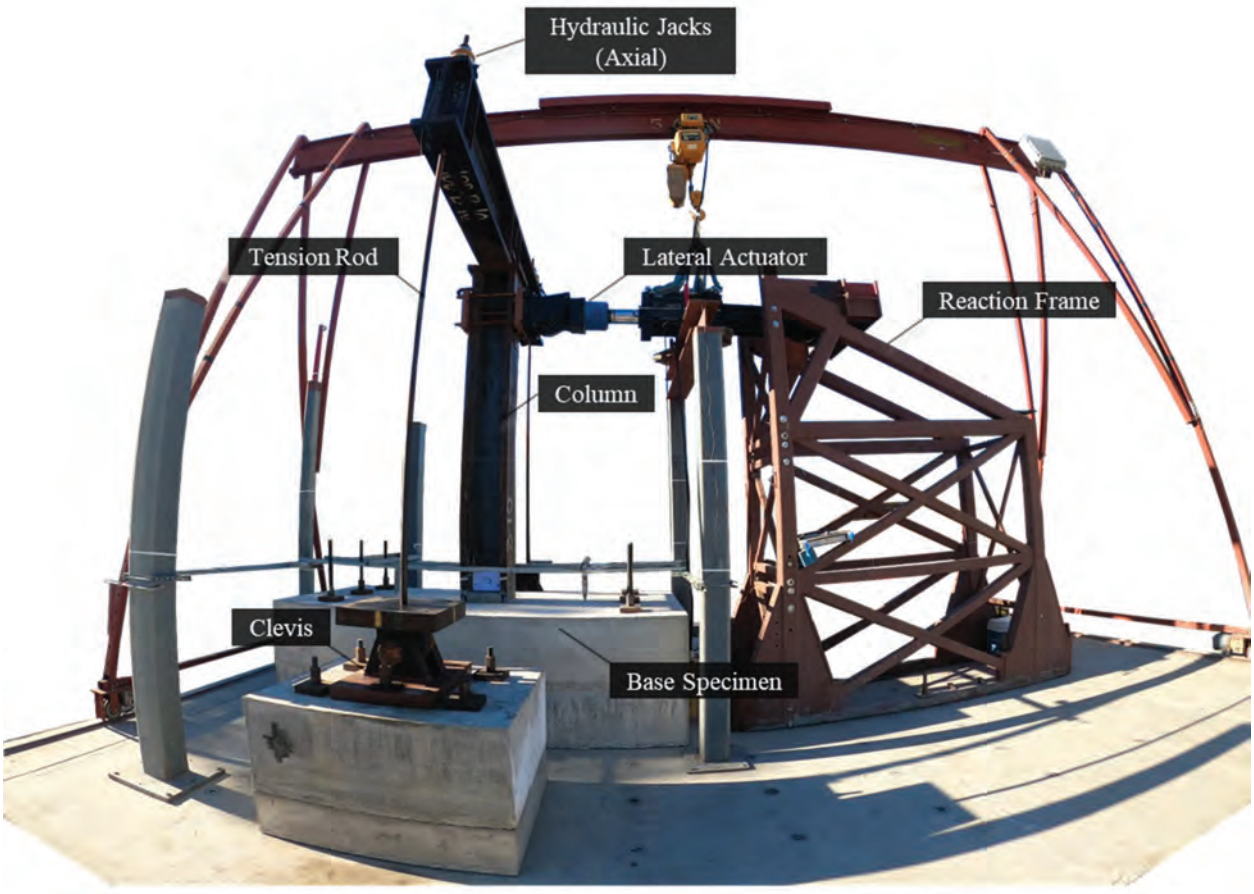

Fig. 5. Wide-angle view of test setup.

This is illustrated for the U-bar hairpin details; however, similar detailing and dimensions are used for the welded reinforcement detail (Test #1) previously shown in Figure 3(a).

4. Referring to Figure 6 and Table 1, reinforcement attachments details were installed in all specimens. All tests featured two rows of attached reinforcement bars (close to the face of the concrete footing). The attached reinforcement was fully developed in tension by providing an adequate tension development length as per ACI 318-19 (ACI, 2019). The location of the attached reinforcement was selected in accordance with the AISC *Seismic Provisions* and AISC *Seismic Design Manual* (AISC, 2016, 2018) such that (a) the first region (top row) of the attached reinforcement coincided with the

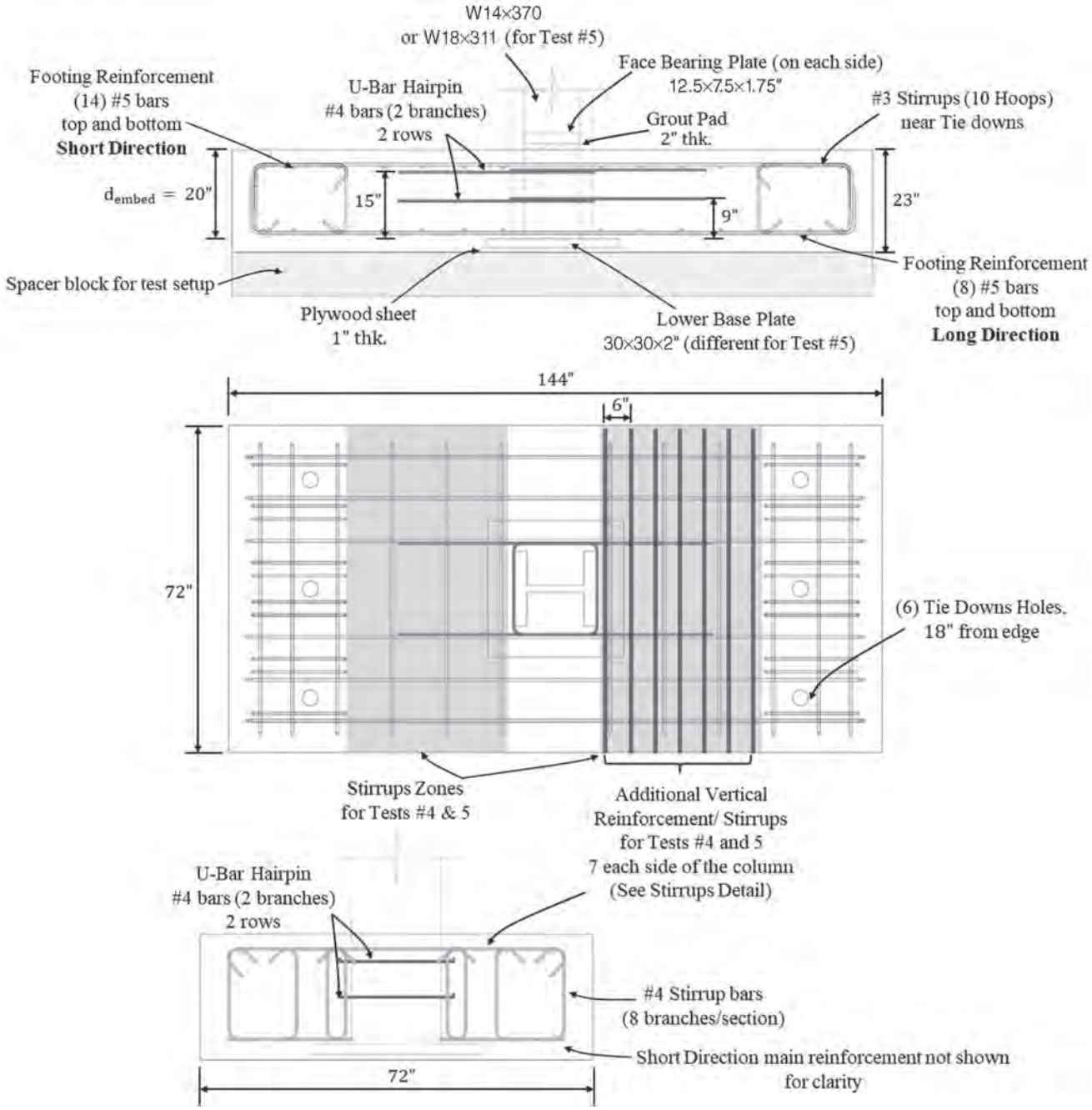

Fig. 6. Specimen detailing (see Table 1 for different parameters across the tests).

longitudinal footing reinforcing bars closest to the face of the foundation, and (b) the second region (bottom row) is placed at a distance no less than $d_{col}/2$ from the termination of the embedded length.

5. Test 1 included #4 (½-in.-diameter) weldable rebars (ASTM A706 Grade 60), arc welded directly to the flange [see Figure 3(a)], whereas Test 2 featured #4 (½-in.-diameter) U-bar hairpin reinforcement (ASTM A615 Grade 60) wrapped around the column embedment (alternating in each row to engage the flanges in both loading directions). Test 3 featured bundled U-bar hairpins with a total of 4 #6 U-bar hairpins per row (¾ in. diameter). For Tests 4 and 5, supplemental vertical reinforcement/stirrups (shown in Figure 6) were installed to assess the effect on connection strength and failure modes.
6. Subsets of tests may be considered to isolate the effect of test variables. For example, Tests 1 and 2 provide a direct examination of the effect of different attachment techniques (i.e., arc welding versus anchoring/fixing), whereas Tests 2 and 3 provide an investigation of the effect of reinforcement area/size. In addition, Tests 2 and 4 allow the investigation of the effect of vertical stirrups, whereas Tests 4 and 5 directly examine the effect of column width/size. The specimens from this program also allow for direct comparison with tests from the experimental program by Grilli et al. (2017), which featured otherwise similar column sizes and footing dimensions.

Standard cylinder tests were performed for all concrete pours as well as grout for all specimens. Coupon tests from the attached reinforcement (both welded studs and U-bar hairpins) used in the experiments were also conducted. Table 2 summarizes the results of ancillary tests for measured material properties that are used to interpret results.

Loading Protocol

For all test specimens, the axial compression was introduced and held constant while the lateral deformation history (expressed in terms of column drift ratio) was applied as per the ATC-SAC protocol (Krawinkler et al., 2000). This protocol was applied until 6% drift amplitude was reached except for Tests 1 and 2, which were stopped at 5% drift.

EXPERIMENTAL RESULTS

Figures 7(a)–7(e) show the moment-drift response of all the five specimens. Figures 8(a)–8(c) show photographs of damage progression and failure modes for the tested specimens, whereas Table 1 shows key results. A qualitative assessment of experimental response for the tested specimens is now presented, to facilitate the interpretation of quantitative data, which is presented subsequently. In the following discussion, the terms "ahead of the column" and "behind the column" denote the compression side of the connection (i.e., in the direction of applied load) and the tension side of the connection, respectively.

Qualitative Discussion of Failure Modes

Referring to Figures 8(a)–8(c), all specimens followed a qualitatively similar damage progression, with some variations resulting from reinforcement detailing. During the initial stages of loading (applied drift less than 1%), minor cracks initiated at the corners of the column as shown in Figure 8(a). Following this, diagonal shear cracks formed on the sides of the block, accompanied by a vertical crack in the concrete behind the column flange, where the attached reinforcement produces tension. These cracks grew in width as loading progressed, with spalling of the concrete ahead of the column flanges. These vertical cracks behind the column reduce the uplift capacity of the base plate, as discussed later. As the applied drift increased, the diagonal shear cracks on the sides of the concrete block grew in width indicating the development of a shear panel. However, this did not control failure or the peak load. The final failure mode, which controlled connection strength, varied from one specimen to another, depending on the vertical reinforcement (or its absence). One of two scenarios occurred [shown photographically in Figures 8(b)–8(c)], these are:

1. In Tests 1, 2, and 3 (without the additional vertical reinforcement), final failure was accompanied by vertical breakout on the tension side of the connection. This failure mechanism is similar to anchor pryout failure modes in concrete (Anderson and Meinheit, 2005), which was observed in similar details by Grilli et al. (2017); see Figure 2(b). The pryout failure occurs when the moment resisting the uplift of the base plate reaches a critical value. This results in the formation of a breakout cone, as shown in Figure 8(b).
2. For Tests 4 and 5 (with additional vertical reinforcement as shown in Figure 6), the presence of supplemental reinforcement mitigated the final tension breakout failure. Instead, the failure occurred at the interface of the vertical crack forming behind the column flanges, as shown in Figure 8(c), at a location between installed stirrups. No spreading of failure (i.e., cone formation) was observed for such tests.

In all tests, the peak moment was achieved between 2% to 2.5% drift. After this, strength deterioration was observed [see Figures 7(a)–(e)] as the breakout block of concrete started to separate from the remainder of the footing. A qualitatively similar response—in other words, pinched hysteresis with excellent deformation capacity and minimal

Table 1. Tests Matrix and Key Results

Test[a]	Axial Load P (kips)	Column Size b_f (in.)	Embedment Depth d_{embed} (in.)	Z[b] (in.)	Base Plate $t_p \times N \times B$ (in.)	Attached Reinforcement Grade	Reinforcement Configuration	M_{max+}^{test} (kip-ft)	M_{max-}^{test} (kip-ft)	$\frac{M_{max}^{test}}{M_{max}^{AISC\ SDM}}$[c]	$\frac{M_{max}^{test}}{M_{max}^{Model}}$
1	100	W14×370 (16.5)	20	114	2×30×30	Weldable rebar studs ASTM A706 Grade 60	(4) #4 (½ in. diameter)	994	1002	0.77	0.82
2	100			114		U-bar hairpin ASTM A615 Grade 60		1055	904	0.81	0.88
3	100			114			(8) #6 (¾ in. diameter)	1334	1109	1.03	1.06
									Mean	**0.87**	**0.92**
									CoV	**0.16**	**0.14**
4	100			114	2×30×30	U-bar hairpin ASTM A615 Grade 60	(4) #4 (½ in. diameter) + Vertical reinforcement	1196	908	0.92	0.90
5	100	W18×311 (12)			2×34×28			1220	820	1.05	1.01
									Mean	**0.99**	**0.96**
									CoV	**0.09**	**0.08**
1G	100	W14×370 (16.5)		112	2×30×30	–	–	1902	1927	1.45	1.22
2G	100	W18×311 (12)		112	2×34×28			1714	1599	1.44	1.17
3G	–	W14×370 (16.5)	30	122	2×30×30			2759	2540	0.97	0.91
4G	100			122				3042	2664	1.07	0.99
5G	150 (T)			122				2803	2555	0.99	0.95
									Mean	**1.19**	**1.05**
									CoV	**0.20**	**0.13**
									Mean (All)	**1.05**	**0.99**
									CoV (All)	**0.22**	**0.13**

[a] New tests are labeled from 1–5, whereas tests from Grilli et al. (2017) are labeled 1G–5G.
[b] Moment-to-shear ratio (i.e., distance from point of load application to top of concrete); see Figure 9(c).
[c] M_{max}^{test} is the maximum moment value of both directions of loading (positive and negative).

Table 2. Summary of Measured Material Strengths from Ancillary Tests					
Test	Number of Samples[a]	Yield Strength F_y^{rebar}[b] (ksi)	Ultimate Strength F_u^{rebar} (ksi)	Concrete Compressive Strength f_c'[c] (ksi)	Grout Compressive Strength F_{grout}[c] (ksi)
ASTM A706 Grade 60 reinforcement	2	71.2	94.2	–	–
ASTM A615 Grade 60 reinforcement	2	65.0	102.5	–	–
Concrete cylinders	5	–	–	4.0	–
Grout cylinders	4	–	–	–	8.5

[a] Average values for tested samples are presented.
[b] Measured yield stress for ASTM A706 bars is based on the 0.2% offset method.
[c] Compressive strength for concrete and grout cylinders is measured on the day of full-scale test.

strength degradation (i.e., less than a 20% drop in peak base moments at 4% drift)—was observed for all tests, except for Test 3 (with bundled U-bar hairpins), which showed a drop in load of roughly 40% after achieving capacity at around 3% drift.

Quantitative Analysis of Test Data

Table 1 summarizes key quantities measured in the experiments. Two moment values were recovered for each test corresponding to maximum moment observed in each loading direction. These are denoted as M_{max+}^{test} and M_{max-}^{test}, such that the positive sign denotes the direction of the first

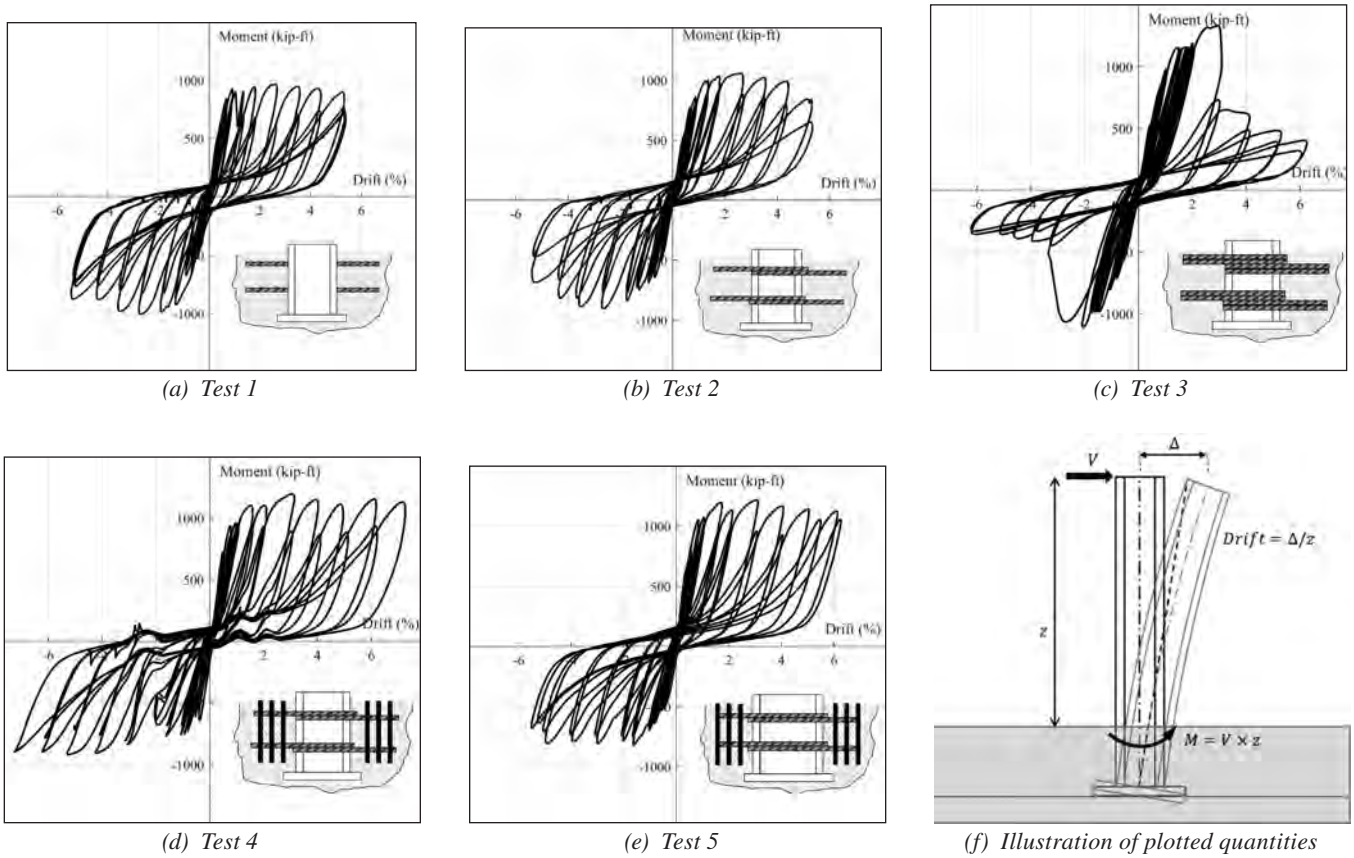

(a) Test 1 (b) Test 2 (c) Test 3

(d) Test 4 (e) Test 5 (f) Illustration of plotted quantities

Fig. 7. Moment-drift plots for all tests and a schematic illustration of plotted quantities.

deformation excursion. Referring to Table 1 and Figures 7 and 8, the following observations may be made:

1. The main observation is that the application of horizontal reinforcement (i.e., attached reinforcement to column flanges) significantly reduced the strength and stiffness relative to values observed by Grilli et al. (2017). Specifically, the specimens from Tests 1 and 2 of the Grilli et al. (2017) test program (Test 1G and 2G in Table 1) are nominally identical to Tests 1 and 5 of this study except for the attachment of horizontal reinforcement. On average, the strengths observed in the specimens with horizontal reinforcement is 45–50% lower than that of their unreinforced counterparts [see Figure 8(d)]. This is counterintuitive and a somewhat disquieting observation. However, a closer evaluation of the underlying mechanisms and failure mode suggests that this may be attributed to the development of a tension field in the concrete behind the column due to the horizontal reinforcement that is in tension. This tension field reduces the resistance of the concrete to uplift of the base plate, significantly reducing overall connection strength.
2. A comparison of results from Tests 1 and 2 (welded rebar stud versus U-bar hairpin) indicates that the moment strength observed in both tests is very close (within 5%), while the load-deformation shows modest difference in terms of cycle-to-cycle degradation.
3. A comparison between Tests 2 and 4 provides a direct assessment of the effect of additional vertical reinforcement/stirrups. The stirrups increase the strength of the connection by 20%. This may be attributed to the fact that the vertical reinforcement mitigates the formation of the tension breakout cone, resulting in higher moment resistance.
4. Comparing Tests 4 and 5 (which are similar in terms of embedment depth, attached reinforcement, and stirrups, but differ in terms of column section and base plate geometry; see Table 1), the strengths are almost identical.

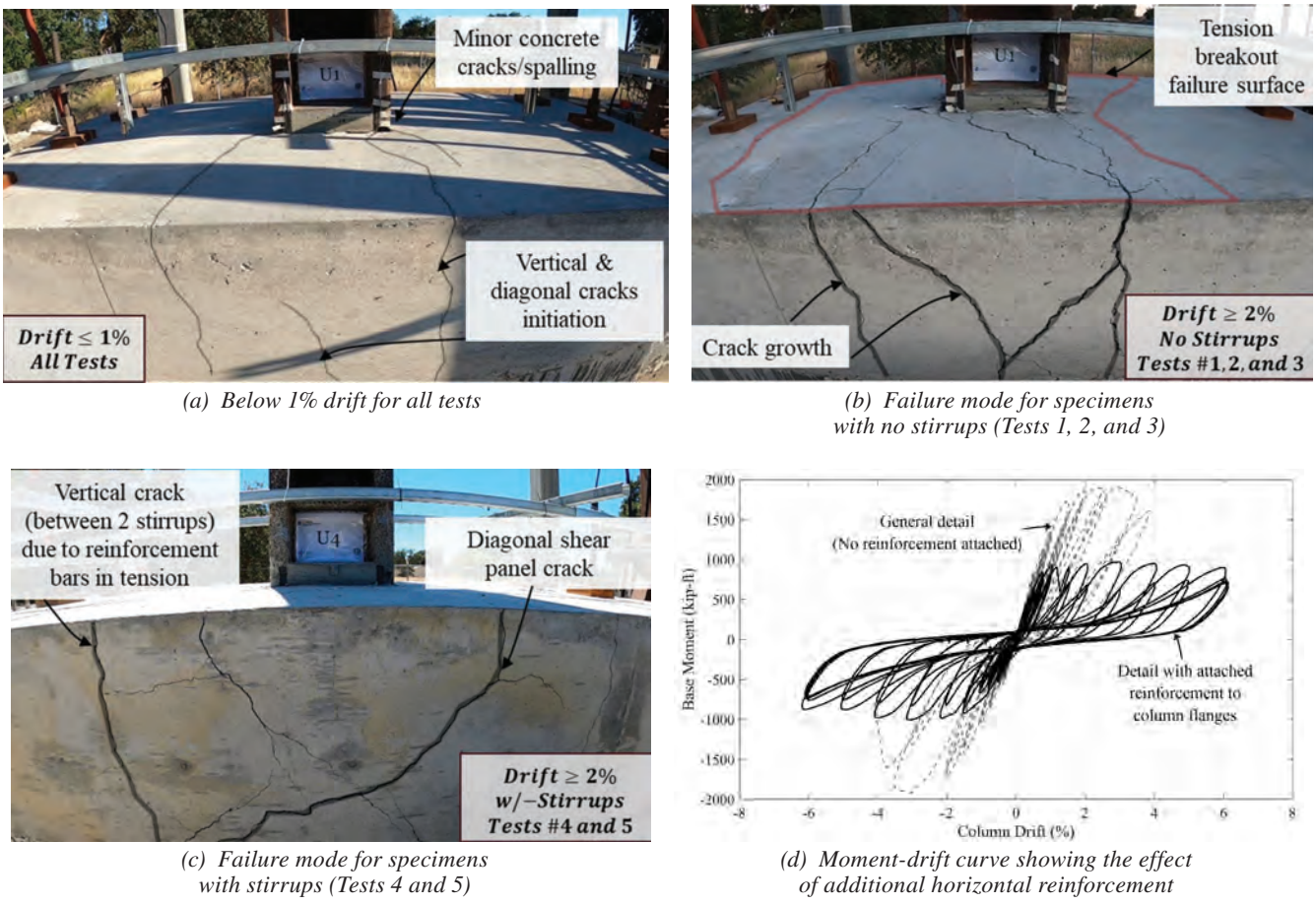

(a) Below 1% drift for all tests

(b) Failure mode for specimens with no stirrups (Tests 1, 2, and 3)

(c) Failure mode for specimens with stirrups (Tests 4 and 5)

(d) Moment-drift curve showing the effect of additional horizontal reinforcement

Fig. 8. Typical damage progression and behavioral insights.

5. The effect of additional attached horizontal reinforcement may be assessed through Tests 2 and 3, which differ only in terms of the cross-sectional area provided by the attached horizontal reinforcement. A 20% increase in moment capacity was observed in Test 3, which has a 340% higher cross-sectional area of reinforcement.

6. All specimens with reinforcement attained very high deformation without significant loss in moment strength (i.e., 6% drift compared to about 3% for the specimens without reinforcement tested by Grilli et al., 2017).

PROPOSED MODEL FOR STRENGTH CHARACTERIZATION

Based on the observations from the experimental program, this section describes the development of a strength model for ECB connections. The model incorporates observations from all relevant test data on embedded connections to quantify internal force transfer mechanisms and failure modes. Specifically, the model considers specimens from this study (with additional horizontal reinforcement), as well as those tested previously by Grilli et al. (2017) without such reinforcement, and provides a unified approach to characterize their strength. The proposed approach assumes that the various internal mechanisms act "in parallel," similar to the development of a plastic mechanism within the connection. This is based on the observation (across all experiments) that significant deformations are mobilized within the various mechanisms (horizontal and vertical bearing, as well as shear panel) such that the strengths from these may be considered additive. Furthermore, this results in a simplified model that also provides fairly accurate results. Figures 9(a)–9(d) schematically illustrate the internal stress distributions and force transfer mechanisms, whereas Figures 9(e)–9(f) illustrate failure modes corresponding to the vertical breakout/pryout limit states. Figure 10 includes a flowchart summarizing the process to determine the ECB connection capacity using the proposed model.

Moment Resistance Due to Horizontal Bearing Stresses

Referring to Figure 9(c), one fraction of the applied moment, M_{HB}, and the entire shear, V, is resisted through the development of bearing stresses on both sides of the embedded column flanges. A modified version of the previously discussed approach developed by Grilli and Kanvinde (2017) is used to estimate the moment resistance provided by the horizontal bearing mechanism while adding the contribution of horizontal reinforcement. The bearing stresses are idealized such that a uniform stress distribution is assumed for both the top stress, f_b^{top}, and the bottom stress, f_b^{bottom}, such that:

$$f_b = f_b^{top} = f_b^{bottom} = 1.54\sqrt{f_c'}\left(\frac{b_w}{b_f}\right)^n \le 1.7f_c' \tag{2}$$

The term b_w/b_f accounts for the effect of confinement, wherein b_w is the width of the foundation, and b_f (in inches) is the width of the flange. The exponent, n, is calibrated based on experimental data to a value of $n = 0.66$ (Mattock and Gaafar, 1982). The value of bearing stress is capped by a value of $1.7f_c'$, reflecting the maximum confinement of the concrete by the reinforcement and the surrounding concrete. Referring to Figure 9(c), the resultant compressive forces C_{top} and C_{bottom} are defined as follows:

$$C_{top} = f_b^{top}\beta_1 c b_j \tag{3}$$

$$C_{bottom} = f_b^{bottom}\beta_1 (d_{embed} - c) b_j \tag{4}$$

In Equations 3 and 4, c (in inches) is the neutral axis depth, $\beta_1 = 0.85$ is the factor relating the depth of the equivalent rectangular stress block to c, and $b_j = (b_f + B)/2$ is the effective width of the joint panel, where B is the width of the lower base plate. Based on work by Grilli and Kanvinde (2017), this expression reflects the development of bearing stresses over a width greater than the column flange because a portion of the concrete panel outside the flange is mobilized. The attached reinforcement is assumed to act in tension and compression in the case of the welded reinforcement bars, and only in tension in the case of the U-bar Hairpin, since the column can transfer force to it only by bearing against the wraparound segment of the U-bar. The reinforcement bars are assumed to be elastic-perfectly-plastic and fully developed in tension (as per ACI 318-19), $F_{rebar} = A_{rebar} \times F_y$. The resultant from each rebar row is directly added to the resultants from the stress distributions, and the moment resistance due to horizontal stresses, M_{HB}, may be obtained by summation of the resultant moments at the top of foundation level, such that:

$$V - C_{top} + C_{bottom} - F_{rebar}^{top} + F_{rebar}^{bottom} = 0 \tag{5}$$

$$M_{HB} = -C_{top}\frac{\beta_1 c}{2} + C_{bottom}\left[d_{embed} - \frac{\beta_1 (d_{embed} - c)}{2}\right] - F_{rebar}^{top} d_{rebar}^{top} + F_{rebar}^{bottom} d_{rebar}^{bottom} \tag{6}$$

In Equations 5 and 6, F_{rebar}^{top} and F_{rebar}^{bottom} are the resultant forces from the engaged reinforcement rods, and d_{rebar}^{top} and d_{rebar}^{bottom} are the distances from the rebar location to the top of the foundation surface for the top and bottom rebar, respectively. Eliminating the term c, which is common to both Equations 5 and Equation 6 (through the resultant force terms C_{top} and C_{bottom}), results in one expression relating the moment capacity due to horizontal bearing directly to the shear force:

$$M_{HB} = \frac{(F_{rebar}^{top} - F_{rebar}^{bottom} - V)d_{embed}}{2} - \frac{(F_{rebar}^{bottom} - F_{rebar}^{top} + V)^2}{4b_j f_b} - \frac{\beta_1 b_j d_{embed}^2 f_b(\beta_1 - 2)}{4} - F_{rebar}^{top} d_{rebar}^{top} + F_{rebar}^{bottom} d_{rebar}^{bottom} \quad (7)$$

Equation 7 represents an interaction equation between the shear force, V, and the moment, M_{HB}, such that for any given shear force V, the maximum moment may be determined using it. The equation assumes that the "neutral axis"—the transition in bearing stress direction—occurs between the upper and lower layers of horizontal reinforcement. Further, it is noted that the moment determined in this manner is calculated at the elevation corresponding to the top of the footing.

Moment Resistance Due to Vertical Bearing Stresses

Referring to Figure 9(d), the base plate at the bottom of the embedment is subjected to bearing stresses on the lower and upper surfaces, resisting the moment transferred to the base through the column flanges, as well as the net axial force transferred to the base plate. The base plate is assumed to resist the total axial force (through upward bearing in the case of compressive load or downward bearing in the case of tensile load) in addition to the moment resisted through the vertical bearing mechanism, M_{VB}. Observations from experiments suggest that although the face-bearing plate at the top of the foundation transfers axial compression into the footing, the separation between the column and the footing during lateral loading [see Figures 8(b)–8(c)] implies that a significant portion of this axial load is carried through the

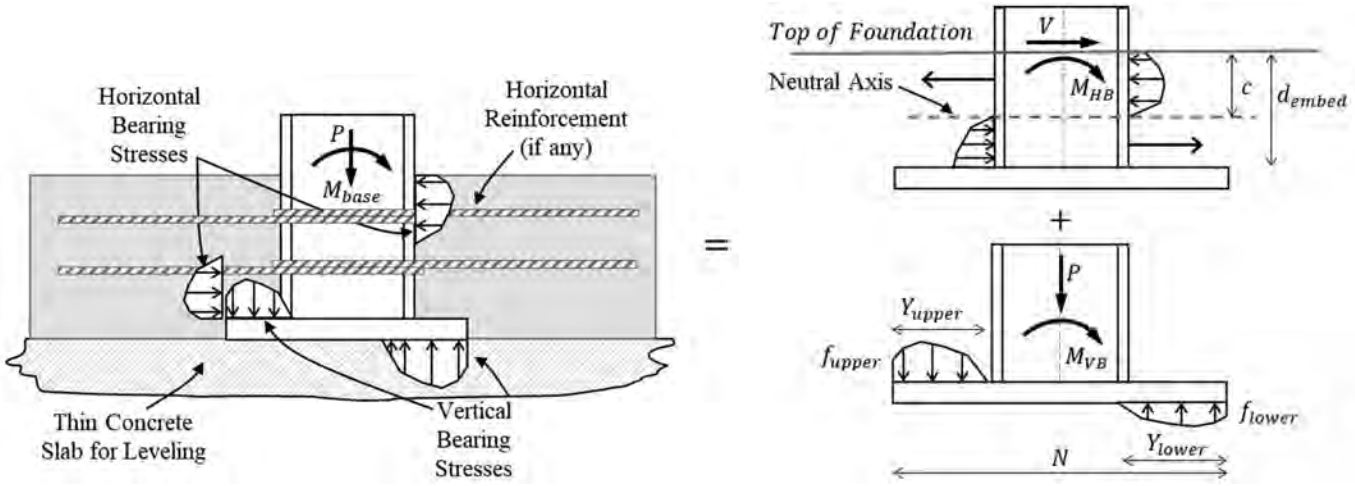

(a) Overall mechanism

(b) Moment resisted due to horizontal and vertical forces

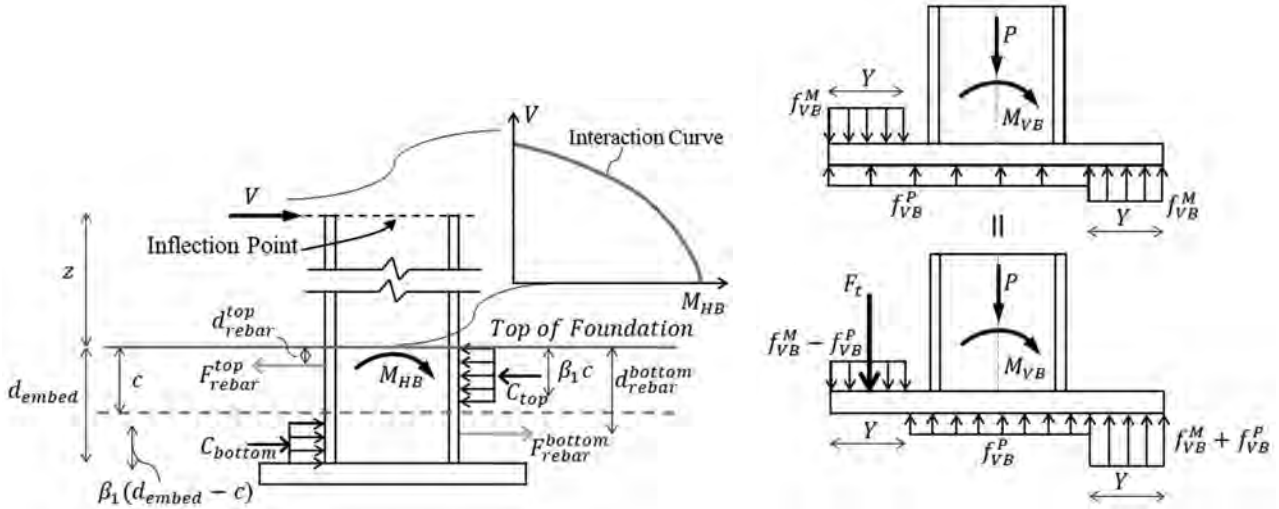

(c) Horizontal resistance mechanism

(d) Idealized vertical resistance mechanism

Fig. 9(a–d). Proposed model for strength characterization.

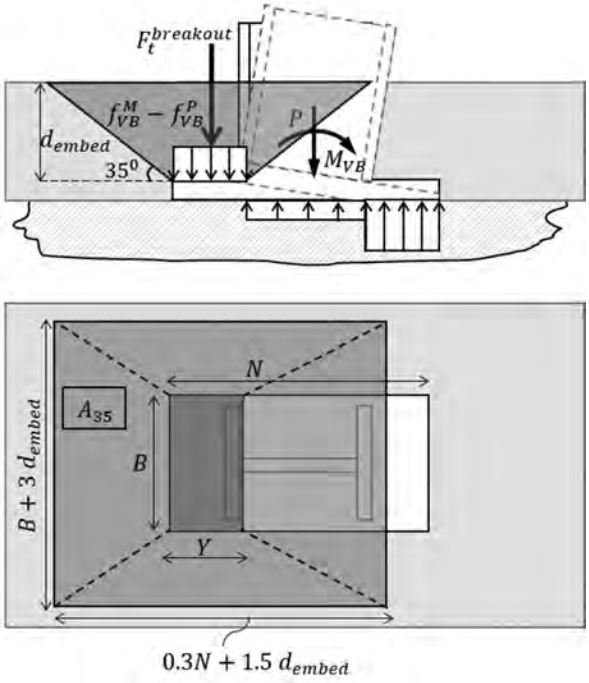

(e) Tension breakout failure mode (vertical bearing)

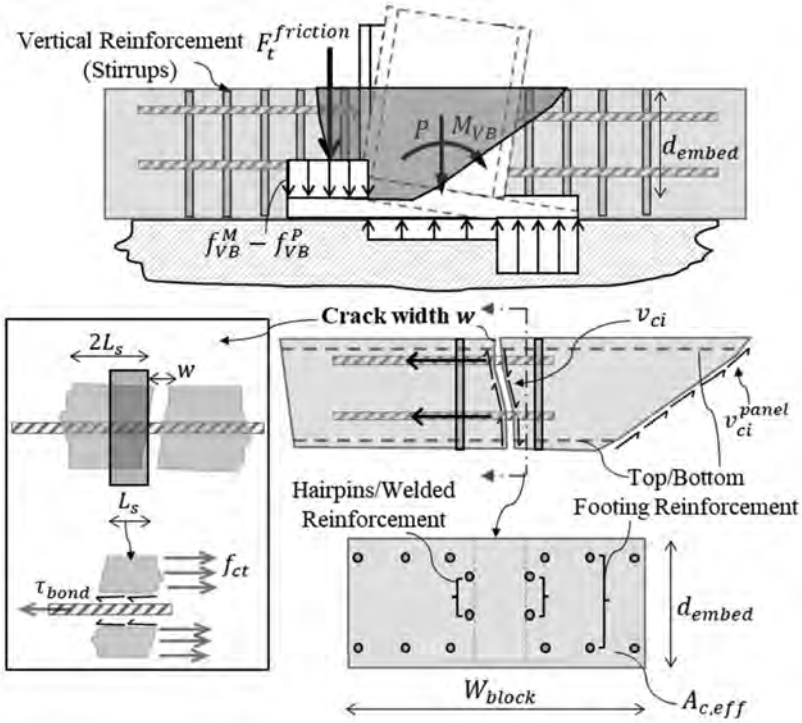

(f) Shear/friction failure mode (vertical bearing)

Fig. 9(e–f). Proposed model for strength characterization.

footing to the base plate at the bottom. The stress distribution on the base plate itself arises from a superposition of stresses due to axial forces and the moment, M_{VB} (Grilli and Kanvinde, 2017), and idealized these stresses as a stepped distribution [see Figure 9(d)], to reflect the combination of axial force and bending resisted by them. The width, Y, of the two "outside" steps was $0.3N$, whereas the middle step was $0.4N$ wide. This results in a stress distribution with values determined using Equations 8 and 9. Specifically, the stresses on the tension side, $f_{VB}^{M} - f_{VB}^{P}$, on the compression side step, $f_{VB}^{M} + f_{VB}^{P}$, and on the central portion may be related to the applied loading as follows:

$$f_{VB}^{M} = \frac{M_{VB}}{(N-Y)\times Y \times B} \tag{8}$$

$$f_{VB}^{P} = P/(B\times N) \tag{9}$$

Under these stresses, critical failure mode in the lab specimens was observed to be the breakout/pryout of the concrete on the tension side of the connection. This assumes that the supporting material slab below the base plate can develop the bearing stresses, $f_{VB}^{M} + f_{VB}^{P}$, induced on the compression side without failure. Implications of disregarding vertical bearing failure on the compression side of the connection are discussed later. With this assumption, determination of the moment, M_{VB}, requires estimation of the force, F_t, that results in a breakout/pryout type failure of the concrete above the base plate on the tension side:

$$F_t = \left(f_{VB}^{M} - f_{VB}^{P}\right)(Y\times B) \tag{10}$$

Following the idealization of Grilli and Kanvinde (2017), this force is assumed to act at a location of $Y/2$ (i.e., $0.3N/2$) from the edge [i.e., at the center of the outside step as shown in Figure 9(d)]. Utilizing the stress distributions in Equations 8–10, the following relationship may be obtained between the moment M_{VB} and the force F_t.

$$M_{VB} = \left(F_t - \frac{PY}{N}\right)(N-Y) \tag{11}$$

The magnitude of F_t may be estimated based on the failure mode, which in turn depends on the connection detailing. Based on the experimental results, three possible scenarios are now discussed.

Scenario 1: Breakout of concrete failure cone in the absence of attached horizontal reinforcement

This failure mode is applicable only when no horizontal reinforcement is attached (tests by Grilli et al., 2017); that is, the tension field produced by the reinforcement does not affect the development of such a cone. In such a case, as shown in Figure 9(e), the total breakout force may be calculated as:

$$F_t = F_t^{breakout} = \frac{40}{9}\frac{1}{\sqrt{d_{cover}}}\sqrt{f_c'}A_{35} \tag{12}$$

Equation 12 is based on the concrete capacity design (CCD) method proposed by Fuchs et al. (1995), such that d_{cover} is the thickness of the material that must be ruptured for breakout, which is equal to d_{embed} for tension breakout. The term A_{35} is the projected area of a 35° failure cone emanating from the edges of the stress block on the tension side of width $0.3N$. The projected area A_{35} is shown in Figure 9(e) and is calculated using Equation 13:

$$A_{35} = (B + 3\ d_{embed})(0.3\ N + 1.5\ d_{embed}) - (B\times 0.3N) \tag{13}$$

Once established this way, the moment resisted through vertical bearing may be determined by using Equations 11–13.

Scenario 2: Breakout of concrete failure cone in the presence of attached horizontal reinforcement

As previously discussed, once reinforcement is attached to the column flanges, a tension field is created above the uplifting end of the base plate, reducing the resistance to vertical motion. Experimental data (from Tests 1–3 of this study) suggests that this resistance is negligible, such that the moment due to vertical bearing resistance may be conservatively assumed as zero (i.e., $M_{VB} = 0$).

Scenario 3: Shear failure of concrete in the presence of horizontal reinforcement and vertical stirrups

The third scenario is associated with the presence of vertical reinforcement/stirrups supplementary to the attached horizontal reinforcement. The intent of the stirrups is to increase the vertical bearing resistance by mitigating the breakout failure mode noted in Scenario 2. Referring to the test results and Figures 7(d)–7(e), the stirrups added a fair amount of vertical resistance while shifting the failure mode from a cone breakout into a direct shear failure at the weak point in the foundation [i.e., the cracked section between two stirrups as shown in Figure 8(c)]. For this, F_t may be estimated from the free-body diagram of the breakout block shown in Figure 9(f). This requires the determination of the shear stress on the crack interface. Cracks occurring along the interface between the cement paste and the aggregate particles result in a rough surface that can transfer shear through aggregate interlocking, as shown in Figure 9(f). Vecchio and Collins (1986) developed a relationship between the shear stress transferred across the crack, v_{ci}, the crack width, w, and the compressive stress, f_{ci} (in psi), on the crack, such that:

$$v_{ci} = 0.18\ v_{ci,max} + 1.64\ f_{ci} - 0.82\ \frac{f_{ci}}{v_{ci,max}} \tag{14}$$

where $v_{ci,max}$ (in psi) is the maximum shear stress that can be transferred across a crack when its width is w (in inches), given by:

$$v_{ci,max} = \frac{2.16\sqrt{f_c'}}{0.3+\left(\frac{24w}{a+0.63}\right)} \quad (15)$$

In Equation 15, a (in inches) is the diameter of the coarse aggregate in the cracked concrete, taken as 0.75 in. Given that the crack, as shown in Figure 9(f), is subjected to tension, f_{ci} in Equation 14 is zero, and thus:

$$v_{ci} = 0.18\, v_{ci,max} \quad (16)$$

The diagonal crack is assumed to have zero shear strength [v_{ci}^{panel} in Figure 9(f) at the right-hand side of the breakout block] because it has already opened completely due to shear panel action by the time the connection capacity is attained. The crack width, w, is determined from the bond-slip relationship at the reinforced concrete interface using the CEB-FIP Model Code (FIB, 1990). Using this approach, the crack width is:

$$w = 2\,L_s\,(\varepsilon_{sm} - \varepsilon_{cm}) \quad (17)$$

where $2L_s$ is the maximum slip length and ε_{sm} and ε_{cm} are the average value of steel and concrete strains, respectively. The transfer length, L_s, is defined as:

$$L_s = \frac{f_{ct}A_{c,eff}}{\tau_{bond}\sum\pi d_i} \quad (18)$$

where f_{ct} is the tensile strength of concrete (taken as $7.5\sqrt{f_c'}$ following the ACI 318-19 provisions); $A_{c,eff}$ (in square inches) is the effective area of concrete $W_{block} \times d_{embed}$ [see

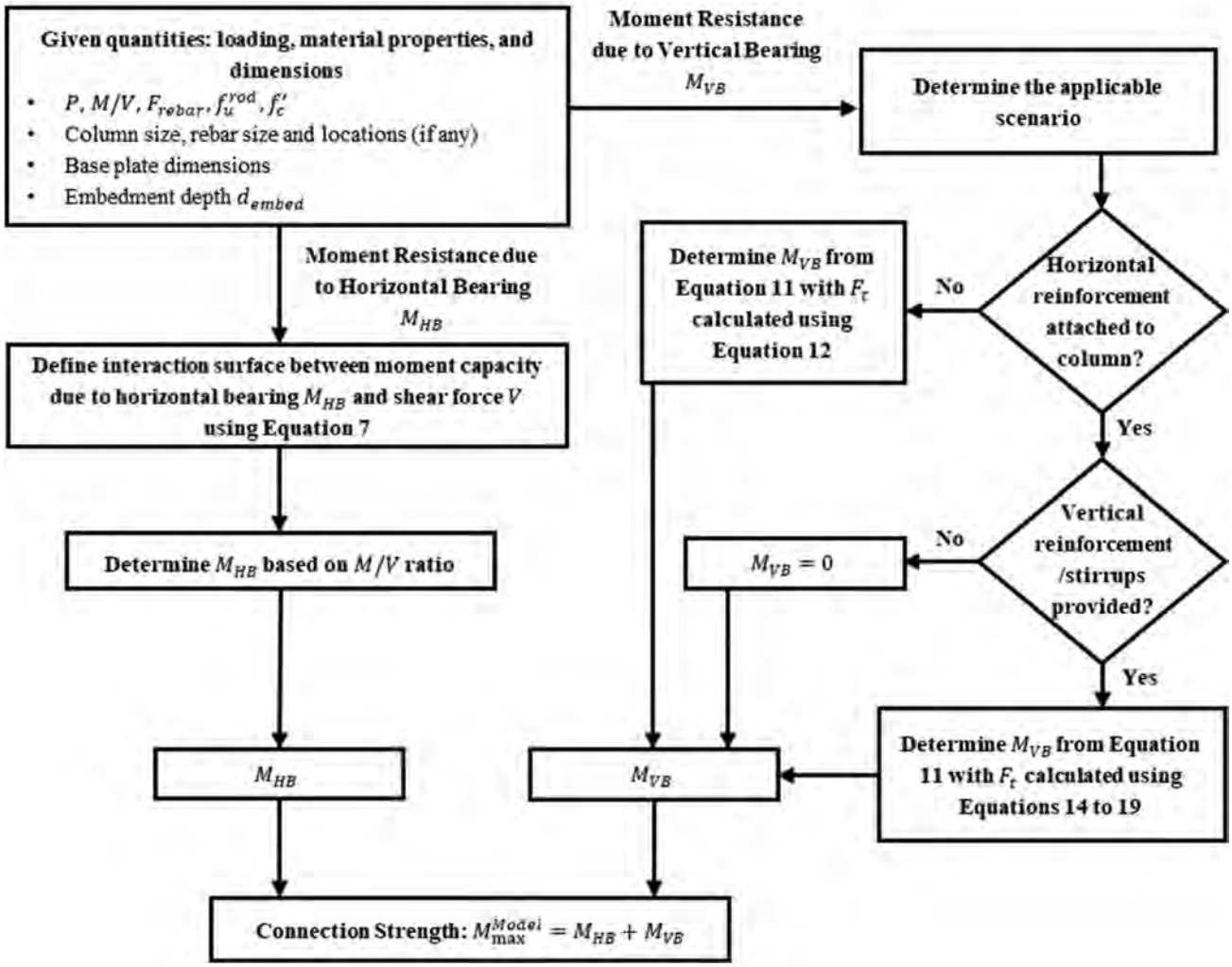

Fig. 10. Flowchart illustrating the strength characterization process.

Figure 9(f)] such that W_{block} is the width of the concrete foundation block; τ_{bond} (in ksi) is the average bond strength along the transfer length, taken as $0.95\sqrt{f_c'}$ (ksi) based on canonical literature (FIB, 1990); and d_i represents the diameters of bars crossing the considered crack. This includes the foundation main longitudinal reinforcement bars, shown in Figure 6, as well as the attached reinforcement, as shown in Figure 9(f). Once determined in this manner, the value of the upward force due to shear friction/aggregate interlocking across the cracked section may be calculated as:

$$F_t = F_t^{friction} = (v_{ci})(A_{c,eff}) \tag{19}$$

This value may then be substituted into Equation 11 to calculate the vertical moment capacity for the connection where vertical/stirrups reinforcement are provided. Once M_{VB} has been determined using the appropriate scenario, the connection strength may be estimated using the proposed unified model as:

$$M_{max}^{Model} = M_{HB} + M_{VB} \tag{20}$$

It is noted here that the moment determined in this manner reflects the moment at the elevation corresponding to the top level of the foundation, considering the statics used in determining M_{HB}. Because the determination of M_{VB} does not include any horizontal forces, it may be statically transferred from the bottom to the top of foundation.

RESULTS AND DISCUSSION

Table 1 summarizes the test-to-predicted ratios for the strength estimates $M_{max}^{test}/M_{max}^{Model}$ for all test data points using the methodology prescribed in the previous section. Also included in Table 1 are the test-to-predicted ratios for the connection strength calculated as per the AISC SDM model $M_{max}^{test}/M_{max}^{AISC\ SDM}$, which is the only model for which official design guidance exists. Figures 11(a) and 11(b) plot the test-to-predicted ratios from both models against the column embedment depth (normalized by the depth of the column, i.e., d_{embed}/d_{col}). Similar comparisons of test data to other models, including the variants of the Grilli and Kanvinde (2017) model are presented in Hassan et al. (2022). Referring to Table 1 and Figure 11, it is observed that:

- The average test-to-predicted ratio for the AISC SDM approach is 1.05 with a coefficient of variation (CoV) of 0.22, indicating that the method is conservative when considered across all the test data (although with large scatter). However, a closer inspection of the data indicates that the method is conservative for the generic details—that is, the Grilli and Kanvinde (2017) tests without horizontal reinforcement—because it does not incorporate the effect of vertical bearing (average test-predicted ratio = 1.19). However, where vertical bearing is insignificant (i.e., tests from the current study without stirrups), the results are somewhat less conservative (average test-predicted ratio = 0.87), while for the cases with the stirrups, the method is fairly accurate, even if it does not consider the contribution from vertical bearing. This may be attributed to the empiricism of calibrated factors in the method, specifically unbounded confinement effect and the simplifications implicitly applied in the method based on the aforementioned discussion. There does not appear to be a significant trend in these results with respect to the embedment depth d_{embed}/d_{col}.
- The proposed model predicts the experimentally observed moment strengths with reasonable accuracy. On average, the test-to-predicted ratio $M_{max}^{test}/M_{max}^{Model}$ = 0.99 with a CoV = 0.13 across all the test specimens, indicating significantly improved performance over the SDM approach. Additionally, the method represents the effects associated with each of the three scenarios outlined previously. Specifically, the approach results in the following average test-to-predicted ratios: (1) Scenario 1—breakout of concrete failure cone in the absence of attached horizontal reinforcement—that is, for the Tests 1G–5G, the average $M_{max}^{test}/M_{max}^{Model}$ = 1.05, with a CoV of 0.13; (2) Scenario 2—breakout of concrete failure cone in the presence of attached horizontal reinforcement—that is, for the Tests 1–3, the average $M_{max}^{test}/M_{max}^{Model}$ = 0.92, with a CoV of 0.14; and (3) Scenario 3—shear failure of concrete in the presence of horizontal reinforcement and vertical stirrups—that is, for the Tests 4 and 5, the average $M_{max}^{test}/M_{max}^{Model}$ = 0.96, with a CoV of 0.08. Thus, the proposed method appears to provide excellent estimates of test response over the subsets of tests (corresponding to each scenario), indicating that it represents the physics and internal stress distributions. Moreover, there is no significant trend in this accuracy with respect to any of the test variables, including the embedment depth, d_{embed}/d_{col} as illustrated in Figure 11(b).

As per the proposed model, the connection strength, M_{max}^{Model}, is attained after significant inelastic deformation and damage have occurred. As a result, this may not be suitable for the design of the base connection (especially if a strong-base–weak-column design is followed as per current practice). A fraction of the ultimate strength could be used for design purposes. This fraction may be taken between

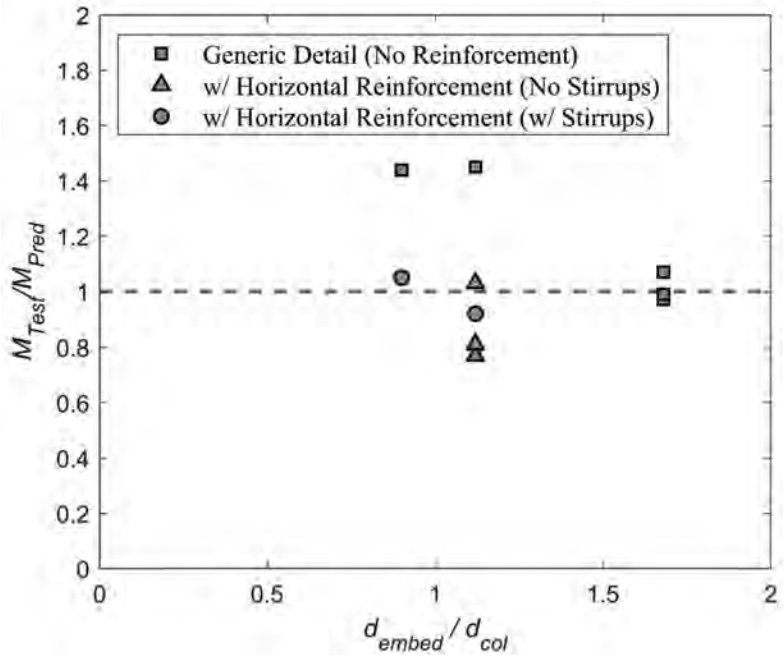

(a) AISC Seismic Design Manual *method*

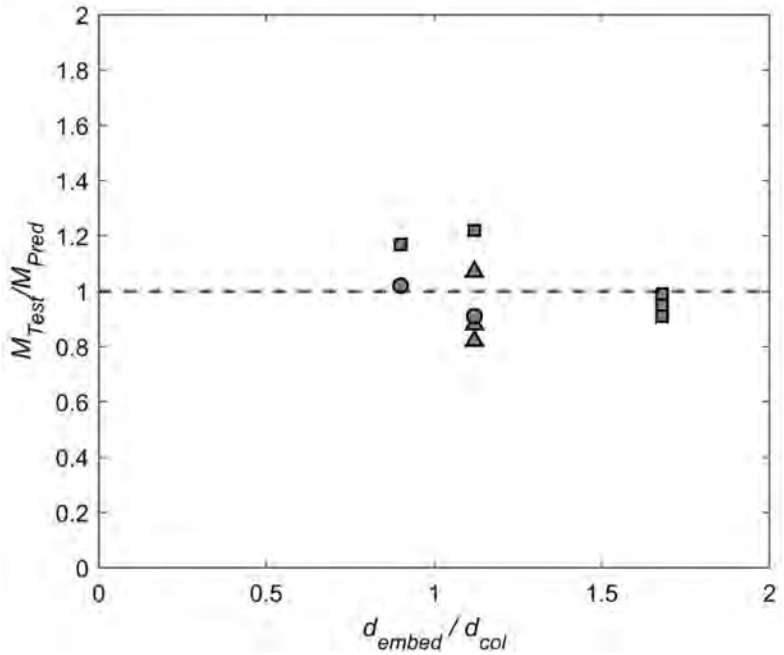

(b) Proposed model

Fig. 11. Test-predicted ratios for all experiments from AISC SDM method and the proposed model plotted against d_{embed}/d_{col}.

0.7–0.8, which represents the ratio between the yield and ultimate moment as observed in tested specimens in this program as well as in Grilli et al. (2017).

SUMMARY AND CONCLUSIONS

Embedded column base (ECB) connections are widely used in mid- to high-rise steel moment frames to resist base moments. Despite their prevalence, methods available to design and estimate their strength rely on approaches originally developed for components such as steel coupling beams embedded in concrete shear walls or composite beam column connections that are similar to ECB connections. While similar in some aspects, these components have significant differences from ECB connections that limit their applicability and accuracy. This study presents findings from five tests representative of ECB connections in the United States. These connections include horizontal reinforcement attached to the column flanges and complement previous experiments (conducted by Grilli et al., 2017) that did not include such reinforcement. Two techniques of attaching the reinforcement were examined, including reinforcement bars welded directly to the column flange or U-bar hairpins wrapped around the column. The tests from this study were considered collectively in developing behavioral insights, evaluating the existing strength characterization approaches, and proposing a new one.

The main observation was that while the attachment of horizontal reinforcement increases moment strength due to the development of horizontal forces, it produces a tension field behind the column. This reduces the restraint the concrete provides to base plate uplift, in turn decreasing moment strength due to vertical bearing stresses. For the specimens tested in this study, the decrease in moment strength (due to vertical stresses) is greater than the increase in moment strength (due to the horizontal stresses), such that the net effect is detrimental. Introduction of vertical reinforcement in the form of stirrups mitigates this problem to an extent by changing the failure mode to shear-friction along a nearly vertical plane rather than concrete breakout. On the other hand, the attachment of horizontal reinforcement significantly increases the rotational ductility of the connections (in the range of 0.06 rad) with respect to details without such reinforcement (in the range of 0.035 rad). These factors may influence detail selection in different contexts—for example, seismic versus nonseismic.

A strength model is proposed to represent these various failure mechanisms. For the horizontal bearing mechanism, the model relies on a stress-block based approach similar to that outlined by Grilli and Kanvinde (2017). For the vertical bearing mechanism, the model considers three scenarios for concrete breakout on the tension side of the connection, depending on the type of reinforcement used, and appears to provide uniformly accurate strength predictions across the different tested configurations and test programs. These predictions are superior compared to the current approach adopted in the AISC *Seismic Design Manual*. From a design standpoint, the use of this model is likely to reduce conservatisms of the AISC SDM model, while providing adequate safety.

Despite the accuracy of the proposed approach and the improvement (with knowledge advancement) over the current approaches for strength characterization and design of ECB connections, the model has numerous limitations. The model is only validated against 10 tests because these are the only available data on ECB connections. The proposed method considered different failure modes pertaining to the uplift/vertical resistance; however, other limit states associated with vertical bearing are also possible depending on the connection configuration, including (1) concrete breakout under the compression toe of the lower base plate (due to placement of the column on a thin layer of concrete) or (2) yielding of the base plate if not sufficiently thick. These may be resolved by using the internal force transfer mechanisms outlined in this study, albeit with consideration of force capacities associated with these other limit states; additional testing and calibration may be required for this purpose. Additionally, it is noted that the flexural deformations of the column may result in separation between the column flanges and footing (especially if no horizontal reinforcement is provided—as noted by Grilli and Kanvinde, 2017). Under such conditions, the axial compression may not be effectively transferred to the footing through the face-bearing plates on the top of the footing. This may result in punching failure of the supporting slab under the embedded base plate if it is not adequately designed. This failure state was not possible in the test setup of this study. Finally, the approach presented here does not include a reliability study to estimate or recommend ϕ factors. If the approach is used as is, then ϕ implicitly equals 1.0; this is similar to the current approach in the AISC *Seismic Design Manual* (2018).

In conclusion, it is emphasized that the response of these connections is controlled by nonlinear interactions between the various components (steel column/base, concrete, and reinforcement). As a result, it is challenging to develop a design method that explicitly satisfies equilibrium, compatibility, and nonlinear constitutive response of the various components, while also being convenient to apply in a professional setting. Consequently, the method presented in this study is based on some simplifying assumptions. This implies that caution should be exercised in extrapolating the results of this study to details that are highly dissimilar from those examined in this study.

ACKNOWLEDGMENTS

The authors are grateful to the American Institute of Steel Construction and the Charles Pankow Foundation for providing major funding for this project. The authors thank the advisory committee of the project: Mason Walters, Geoff Bomba, and Ali Roufegarinejad of Forell/Elsesser Engineers; Jim Malley of Degenkolb Engineers; Chia-Ming Uang of the University of California at San Diego; Subhash Goel of the University of Michigan; Tom Sabol of Engelkirk Structural Engineers; Tim Fraser of Structural Steel Detailing; Tom Kuznick of Herrick Steel; Joe Zona of Simpson Gumpertz and Heger; Rick Drake of Fluor Corporation; and Devin Huber of AISC.

REFERENCES

ACI (2019), *Building Code Requirements for Structural Concrete and Commentary*, ACI 318-19, Farmington Hills, Mich.

AISC (2016), *Seismic Provisions for Structural Steel Buildings* ANSI/AISC 341-16, American Institute of Steel Construction, Chicago, Ill.

AISC (2018), *Seismic Design Manual*, 3rd Ed., American Institute of Steel Construction, Chicago, Ill.

Anderson, N.S. and Meinheit, D.F. (2005), "Pryout Capacity of Cast-In Headed Stud Anchors," *PCI Journal*, Vol. 50, No. 2, pp. 90–112.

ASCE (1994), "Guidelines for Design of Joints between Steel Beams and Reinforced Concrete Columns," ASCE Task Committee on Design Criteria for Composite Structures in Steel and Concrete, *Journal of Structural Engineering*, ASCE, Vol. 120, No. 8, pp. 2,330–2,357.

Astaneh, A., Bergsma, G., and Shen, J.H. (1992), "Behavior and Design of Base Plates for Gravity, Wind and Seismic Loads," *Proceedings of the National Steel Construction Conference*, AISC, Chicago, Ill.

Cui, Y., Nagae, T., and Nakashima, M. (2009), "Hysteretic Behavior and Strength Capacity of Shallowly Embedded Steel Column Bases," *Journal of Structural Engineering*, ASCE, Vol. 135, No. 10, pp. 1,231–1,238. https://doi.org/10.1061/(ASCE)ST.1943 -541X.0000056

Fahmy, M., Stojadinovic, B., and Goel, S.C. (1999), "Analytical and Experimental Behavior of Steel Column Bases," *Proceedings of the 8th Canadian Conference on Earthquake Engineering*, Canadian Association for Earthquake Engineering, Ottawa.

Falborski, T., Torres-Rodas, P., Zareian, F., and Kanvinde, A. (2020), "Effect of Base-Connection Strength and Ductility on the Seismic Performance of Steel Moment-Resisting Frames," *Journal of Structural Engineering*, ASCE, Vol. 146, No. 5.

FIB (1990), *Model Code*, Comité Euro-International du Beton, Lausanne, Switzerland.

Fisher, J.M. and Kloiber, L.A. (2006), *Base Plate and Anchor Rod Design*, Design Guide 1, 2nd Ed., AISC, Chicago, Ill.

Fuchs, W., Eligehausen, R., and Breen, J.E. (1995), "Concrete Capacity Design (CCD) Approach for Fastening to Concrete," *ACI Structural Journal*, Vol. 92, No. 1, pp. 73–94.

Gomez, I., Deierlein, G., and Kanvinde, A. (2010), "Exposed Column Base Connections Subjected to Axial Compression and Flexure," Final Report, AISC, Chicago, Ill.

Grilli, D., Jones, R., and Kanvinde, A. (2017), "Seismic Performance of Embedded Column Base Connections Subjected to Axial and Lateral Loads," *Journal of Structural Engineering*, ASCE, Vol. 143, No. 5. 04017010. https://doi.org/10.1061/(ASCE)ST.1943-541X.0001741

Grilli, D.A. and Kanvinde, A. (2017), "Embedded Column Base Connections Subjected to Seismic Loads: Strength Model," *Journal of Constructional Steel Research,* Vol. 129, pp. 240–249.

Hanks, K.N. and Richards, A. (2019), "Experimental Performance of Block-Out Connections at the Base of Steel Moment Frames," *Journal of Structural Engineering*, ASCE, Vol. 145, No. 7, 04019057. https://doi.org/10.1061/(ASCE)ST.1943-541X .0002333

Harris, K.A., Mitchell, D., Cook, W.D., and Redwood, R.G. (1993), "Seismic Response of Steel Beams Coupling Reinforced Concrete Walls," *Journal of the Structural Division*, pp. 3,611–3,629. 10.1061/(ASCE)0733-9445(1993)119:12(3611)

Hassan, A.S. (2022), "Seismic Performance of Dissipative, Biaxially Loaded and Embedded Column Base Connections," Doctoral Dissertation, Department of Civil and Environmental Engineering, University of California, Davis.

Hassan, A.S., Song, B., Galasso, C., and Kanvinde, A.M. (2022), "Seismic Performance of Exposed Column Base Plate Connections with Ductile Anchor Rods," *Journal of Structural Engineering*, ASCE. 10.1061/(ASCE)ST.1943-541X.0003298

Hetenyi, M. (1946), "Beams on Elastic Foundation: Theory with Applications in the Fields of Civil and Mechanical Engineering," University of Michigan Press.

Inamasu, H., de Castro e Sousa, A., Güell, G., and Lignos, D.G. (2021), "Anchor-Yield Exposed Column Bases for Minimizing Residual Deformations in Seismic-Resistant Steel Moment Frames," *Earthquake Engineering Structural Dynamics,* Vol. 50, No. 4, pp. 1,083–1,100. https://doi.org/10.1002/eqe.3392

Kanvinde, A.M., Higgins, P., Cooke, R.J., Perez, J., and Higgins, J. (2015), "Column Base Connections for Hollow Steel Sections: Seismic Performance and Strength Models," *Journal of Structural Engineering*, ASCE, Vol. 141, No. 7.

Krawinkler, H., Gupta, A., Medina, R., and Luco, N. (2000), "Loading Histories for Seismic Performance Testing of SMRF Components and Assemblies," Report No. SAC/BD-00/10, SAC Joint Venture, Richmond, Calif.

Marcakis, K. and Mitchell, D. (1980), "Precast Concrete Connections with Embedded Steel Members," *Prestressed Concrete Institute Journal*, Vol. 25, No. 4, pp. 88–116.

Mattock, A.H. and Gaafar, G.H. (1982), "Strength of Embedded Steel Sections as Brackets," *ACI Journal*, Vol. 79, No. 2, pp. 83–93.

Pertold, J., Xiao, R., and Wald, F. (2000a), "Embedded Steel Column Bases—I Experiments and Numerical Simulation," *Journal of Constructional Steel Research*, Vol. 56, No. 3, pp. 253–270.

Pertold, J., Xiao, R., and Wald, F. (2000b), "Embedded Steel Column Bases—II Design Model Proposal," *Journal of Constructional Steel Research*, Vol. 56, No. 3, pp. 271–286.

Richards, P.W., Barnwell, N.V., Tryon, J.E., and Sadler, A. (2018), "Flexural Strength and Stiffness of Block-Out Connections for Steel Columns," *Engineering Structures*, Vol. 173, pp. 404–415. https://doi.org/10.1016/j.engstruct.2018.06.055

SEAOC (2015), *2015 IBC SEAOC Structural/Seismic Design Manual Volume 1: Code Application Examples*, Sacramento, Calif.

Shahrooz, B.M., Remetter, M.E., and Qin, F. (1993), "Seismic Design and Performance of Composite Coupled Walls," *Journal of Structural Engineering,* ASCE, Vol. 119, No. 11, pp. 3,291–3,309.

Trautner, C.A., Hutchinson, T., Grosser, P.R., and Silva, J.F. (2017), "Investigation of Steel Column-Baseplate Connection Details Incorporating Ductile Anchors," *Journal of Structural Engineering*, ASCE, Vol. 143, No. 8, 04017074. https://doi.org/10.1061/(ASCE)ST.1943-541X.0001759

Vecchio, F.J. and Collins, M.P. (1986), "The Modified Compression-Field Theory for Reinforced Concrete Elements Subjected to Shear," *ACI Journal*, Vol. 83, No. 2, pp. 219–231.

Wald, F. (2000), "Column Base Modelling," in M. Ivanyi and C.C. Baniotopoulos, eds., *Semi-Rigid Joints in Structural Steelwork*, International Centre for Mechanical Sciences, Vol. 419, Springer, Vienna, pp. 227–288.

Steel Structures Research Update

Adhesive Steel-to-Steel Connections

JUDY LIU

INTRODUCTION

Ongoing research on adhesive steel-to-steel connections is highlighted. This study, currently under way at the University of Massachusetts–Amherst, is led by Dr. Kara Peterman, Associate Professor in the Department of Civil and Environmental Engineering. Dr. Peterman's research interests include behavior of cold-formed and hot-rolled steel structures under service loads and extreme loads due to natural hazards. Among Dr. Peterman's accolades for her teaching and research are the University of Massachusetts–Amherst College of Engineering Outstanding Teacher Award, the McGuire Award for Junior Researchers from the Structural Stability Research Council (SSRC), the AISC Terry Peshia Early Career Faculty Award, and the AISC Milek Fellowship. The four-year Milek Fellowship is supporting this research on the holistic design and behavior of adhesive steel-to-steel connections. The research team is partway through year two of the four-year study. Selected highlights from the work to date are presented, along with a preview of future research tasks.

BACKGROUND AND MOTIVATION

The research team seeks to fill knowledge gaps and realize the great potential for adhesive structural steel connections. Experience with adhesives exists primarily in aerospace, nautical, and automotive industries, with some in cross-laminated timber and concrete construction, and more limited work with structural steel. Potential benefits for adhered steel-to-steel connections include improved performance of mechanical connections, connection flexibility, and reduction or elimination of stress concentrations.

A literature review highlights potential applications, anticipated benefits, and knowledge gaps. Applications related to the proposed research have included bridge retrofit, light-framed construction, and steel connections. Bridge retrofit work includes a Hu et al. (2006) study on adhered steel angles to mitigate out-of-plane, distortion-induced fatigue cracks. Two successful field tests on skewed bridges and large-scale laboratory tests demonstrated environmental durability and reductions in strains, with some loosening of the adhesives after millions of cycles of loading (Hu et al., 2006). In their investigation of bridge retrofit schemes using fiber-reinforced polymer (FRP) plates adhered to steel, André et al. (2012) observed debonding of the adhesive from the steel and failure within the adhesive itself. Peterman et al. (2017) also observed failures between adhesives and polymers in research on thermal break strategies for steel building systems. Serrette et al. (2006) explored cold-formed steel shear walls bonded to steel sheets or oriented strand board. The shear walls were attached to the stud wall framing with adhesive and fasteners. Peak wall resistance and stiffness were increased, but energy dissipation decreased. The researchers pointed to the need for additional research on the adhesive and connection detailing (Serrette et al., 2006). Steel double-lap splice connections studied by Sadowski et al. (2010) utilized a rivet, adhesive, or a combination. The combined connection demonstrated increased connection strength, elastic stiffness, and ductility. Gasparini et al. (1990) investigated mechanical properties of adhered steel-to-steel connections, identifying research needs in behavior under sustained loading and tensile creep rupture. Ikegami et al. (1996) demonstrated variability in the behavior of adhesively bonded steel connections (e.g., lap splices, butt joints), noting dependence on the curing process. Meanwhile, de Morais et al. (2007) demonstrated improved connection strength with increased adhesive thickness in lap splice and butt joint connections.

The literature review identifies lack of standards for adhesives in steel construction as well as research needs. More data are needed on adhered steel-to-steel connections, their limit states, and behavior (e.g., creep). Research must address adhesives used in combinations of connecting elements or as grout, fill encasement, or thermal break. Development of systematic methods for performance evaluation will further advance adhered structural steel connections. Challenges include the need for a controlled environment, different adhesives for different applications, lack of specifications, and varied mechanical performance based on curing.

PROPOSED RESEARCH AND DELIVERABLES

The research team is providing fundamental knowledge needed to advance adhesives for slip-critical bolted

Judy Liu, PhD, Research Editor of the AISC *Engineering Journal*, Professor, Oregon State University, School of Civil and Construction Engineering, Corvallis, Ore. Email: judy.liu@oregonstate.edu

connections, prefabricated modular construction, bridge girder splices, and anchorage. Questions about installation procedure, structural behavior, creep performance, and performance under elevated temperatures are being addressed. The proposed work synthesizes existing knowledge, leverages the expertise of an industry advisory panel, identifies viable adhesives and applications, conducts experimental testing to address knowledge gaps in mechanical properties and structural behavior, and develops design recommendations (Figure 1).

Numerous opportunities exist for adhesives in structural steel construction. Adhesives may be integrated into bolted and welded connections and do not introduce stress concentrations or require any changes in the bolt or weld configurations. Adhesives may allow greater control of connection failure mode and energy dissipation. Adhesives may also be used to fill connection gaps or as anchor rod grout or connection encasement.

Research to address knowledge gaps and pursue opportunities leads to five major deliverables. The first deliverable is the information about the structural behavior of adhered steel-to-steel connections. The second is the validation of adhesives for these connections. Validation is tied to the determination of performance objectives and minimum properties for the adhesives. The third deliverable is a set of recommendations providing guidance on selection, design, and detailing of connections with structural adhesives. Accompanying the design recommendations is the fourth deliverable, a centralized and searchable database of available structural adhesives. Finally, underlying the research outcomes is the fifth deliverable, the experimental data.

The experimental work plan is a systematic investigation at material, connection, and subsystem levels (Figure 2). Material-level testing addresses tension, compression, and creep. Double-lap splices and anchors will be explored in connection-level testing. At the subsystem level, steel deck diaphragms and steel-sheet sheathed cold-formed steel (CFS) shear walls will be tested.

Material-Level Testing

Material-level testing focuses on strength characterization of the adhesives. The impact of curing methods and surface preparation on the mechanical properties will also be assessed. The research team plans to utilize available standards for adhesives and adapt standards as needed for tension, compression, and creep (Figure 2). Elastic yield strength and ultimate strength will be evaluated following ASTM D638, the test standard used for plastics (ASTM, 2022). Tension coupons will be machined from properly cured adhesive stock. The team will assess impact of cure time, cure temperature, and surface preparation on adhesives under tensile loading. Procedures such as ASTM D1002 (ASTM, 2019) for "Apparent Shear Strength of Single-Lap Joint Adhesively Bonded Metal Specimens by Tension Loading (Metal-to-Metal)" will be followed. Relevant standards [ASTM D2293 (ASTM, 2002), ASTM D2294 (ASTM, 2016)] will be utilized for creep testing of lap joints (adhesives in shear) under tension and compression loading. The team expects to investigate three adhesives and two curing methods. The results for the material-level testing will lay the foundation for test phases to follow.

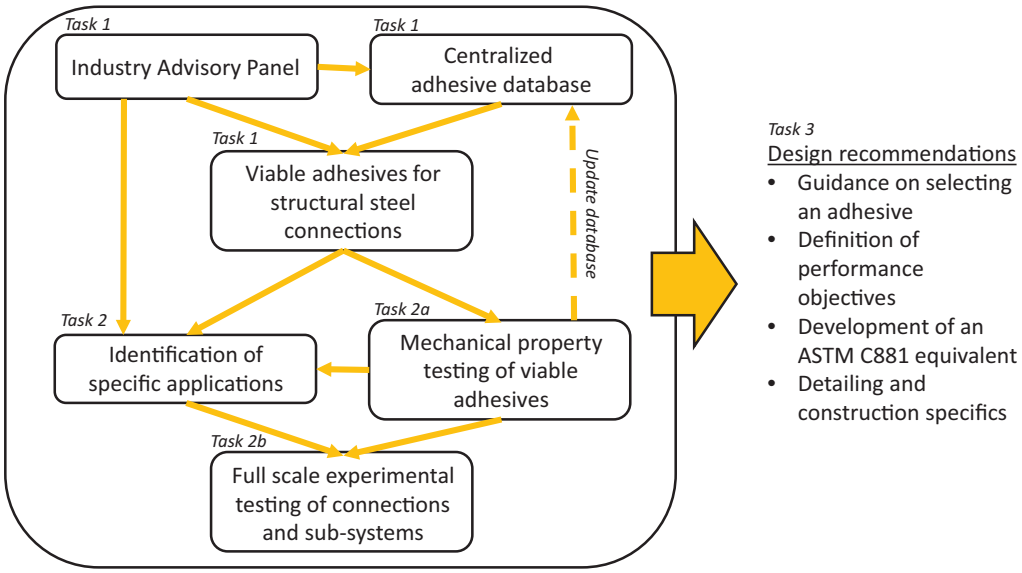

Fig. 1. Research tasks and deliverables.

Connection Testing

Connection tests will further inform design guidance for applications such as adhered anchor rods, steel deck diaphragms adhered to steel joists, and steel-sheet sheathed cold-formed steel (CFS) shear walls. Double-lap splice connections will be used to capture adhesive-steel interactions at a component level (Figure 3). Based on the literature and identified research needs, parameters will include thickness of the adhesive, combinations of adhesives with slip-critical bolts, and elevated temperatures. For the anchor rods, isolated adhered anchor rod pull-out tests will be conducted (Figure 4). Adhesive thickness may again be a parameter. Where thickness is dictated by the available fill space, the test results will provide upper and lower bounds on performance. These tests will use the same curing methods and adhesives as in the material-level tests. All specimens will be loaded with monotonic displacement control.

Subsystem Testing

The subsystem testing will focus on steel deck diaphragms adhered to steel joists and steel-sheet sheathed cold-formed steel (CFS) shear walls. The research team has chosen these subsystems to highlight the potential benefits of adhesives for prefabricated panels or modules for construction. Replacing or reducing the number of fasteners with adhesives may improve fabrication and installation time. Adhesives and methods will be chosen based on the materials and connection level testing. These experiments will leverage the existing cantilever diaphragm rig at UMass Amherst (Figure 5). Steel deck diaphragms will be adhered to steel joists as shown schematically in Figure 6. In its current configuration, the rig is set for 15 ft by 15 ft specimens but can be modified to accommodate 10 ft by 10 ft specimens. Expected research deliverables include information about the feasibility of adhered connections for CFS shear walls and deck diaphragms, as well as the behavior of these subsystems.

LITERATURE REVIEW, DATABASE, AND TEST PLANNING

Work to date has included a literature review, database, test planning, and creep testing that is under way. The literature review has confirmed that there is ample information on aerospace, automotive, and naval uses, but not much related to building applications. Large-scale tests (e.g., Serette et al., 2006; Hu et al. 2006) are also rare. The review has provided structural adhesives to populate the database, information on testing procedures, pointers to gaps in knowledge, and the groundwork for test planning.

For test planning, the literature has informed test procedures and properties of ideal adhesives. Ideal adhesives should include a high lap shear strength, long pot life or handling time to facilitate fabrication of joints, and low elongation at high loads. Ideally, the adhesives should also have a high glass transition temperature and a practical in-service temperature range. The curing method should be appropriate for large-scale work, whether in the fabrication shop or in the field. Meanwhile, relevant test standards have been reviewed and work on prototypes completed.

The database utilizes an online web application designed for sharing computational documents. The Jupyter Notebook features plots such as distributions of lap shear strengths and handling times for the adhesives in the database. The "live" Notebook updates plots with any changes in the database.

Challenges experienced by the research team include variability in manufacturer information and curing methods. Not all manufacturers release the same information in their data sheets; the research team is missing information for some adhesives. This introduces difficulties in

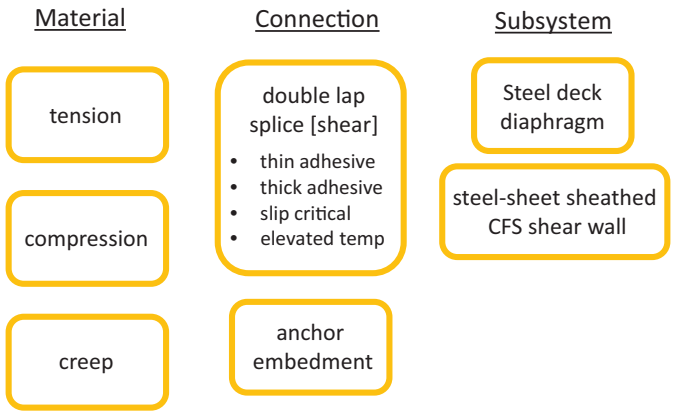

Fig. 2. Material, connection, and subsystem levels of investigation.

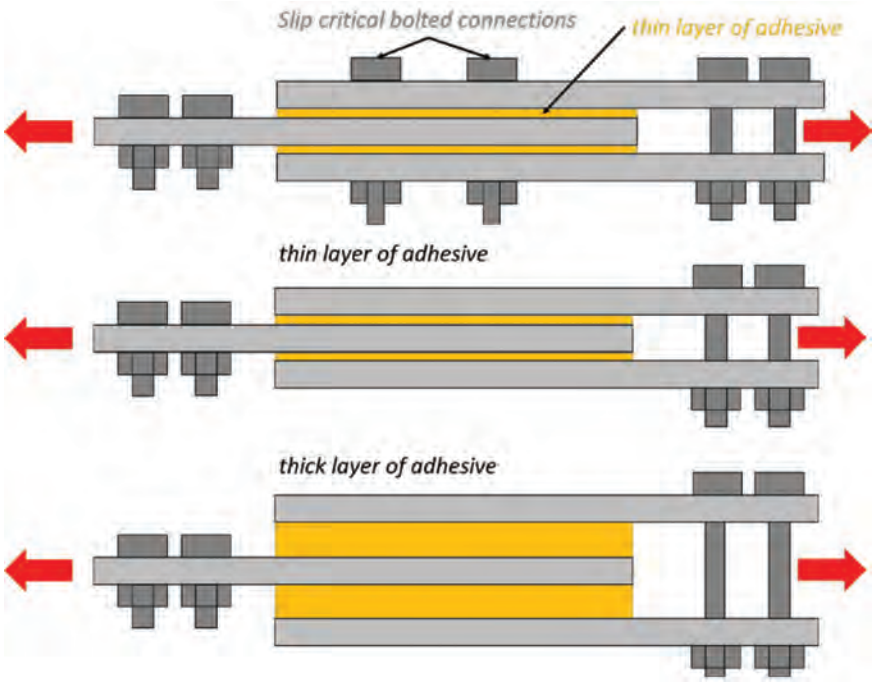

Fig. 3. Double-lap splice connection test configurations.

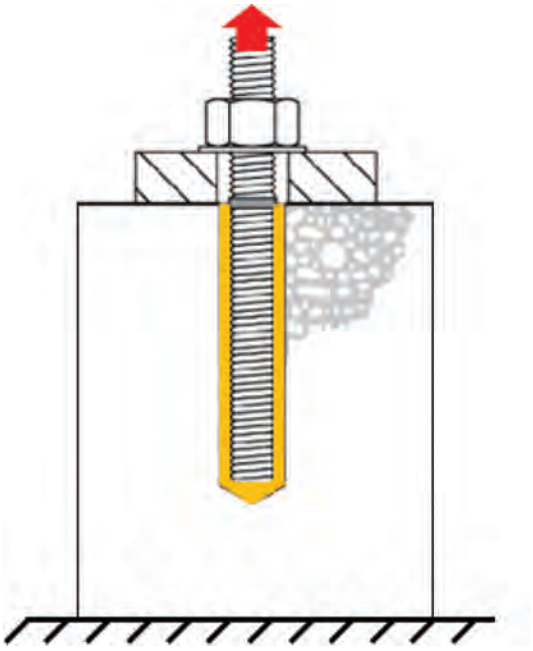

Fig. 4. Anchor rod pull-out test configuration.

Fig. 5. Cantilever diaphragm testing rig at UMass Amherst.

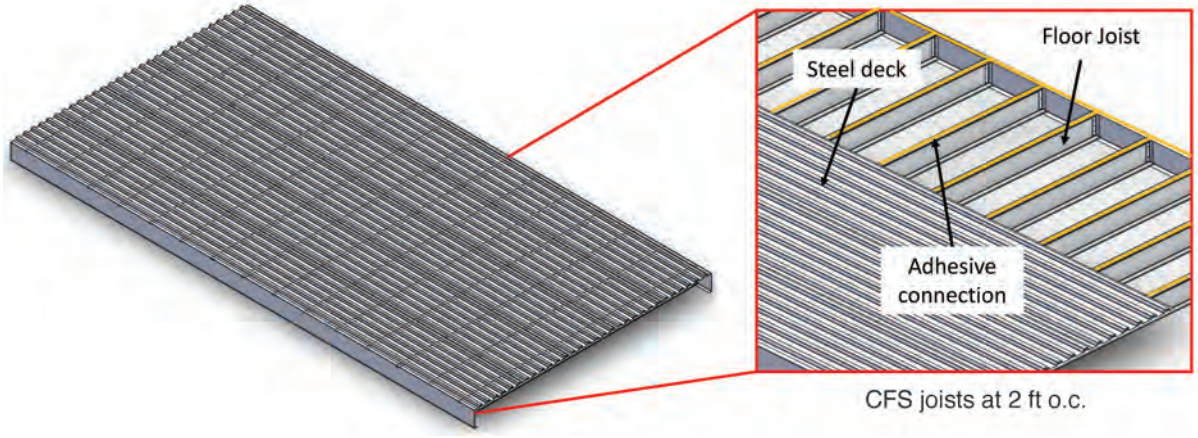

Fig. 6. Steel deck diaphragm-joist subassembly.

comparing adhesives. Different curing methods maximize different properties such as cure time, glass transition temperature, strength, or in-service temperature range. Synthesis of available products and methods continues.

COMPLEMENTARY RESEARCH EFFORTS

This research has also been informed by complementary work by the Virginia Department of Transportation (DOT) and the Federal Highway Administration (FHWA). Jason Provines, Virginia Transportation Research Council (VTRC), leads the DOT work focused on adhesives for gap filling and joint sealing at bridge girder ends. The adhesive joints are primarily under compressive loading. Ryan Slein and Fang Wang are in Phase 2 of their research, having completed a Phase 1 experimental study comparing performance of adhesive-enhanced bolted connections with conventional double-lapped shear bolted connections. Creep of adhesives and relaxation of bolt pretension were also investigated.

These groups shared research at a workshop hosted by UMass Amherst. Workshop outcomes included comparisons of adhesive selection processes and experimental protocols. The workshop highlighted the challenges in specifying adhesives for universal structural steel application. While the UMass and FHWA research teams had overlapping research goals (primarily shear connections), and thus overlapping adhesive selection, the VTRC team focused on entirely on compression joints and examined a different suite of structural adhesives. In translating research outcomes to practice, and to meet this challenge, the UMass team will be working to establish acceptable performance criteria to be used under certain load conditions.

FUTURE WORK

Work continues on the testing, database building, and design recommendation development. Looking ahead to one of the major deliverables, the research team expects to develop equations and recommendations that parallel existing guidance. For example, ASTM C881 (ASTM, 2020), "Standard Specification for Epoxy-Resin-Base Bonding Systems for Concrete," provides performance objectives for adhesives for specific applications. Applications range from load-bearing applications to non-load-bearing sealants. Each application type is defined along with performance targets to be achieved in order for an adhesive to be rated for that application. The adhesive rating system will be informed by the experimental testing and guidance from the industry advisory panel.

ACKNOWLEDGMENTS

Thank you to Dr. Kara Peterman for her contributions to this article. The work of PhD student Kate Sullivan is also recognized. The research is sponsored by the American Institute of Steel Construction (AISC) through the Milek Fellowship, with technical and financial support from the American Iron and Steel Institute (AISI) and the Steel Deck Institute (SDI). The researchers would also like to thank Advisory Committee members Caroline Bennett (University of Kansas), Devin Huber (AISC), Chris Garrell (AISC/NSBA), John Hooper (MKA), Ronnie Medlock (High Steel Structures), Bonnie Manley (AISC), Ryan Slein (FHWA), Tom Sputo (SDI), Brian Volpe (Cives Steel), Duff Zimmerman (Cooper Steel), Joe Zona (SGH), and Aamer Syed (Sika). Any findings or recommendations are those of the researchers and do not necessarily reflect the views of the sponsors.

REFERENCES

André, A., Haghani, R., and Biel, A. (2012), "Application of Fracture Mechanics to Predict the Failure Load of Adhesive Joints Used to Bond CFRP Laminates to Steel Members," *Construction and Building Materials*, Vol. 27, No. 1, pp. 331–340. https://doi.org/10.1016/j.conbuildmat.2011.07.040.

ASTM (2002), *Standard Test Method for Creep Properties of Adhesives in Shear by Compression Loading (Metal-to-Metal)*, ASTM D2293-96, ASTM International, West Conshocken, Pa. https://doi.org/10.1520/D2293-96R02

ASTM (2016), *Standard Test Method for Creep Properties of Adhesives in Shear by Tension Loading (Metal-to-Metal)*, ASTM D2294-96, ASTM International, West Conshocken, Pa. https://doi.org/10.1520/D2294-96R16

ASTM (2019), *Standard Test Method for Apparent Shear Strength of Single-Lap-Joint Adhesively Bonded Metal Specimens by Tension Loading (Metal-to-Metal)*, ASTM D1002-10, ASTM International, West Conshocken, Pa. https://doi.org/10.1520/D1002-10R19

ASTM (2020), *Standard Specification for Epoxy-Resin-Base Bonding Systems for Concrete*, ASTM C881/C881M-20a, ASTM International, West Conshocken, Pa. https://doi.org/10.1520/C0881_C0881M-20A

ASTM (2022), *Standard Test Method for Tensile Properties of Plastics*, ASTM D638-22, ASTM International, West Conshocken, Pa. https://doi.org/10.1520/D0638-22

de Morais, A.B., Pereira, A.B., Teixeira, J.P., and Cavaleiro, N.C. (2007), "Strength of Epoxy Adhesive-Bonded Stainless-Steel Joints," *International Journal of Adhesion and Adhesives*. https://doi.org/10.1016/j.ijadhadh.2007.02.002.

Gasparini, D.A., Nara, H., Andreani, J., Boggs, C., Brewer, D., and Etitum, P. (1990), "Steel-to-Steel Connections with Adhesives," *Journal of Structural Engineering,* ASCE, Vol. 116, No. 5. https://doi.org/10.1061/(ASCE)0733-9445(1990)116:5(1165)

Hu, Y., Shield, C., and Dexter, R. (2006), "Use of Adhesives to Retrofit Out-of-Plane Distortion Induced Fatigue Cracks," Report No. MnDOT 2006-04, Minneapolis, Minn.

Ikegami, K., Fujii, T., Kawagoe, H., Kyogoku, H., Motoie, H., Nohno, K., Sugibayashi, T., and Yoshida, F. (1996), "Benchmark Tests on Adhesive Strengths in Butt, Single and Double Lap Joints and Double-Cantilever Beams," *International Journal of Adhesion and Adhesives*. https://doi.org/10.1016/0143-7496(95)00051-8.

Peterman, K.D., Kordas, J., Moradei, J., Coleman, K., Der Ananian, J., Webster, M.D., D'Aloisio, J.A., and Hajjar, J.F. (2017), "Thermal Break Strategies for Cladding Systems in Building Structures," Report to the Charles Pankow Foundation, Charles Pankow Foundation, Vancouver, Wash.

Sadowski, T., Kneć, M., and Golewski, P. (2010), "Experimental Investigations and Numerical Modelling of Steel Adhesive Joints Reinforced by Rivets," *International Journal of Adhesion and Adhesives*. https://doi.org/10.1016/j.ijadhadh.2009.11.004.

Serrette, R., Lam, I., Qi, H., Hernandez, H., and Toback, A. (2006), "Cold-Formed Steel Frame Shear Walls Utilizing Structural Adhesives," *Journal of Structural Engineering,* ASCE, Vol. 132, No. 4. https://doi.org/10.1061/(ASCE)0733-9445(2006)132:4(591)

ERRATA

Application of AISC *Specification* Requirements for Second-Order Analysis and Stability Design

Rafael Sabelli, Allen Adams, and David Landis

Vol. 60, No. 3, 2023

Revise the bottom two rows in Table 1:

Table 1. Methods of Addressing Stability-Design Considerations

Stability-Design Consideration		Direct Analysis Method	Effective Length Method	First-Order Method
(a) All deformations that contribute to the displacements of the structure		Analysis of model that includes all significant sources of flexibility		
(b) Second-order effects	System P-Δ effects (including P-δ effect on P-Δ)	Second-order analysis		Additional lateral load
	Member P-δ effects	B_1 amplifier or inclusion of member P-δ effect in second-order analysis		B_1 amplifier
(c) Geometric imperfections (system)	Effect on structural response	Minimum notional load or modeling of imperfections	Minimum notional load	
(c) Geometric imperfections (member), (d) Stiffness reduction due to inelasticity, and (e) Uncertainty in strength and stiffness	Effect on structural response	Stiffness reduction	Effective length factor	Additional lateral load
	Effect on member strength	Member strength formulae		

Guide for Authors

Scope

Engineering Journal is dedicated to the improvement and advancement of steel construction. Its pages are open to all who wish to report on new developments or techniques in steel design, research, the design and/or construction of new projects, steel fabrication methods, or new products of significance to the uses of steel in construction. Only original papers should be submitted.

General

Papers intended for publication should be submitted by email Margaret Matthew, editor, at **matthew@aisc.org**.

The articles published in the *Engineering Journal* undergo peer review before publication for (1) originality of contribution; (2) technical value to the steel construction community; (3) proper credit to others working in the same area; (4) prior publication of the material; and (5) justification of the conclusion based on the report.

All papers within the scope outlined above will be reviewed by engineers selected from among AISC, industry, design firms, and universities. The standard review process includes outside review by an average of three reviewers, who are experts in their respective technical area, and volunteers in the program. Papers not accepted will not be returned to the author. Published papers become the property of the American Institute of Steel Construction and are protected by appropriate copyrights. No proofs will be sent to authors.

Manuscripts

Manuscripts must be provided in Microsoft Word format. Include a PDF with your submittal so we may verify fonts, equations and figures. View our complete author guidelines at **aisc.org/ej**.

Smarter. Stronger. Steel.

American Institute of Steel Construction
130 E Randolph St, Ste 2000, Chicago, IL 60601
312.670.2400 | aisc.org/ej